Investigation of Spatial Harmonic Magnetrons for High Power Millimetre and THz Wave Operations

A thesis submitted to the University of London for partial fulfilment of the requirements for the degree of Doctor of Philosophy

By

Jiandong Lang

Supervisor: Prof. Xiaodong Chen

School of Electronic Engineering and Computer Science
Queen Mary University of London

November 2016

Abstract

Magnetron is a crossed-field vacuum tube and has found applications in many fields where high power microwave is required, such as meteorological radar, marine navigation, particle accelerator and domestic and industrial heating. When the operating frequencies are in millimetre-wave/THz band, conventional magnetrons show an inherent limitation due to complex small structure, short life time and intense magnetic field.

Recently, the Spatial Harmonic Magnetron (SHM) has been proved to be an effective alternative to conventional magnetron for millimetre-wave/THz applications with the advantages of simple anode structure, sufficient life time, low voltage and magnetic field. However, the physics of the operation of SHM have not been adequately understood. In this thesis, considerable insight into the SHM operation has been obtained based on the 3-D particle simulation and experiment.

The investigation of a 16-vane SHM operating in the $\pi/2$-1 mode at 35GHz reveals that the cathode current mainly depends on the electron secondary emission from the cold cathode rather than the injection current from the side cathode. The smaller secondary emission coefficient causes noisy output spectrum and low output power. When the secondary emission coefficient reduces below a threshold value, the oscillation cannot start. The transient behaviour shows that the neighbouring modes compete with the working mode. The particle-in-cell (PIC) simulation of a $\pi/2$ SHM demonstrates that the oscillation could jump from the working mode to its neighbouring mode with a slight change of the anode voltage.

The simulated performance on a compact 95 GHz SHM is in a good agreement with the measured one. A number of engineering issues, such as the pulse duration, the anode temperature and vacuum break down have been considered for the SHM to deliver more than 5kW peak power with 200ns pulse in 0.05% duty cycle. The quality of output signal pulses assessed in the experiment indicates that this SHM can be effectively used for the development of low cost W-band cloud radar.

There are a number of technical challenges in designing and fabricating THz-band SHMs with good performance, such as fabrication of a large number of cavities and the cold cathode. The modelling of a 40-vane 209 GHz SHM operating on the π/2-1 mode and the measurement on fabricated anode cavity indicates that the fabrication tolerance should be taken into account in the design of a high frequency SHM.

Based on the analysis on a 44-cavity anode, the π/2-3 mode is chosen to improve the mode stability. The PIC simulation indicates that such magnetrons can deliver at least 0.6 kW peak power at a frequency above 300GHz.

Acknowledgements

First and foremost I would like to express my deep and sincere gratitude to my supervisor Prof. Xiaodong Chen for his supervision throughout my PhD study. His precious personalities and serious research attitude not only influenced my time of study, but will continue to do so throughout my life.

I am also greatly indebted to Prof. Clive Parini and Dr. Robert. S. Donnan for serving in my committee during mid-exams. Special thanks to Prof. Dmytro M. Vavrive in the Institute of Radio Astronomy of Ukraine for this support on the magnetron experiment. I would also like to thank Dr. Yasir Alfadhl who guided me almost one year.

Many thanks are also due to the following people who have kindly offered their help:

- Dr. Monika Balk in CST for her help on particle simulation techniques.
- Dr. Nasrin Nasresfahani in Hamburg University of Technology for her suggestions about magnetron modelling.
- Mr. Thomas M. Loftus for his assistance of the experiment.
- Mrs. Mellisa Yeo, Mrs, Jennifer Murray, Dr. Ke yang, Dr. Max. M. Torrico, Dr. Xiang Li, Dr. Daohui Li and all my colleagues in Queen Mary University of London for the their help of my PhD study.

Lastly, I would like to convey my gratitude to my parents who raised me and supported me in all my pursuits. It is maybe the best place to say thanks to my lovely and considerate wife Mrs. Ding whose support and encouragement are so appreciated.

Table of Contents

List of Figures

List of Tables

Abbreviations and Glossary

VED	Vacuum Electronic Device
BWO	Backward Wave Oscillator
TWT	Travelling Wave Tube
FEL	Free Electron Laser
CFA	Crossed Field Amplifier
THz	Terahertz
EIK	Extended Interaction Klystron
SHM	Spatial Harmonic Magnetron
FIT	Finite Integration Technique
PIC	Particle in Cell
PMC	Perfect Magnetic Conductor
AKS	Advanced Krylov Subspace
JDM	Jacobi-Davidson Method
VNA	Vector Network Analyser
TSS	Tangential Signal Sensitivity
WEDM	Wire Electric Discharge Machining

List of Publications

Journal papers

[1] X. Li, **J. Lang**, Y. Alfadhl, X. Chen, "Study of an Eighth-Harmonic Large-Orbit Gyrotron in the Terahertz Band", IEEE Transactions on Plasma Science, vol. 43, pp.506-514.

[2] **J. Lang**, Y. Alfadhl, and X. Chen,” Design and Simulation of a 300GHz Spatial Harmonic Magnetron,” in preparation.

Conference papers

[1] **J. Lang**, Y. Alfadhl, and X. Chen, “Investigation of a W-band spatial harmonic magnetron for the application of cloud radar,” 9th Europe/UK-China Conference on Millimetre waves and THz Technologies (UCMMT), Qingdao, China, 2016.

[2] **J. Lang**, X. Li, Y. Alfadhl, and X. Chen, "Study of a THz spatial harmonic magnetron," 16th IEEE International Vacuum Electronic Conference (IVEC), Beijing, China, 2015.

[3] X. Li, **J. Lang**, Y. Alfadhl, and X.Chen., “Numerical study of a high-harmonic gyrotron using an axis-encircling electron beam” 16th IEEE International Vacuum Electronic Conference (IVEC), Beijing, China, 2015.

[4] **J. Lang**, X. Chen, and R. Donnan. “Simulation of a 209 GHz Magnetron by using CST Particle Studio,” Workshop on terahertz, Saint Petersburg, Russia, 2015.

[5] **J. Lang**, X. Li, Y. Alfadhl, and X. Chen, “Investigation of a 0.2-THz magnetron using 3D particle simulation” 7th Europe/UK-China Conference on Millimetre waves and THz Technologies (UCMMT), Chengdu, China, 2014. (*Best student paper*)

[6] X. Li, **J. Lang**, Y. Alfadhl, and X. Chen “Study of a 0.42 THz fourth-harmonic large orbit gyrotron,”39th International Conference on Infrared, Millimeter, and Terahertz Waves, IRMMW-THz, September, 2014.

[7] X. Li, **J. Lang**, Y. Alfadhl and X. Chen, "3D PIC simulation of starting process of oscillation in a 42 GHz gyrotron", UCMMT2013: 6th UK, Europe, China Millimeter Waves and THz Technology Workshop National Roman Museum, Rome, Italy 9-11 September 2013.

[8] **J. Lang**, X. Li, Y. Alfadhl and Xiaodong Chen, "3D spatial harmonic magnetron - a contender for compact high power THz source", National Vacuum Electronics Conference (NVEC), London, UK, 2013.

Chapter 1 Introduction

1.1 Introduction to Vacuum Electronic Devices

Magnetron is the first practical vacuum electronic device (VED) which was developed in England in the 1930's and it provided the impetus for the development of microwave radar during World War II [1-3]. Since then, a large variety of VEDs have been developed for the generation and amplification of microwave power, such as backward-wave oscillators (BWOs) [4], travelling wave tubes (TWTs) [5, 6], klystrons [7, 8], free electron lasers (FELs) [9, 10], and gyro-devices [11, 12]. Although solid-state devices have been progressively filling roles that once could only be met by VEDs, VEDs are still essential for the generation of very high powers (10 kW and higher) at millimetre-wave and THz frequencies (100 GHz and higher) [13, 14].

1.1.1 Fundamental of Vacuum Electronic Devices

There are various types of VEDs, but they all share some common features and fundamental operating mechanisms. A typical VED consists of two or more electrodes enclosed in a metal vacuum envelop. The electrons are emitted from the cathode by thermionic emission, or electric field emission, or some other methods, such as secondary emission. Thermionic cathodes fabricated by a barium oxide–coated metal surface, or an impregnated tungsten surface are commonly used.

Fundamentals of all VEDs are the dynamics of electrons under different electric- and magnetic-field configurations. The principle of operation is to transfer the kinetic energy of electrons to the RF field so as to enhance electromagnetic radiation. For example, when an electron is decelerated, its kinetic energy is transferred to the RF field. Thus, the DC energy stored in an external power supply can be converted to RF energy. The RF energy is coupled out of envelop to the load circuit accomplished with coupling slots or probes, or transparent windows. After the electrons leave the electron-wave interaction space, remaining electrons are collected by the collector elements. Because of the requirement for a high vacuum and the need to dissipate large amounts of heat, VEDs are generally large and bulky compared with solid-state devices. In addition, VEDs often require magnetic field and high voltage power supplies. Factors to consider in the choice of a particular type of VEDs include output power, frequency, bandwidth, tuning range, and noise.

1.1.2 Different types of vacuum electronic devices

Depending on the different interaction mechanism between the electrons and the electromagnetic field, VEDs are often grouped into two categories: the ‘O’ type and the ‘M’ type [15]. The ‘O’ type is also called a linear-beam type, in which the electron beam traverses the length of the tube parallel to the magnetic field and the magnetic field is used for focusing only, such as TWTs and Klystrons. The TWT is usually used as an amplifier. Figure 1.1 is an example of a TWT in which the slow wave structure is a helix.

It uses an electron gun and a focusing magnet to generate and accelerate an electron beam through an interaction region. The RF input is coupled to the slow wave structure at the electron gun end. The helical structure slows down the propagating RF wave so that it travels with the velocity close to the electron beam along the interaction region, which makes the beam-wave interaction possible. Then the amplified signal is coupled out at the end of the helix. The TWT has the highest bandwidth of any amplifier tube, ranging from 30% to 120%. This makes it very useful for electronic warfare systems and satellite communications which require high power over broad bandwidths [16].

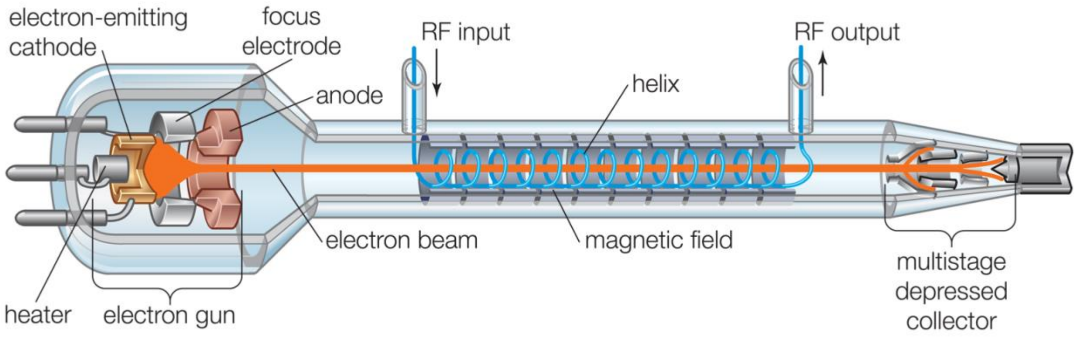

Figure 1.1 Schematic of a travelling wave tube [17].

The ‘M’ type is also called crossed-field devices, in which magnetic field is perpendicular to both the electron beam and the accelerating electric field and plays a direct role in the interaction process. Typical ‘M’ type devices are magnetrons and crossed-field amplifiers (CFAs). Figure1.2 shows a structure of a conventional cavity magnetron. It consists of a cylindrical cathode and a coaxial anode with several individual resonant cavities. The most efficient oscillation mode is the π mode, when the adjacent cavities are 180^o out of phase. A static magnetic field is parallel to the axis of the cathode. During the start-up of oscillation, the electron cloud rotates around the cathode surface and generates noise. When the RF field grows and the anode voltage exceeds a certain value, electrons begin to transfer their energy to the RF field. When the anode voltage and the static magnetic field are properly selected, the π mode oscillations will dominate. A detailed mechanism of operation and typical characteristics of magnetron will be discussed in Chapter 2. The magnetron has the advantages of being able to generate high power (from several kilowatts to megawatts) at high efficiency (80% -90%). Magnetrons are widely used in radar systems [18, 19], medical X-ray source [20], microwave oven and heating [21]. With the advantages of low cost and compact structure, magnetron is also selected as a power source in microwave wireless power transmission systems [22].

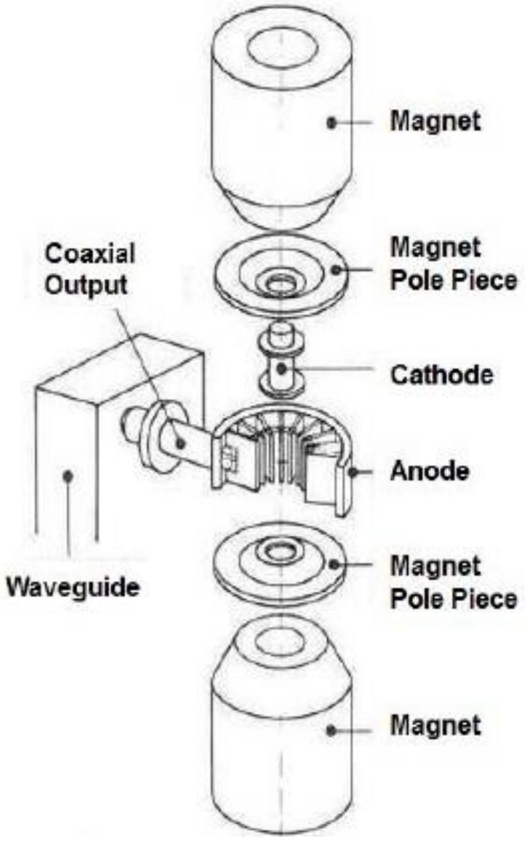

Figure 1.2 Basic structure of a conventional magnetron [19].

The VEDs also can be classified as slow-wave devices and fast wave devices. The devices introduced above are slow-wave devices in which the interaction circuits are designed to reduce the phase velocity of the electromagnetic wave below the speed of light. In fast-wave devices, the RF structure is usually a smooth waveguide or a large resonator in which no attempt is made to reduce the velocity of the wave. The result is that the size limitations found in slow-wave devices are significantly relaxed. With larger dimensions, the power-handling capability is also enhanced.

Gyrotron is a typical fast wave device which can be used as an amplifier or oscillator. As shown in Figure 1.3, it consists of an electron gun with input and output cavities along the axis of the electron beam. It usually has a solenoidal bias magnet that provides an axial magnetic field. This field forces the electrons to travel in tight spirals down the length of the tube.

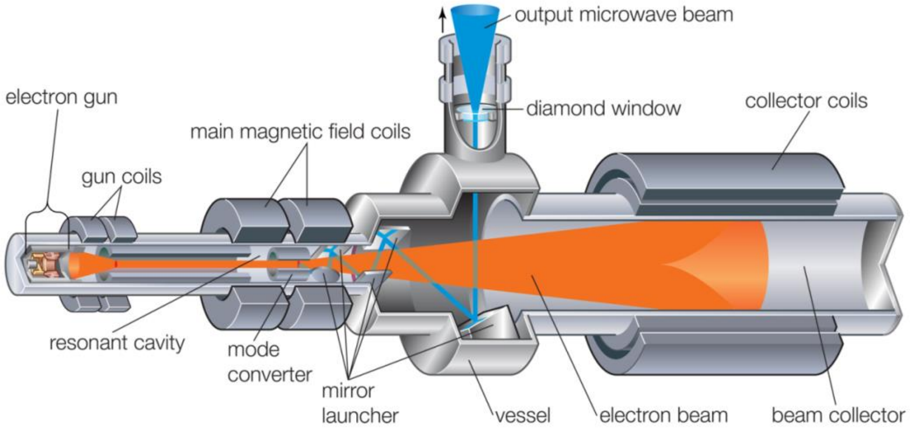

Figure 1.3 Schematic of a gyrotron [17].

The electron velocity is so high and the relativistic effect will cause the spiralling electrons to bunch in the transverse plane. And then, a net energy from the transverse component of the electron velocity is transferred to the RF field if a proper synchronisation condition is satisfied. A significant feature of the gyrotron is that the frequency of operation is determined by the bias field strength and the electron velocity, as opposed to the dimensions of the tube itself. This makes gyrotron especially useful for frequencies above 100 GHz, as shown in Figure 1.4. However, the development of the fast-wave devices is limited by the complex structure and the requirement of intense external magnetic field.

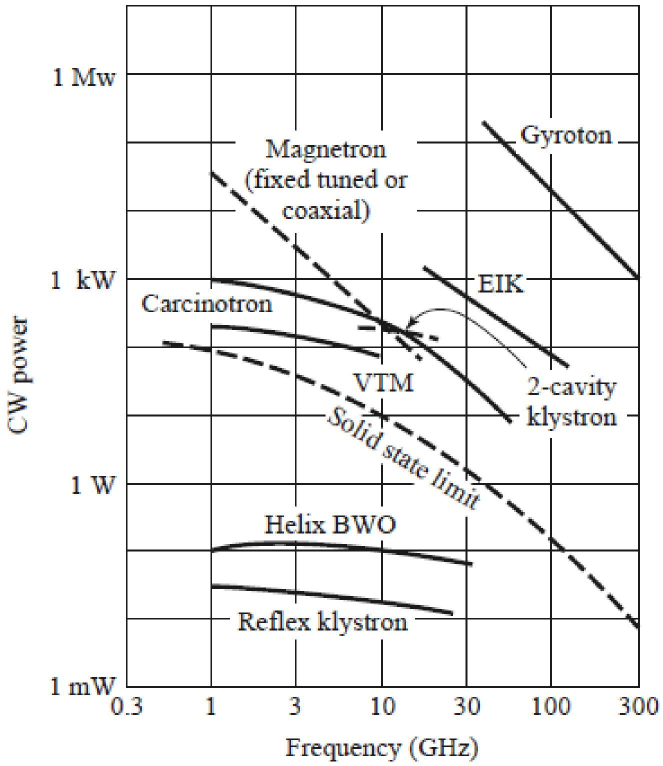

Figure 1.4 Power versus frequency performance of VEDs [16].

1.2 Applications of Millimetre-wave and THz Magnetron

1.2.1 Millimetre-wave cloud radar

The cloud is an important component of the climate system, which has a profound impact on the Earth's climate. It is a fundamental stage of water cycle in the atmosphere, condensing water vapour and forming precipitation. The cloud has macro physical properties and micro properties. Macro physical properties are the height of the cloud base and top, and related to that the thickness (vertical extent) of the cloud, the cloud fraction and the cloud overlap. Microphysical cloud properties are the phase of the particles (water or ice) and the particle size distribution.

The diameters of the particle in the cloud are in the range from 10 μm to 100 μm. They are most often too small to be detected by centimetre-wavelength radars. Thus, millimetre-wavelength radars are necessary [23, 24].

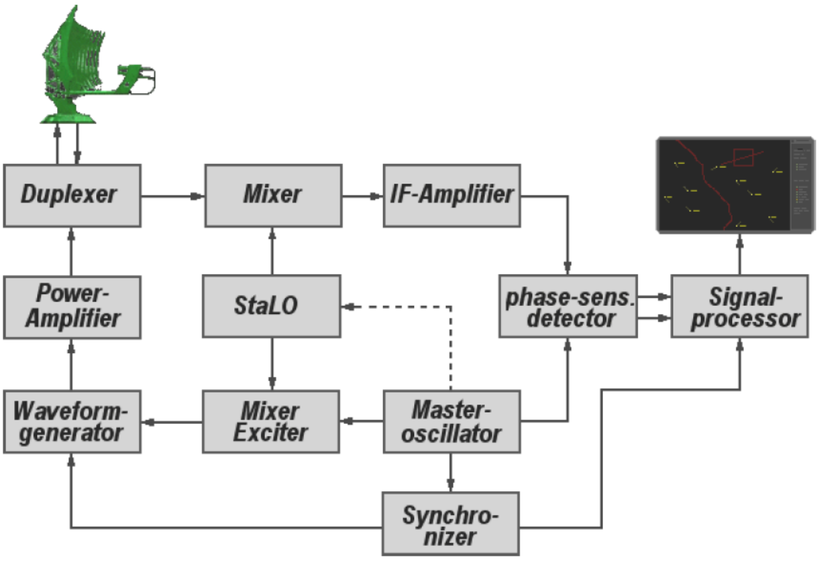

Figure 1.5 A block diagram of a fully coherent radar based on amplifiers [25].

Compared with microwave weather radar, millimetre-wave cloud radar is superior in measuring the clouds in the following ways: (1) it has higher sensitivity in detecting small particles like ice drop, fog, and dust; (2) it provides better precision of Doppler velocity; (3) it has higher spatial resolution due to its narrow beam width; (4) it has more compact and lighter weight. At present, Ka-band and W-band radar for cloud research has been proven to be an optimal choice in terms of maximum sensitivity and system compactness for ground-based, airborne and space borne radar systems [26, 27].

There are two main approaches to the development of coherent millimetre-wave radar systems: truly coherent radar and pseudo-coherent (also named coherent-on-receiver radar) [28]. The transmitter of the truly coherent radar is based on an amplifier, such as TWT and EIK driven by a highly stable oscillator [29, 30]. The block diagram is shown in Figure 1.5. The oscillator is used also as a reference source for the receiver, in which case the measurement of the backscattered signal phase is relatively easy. Such systems provide fairly good clutter suppression, a high Doppler resolution, and give a possibility of introducing sophisticated methods of pulse compression. However, the high cost limits its applications, especially in the civil areas.

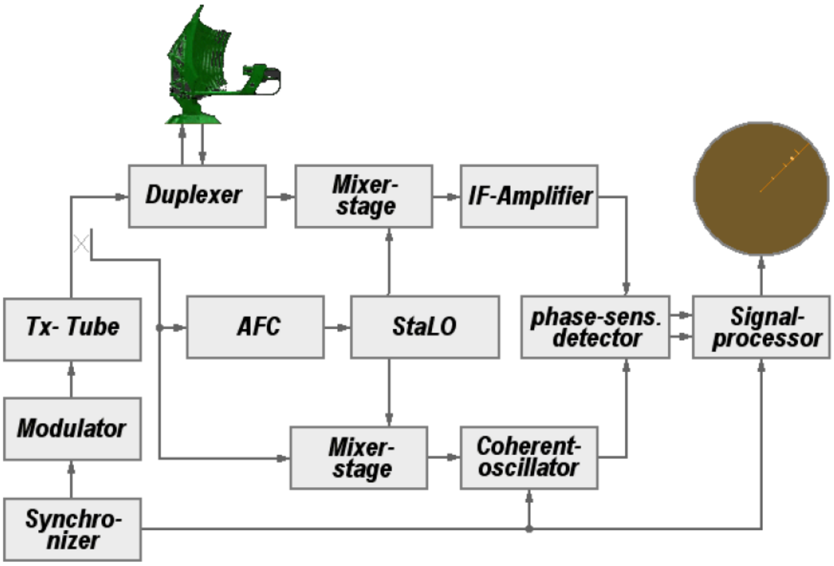

Figure 1.6 A block diagram of a pseudo-coherent radar based on oscillators [25].

Coherent-on-receiver approach deals with storing the values of the phase of the RF pulses emitted by the transmitter and comparing these values with those measured by the receiver, as shown in Figure 1.6. In this case, the transmitter can be based on a self-running oscillator such as magnetron. The recent advances in microprocessor development and digital signal processing allow the development of the coherent receiver systems with the capabilities similar to those provided by truly coherent systems [31] . The relatively low cost and complexity make it being a very attractive solution. But the problem lies in the lack of reliable long life time millimetre-wave magnetrons, especially W-band magnetron. VEDs such as TWTs and Klystrons have already been used in millimetre-wave radar systems. The requirement of smaller, lighter, and cheaper radiation source in the application of millimetre-wave cloud radar systems motivates us to research on the millimetre-wave magnetrons.

1.2.2 THz applications

The terahertz (THz) frequency range spans from 100 GHz to 10 THz in the electromagnetic spectrum. It lies in between the microwave band and the infrared region, as shown in. Although the scientists' attention had been paid to the THz radiation from at least 1920s, this part of electromagnetic spectrum has been poorly explored until recent years due to the lack of high power THz source and reliable detectors [32].

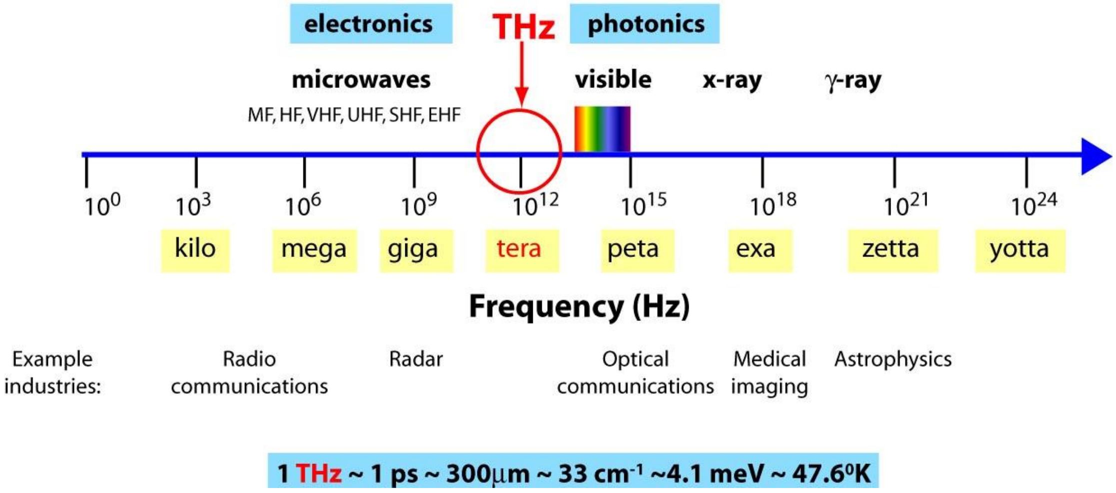

Figure 1.7 Schematic of the electromagnetic spectrum showing the location of THz band [32].

THz radiation has some unique properties. (1) It can penetrate a wide variety of visually opaque and non-conducting materials such as ceramics, clothing, wood and plastic. The penetration is non-ionizing since the photon energy level of 1 THz is about 4.14 meV which is much less than the energy of X-rays. (2) The short wavelength of THz wave has higher spatial resolution and signal-to-noise ratio than the microwave. (3) Many materials including explosives, chemical and biological agents have characteristic THz spectra that can be used as fingerprints for identifying these concealed materials. (4) It is readily absorbed by water.

Due to these unique properties, THz technology has a wide variety current and potential applications in high data rate communications [33], concealed weapon or threat detection [34, 35], remote high resolution imaging [36], materials research [37], astronomy [38], plasma fusion diagnostics [39], chemical and biology sciences[40].

In the past decades, the numerous THz sources have been developed. Most of them can be classified into three groups as Photonic devices, solid-state devices and vacuum devices. As for the low-frequency part of the THz region up to 1 THz, VEDs can be considered as high power THz sources for practical applications. So far, BWOs, EIKs, TWTs and Gyrotrons have been developed operating above 200 GHz [13]. However, most of these tubes require high magnetic field or complex structures which limits their developments for the practical applications. Magnetron which is the first proposed device in the VED families seems to be forgotten in this high frequency region.

1.3 Research Motivation

1.3.1 Limitations of conventional magnetron

The requirement of high power, low cost, and compact millimetre-wave and THz oscillators motivates us to explore the magnetron for high frequency operation. However, since the 1950s, it has become clear that conventional magnetrons do not operate effectively above Ka-band due to some inherent limitations [41]. The first one is the need to increase the number of the anode resonators to generate higher frequencies. However, large number of resonators will reduce the mode separation of the π mode. Metal straps connecting the alternate resonators are usually used to improve the mode separation as shown in Figure 1.8. But, as we know, the dimensions of the magnetron cavity scale as the wavelength λ. In millimetre wave and THz band, the anode cavity diameter is usually several millimetres. The strapped cavity is too small to be fabricated and assembled.

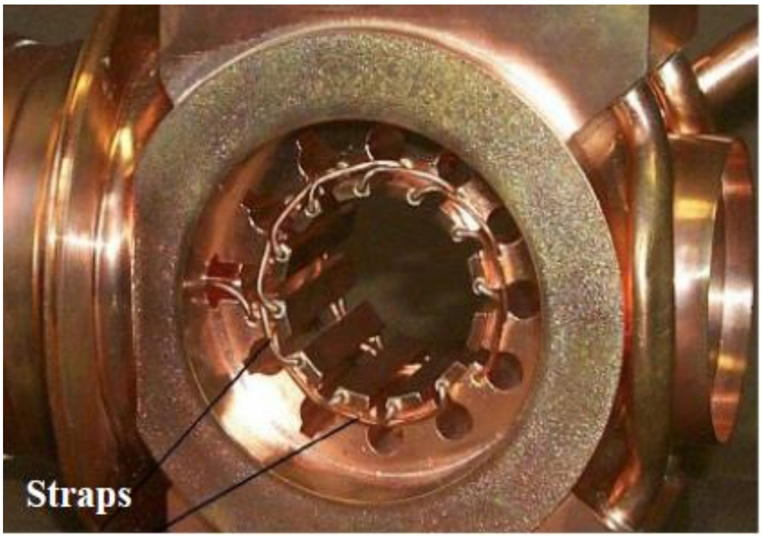

Figure 1.8 Wire strapping anode of an S band cavity magnetron [42].

The second limitation is the necessity of the high voltage and the high magnetic field. The required dc magnetic field and high voltage grow as 1/ λ. If the required magnetic field is higher than 2 T, it is hard to be realised by the permanent magnet. Also, these tubes require relatively high values of the anode voltage (>20 kV) which complicates the development of the compact power supplies and transmitters.

In conventional magnetrons, to obtain a large value of emission current, it is necessary to increase the cathode temperature. However, the cathode suffers intense electron back bombardment, which could overheat the cathode and the emission current is unstable. In addition, the intense electron back bombardment will deteriorate the status of the cathode surface. An intensive sublimation of the cathode naturally leads to spoiling the magnetron's resonant system and the contamination of the vacuum condition. The short life time is a serious problem of the conventional magnetron for the practical applications.

Therefore, in order to develop a millimetre-wave and THz magnetron, it needs to simplify the magnetron anode structure, reduce the required voltage and magnetic field, and extend the magnetron lifetime.

1.3.2 Spatial harmonic magnetron with cold secondary emission cathode

Spatial harmonic magnetrons (SHMs) with secondary emission cathode can be considered as the most successful alternative to conventional magnetrons. Different from conventional fundamental π mode magnetron, the SHM utilizes the first order backward spatial harmonic of a non-π mode (usually the $\pi/2$-mode or a neighbouring one) for its operation.

Figure 1.9 presents a dispersion diagram of a 16-vane magnetron cavity as studied in Chapter 3. It shows that $\pi/2$ mode has better mode separation than π mode which allows SHM has good mode separation even without any mode separation straps. The fabrication of this unstrapped anode becomes much easier.

According to the magnetron electron-wave synchronism theory, electrons require lower voltage to synchronize with high order spatial harmonic than the fundamental harmonic. At the same time, high order spatial harmonic locates closer to the anode surface, which means that the value of the operating voltage should be close to the cut off voltage. Thus, the operating point is close to both of the resonant voltage and cut off voltage, which reduces the required voltage and magnetic field.

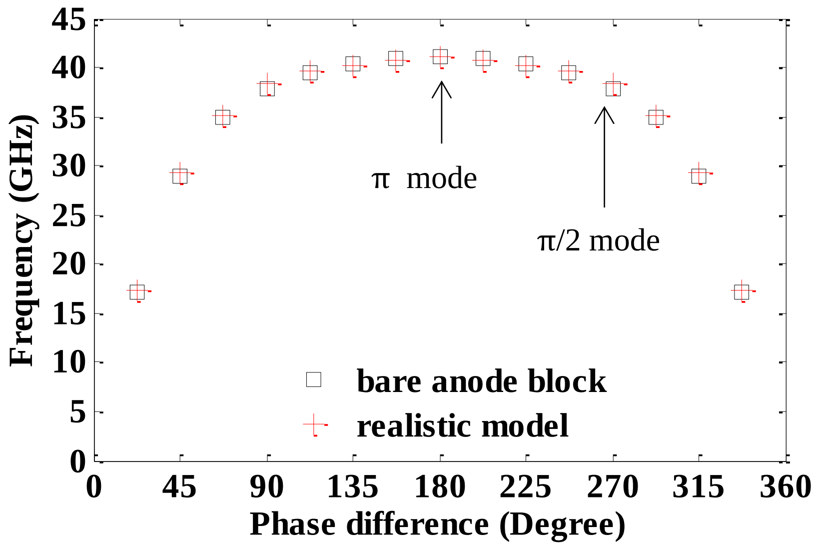

Figure 1.9 Dispersion diagrams of a 16-vane spatial harmonic magnetron (bare anode and anode cavity).

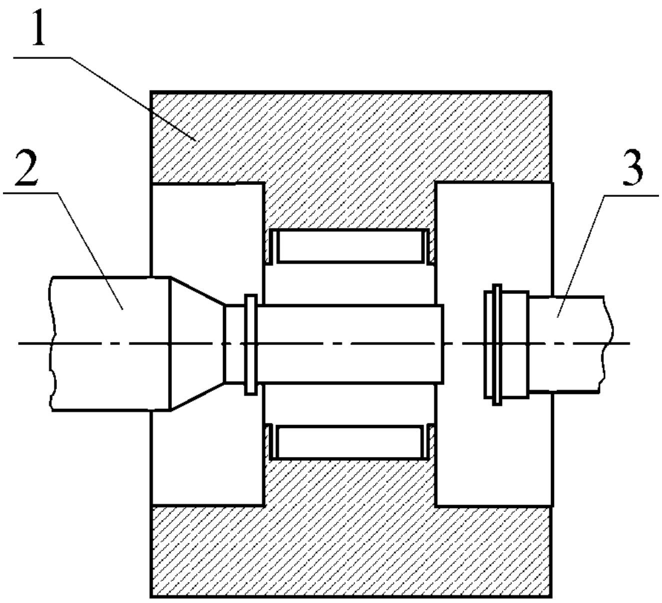

Figure 1.10 Schematics of the spatial harmonic magnetron [43].
1, anode; 2, cold secondary emission cathode; 3, axillary thermionic cathode.

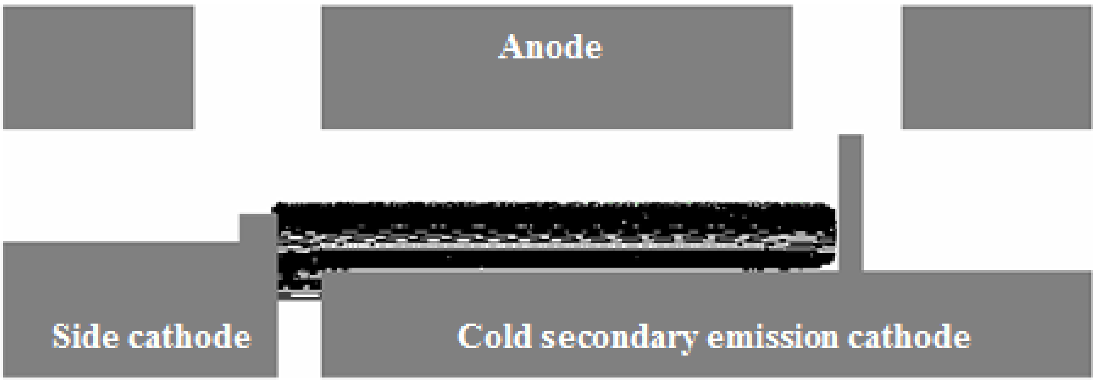

Figure 1.11 Electron injection from the auxiliary cathode to the interaction space [29].

Benefit from these advantages, the first millimetre wave spatial harmonic magnetron was developed in 1975 [44]. However due to L type oxide cathode was used, the life time was less than 50 hours. In order to improve lifetime, a cold cathode with electron secondary emission is introduced in the spatial harmonic magnetron [43]. As shown in Figure 1.10, there are two cathodes in the SHM: (1) a cold secondary emission cathode made from a copper core coated by platinum foil placed in the centre of the interaction space. (2) The other is an axillary thermionic cathode (also named side cathode) placed outside of the interaction space.

A very small amount of current, usually hundreds of mA, is emitted from the side cathode and injected into the interaction space during the anode voltage rising up period. These injected electrons accumulate surround the cold cathode and expand toward the anode with anode voltage increasing as illustrated in Figure 1.11. When the value of the anode voltage reaches the operating point, the electrons near the anode surface acquire sufficient velocity to interact with the RF field which cause an intense current strike back onto the cold cathode. Usually, more than 100 $\mathrm{A/cm^2}$ secondary emission current could be initialized from the cold cathode.

As the heat source is outside of the interaction space and there is no electrical or heat contacts with the cold cathode, the cold cathode runs relatively cool without any significant thermionic emission. The cold cathode is very robust even under intense electron bombardment. Therefore, the lift time of the SHM can be extended to thousands of hours by using cold secondary emission cathode.

1.4 Objectives

Although some of the Ka-band SHMs have already been used in practical could radar system, for a long time, the development and modifications of the SHM have been based on empirical rules accumulated from a large volume of experimental data. At present, a demand has arisen for a numerical analysis of such magnetrons that will allow studying in depth the physics of their operation with the aim of a further enhancement of their performance.

As introduced above, SHM is essentially different from the conventional magnetron in terms of structures and operating principles. In conventional magnetron, the space charges come from the primary electrons of the thermionic cathode, thus electron secondary emission is not considered in the numerical study of the magnetron operation. While in the SHMs, secondary electrons are the main contribution to the space charge. Electron secondary emission plays an important role in the operation of the SHMs. Therefore, the investigation of the electron back bombarding, electron secondary emission, electron-wave interaction, and space charge distribution in the SHMs are the essential tasks of this thesis.

In practice, to reduce the cost, the cold cathode is made of platinum coated on a copper core. It complicates the cathode fabrication in the millimetre-wave and THz band. According to the study of the magnetron performances with various electron secondary emission coefficients, it may open a way for the using of inexpensive pure metals for the cathode production with low cost and complexity.

Conventional magnetrons do not suffer strong mode competition since the fundamental π mode has the largest amplitude and the straps increases the mode separation. Thus, in the study of the conventional magnetrons, just fundamental π mode is considered and other modes can be neglected. However, the SHMs suffer strong mode competition since the amplitudes of the spatial harmonics are weaker than the fundamental ones and there is no additional mode separation strap. Thus, all of the modes should be included in the study of the SHMs. One of the objectives of this thesis is to investigate the mode competition and mode jumping of the SHMs.

According to the scale law, the cavity dimensions are much smaller in the high frequency region, taking a 209 GHz SHM for example (presented in Chapter 5), the anode diameter is 2.6 mm; the cathode diameter is 1.55 mm; the vane thickness is 0.07 mm. Therefore, the effect of the fabrication tolerance needs to be investigated in this thesis based on the simulation and measurement. Another objective is to build a simulation model of a SHM above 300 GHz for the development of a THz magnetron.

The particle simulation of the SHM is much complicated and time consuming than the conventional magnetron due to two cathodes and electron secondary emission. This thesis will develop an appropriate modelling method with sufficient accuracy and acceptable simulation efficiency to investigate 35 GHz, 95 GHz, 209 GHz, and 300 GHz SHMs.

1.5 Thesis Organization

The remaining part of this thesis is organized as follows:

Chapter 2 gives an introduction to the development and the operation principle of both conventional magnetron and spatial harmonic magnetron. Detailed discussions have been presented on the anode modes, spatial harmonic, thermionic cathode and cold secondary emission cathode, electron-wave interaction, and relationship between the anode voltage and the magnetic field.

Chapter 3 presents extensive simulation work on a Ka-band $\pi/2$-1 mode SHM. The electron dynamics and the distribution of the back bombardment currents have been studied. To speed up the simulation, a simplified modelling method is developed. The mode competition and the effect of the electron secondary emission coefficients are discussed. The mode jumping has been observed in the study of a Ka-band $\pi/2$ mode SHM.

Chapter 4 presents the investigation of a 95 GHz SHM based on the particle simulation and experimental measurement. The magnetron power supply has been introduced and a magnetron transmitter has been developed for the application of W-band cloud radar.

Chapter 5 investigates a 209 GHz SHM and primary emission domination state and secondary emission domination state have been discussed. An anode cavity has been fabricated and measured to investigate the effect of the fabrication tolerance on the performance of THz magnetron. A model of a SHM above 300 GHz has been built to further increase the magnetron frequency.

Chapter 6 concludes this thesis and suggests the future work as well as possible improvements.

Chapter 2 Operating Principle of Magnetrons

In this chapter, the operating principle of conventional magnetron and the SHM will be introduced. The operation principle of SHMs is essentially different from conventional magnetrons in terms of operating mode, anode structure and cathode. These differences allow SHM have larger anode dimensions, lower operating fields, and long life time.

2.1 Early Magnetrons

A review of the early magnetron development will be given here to show the significant steps that have led to the present high efficient magnetrons. The first magnetron was mentioned by Hull in 1921 [45]. These early magnetrons used anode that were cylindrical in shape (Figure 2.1 (a)). In 1929 Okabe developed the split anode magnetron, in which the anode was divided into two halves. But the output power and efficiency are very low [2]. In 1935 Posthumous deduced theoretically that in magnetrons with multi-segment anodes and large magnetic field, RF power should be generated with high efficiency. He then demonstrated an efficiency of about 50% in a magnetron operating at 600 MHz (Figure 2.1 (b)) [46, 47]. In 1938, a magnetron with a copper anode and hole-and-slot resonators had been built by Alekseroff and Malearoff. A tungsten helix cathode was used and the generated power was about 100W CW at a wavelength of 10cm [48]. In 1940 Randall and Boot at the University of Birmingham (UK) built a magnetron with an anode containing resonant cavities, and they called this device the cavity magnetron (Figure 2.1 (c)) [49].

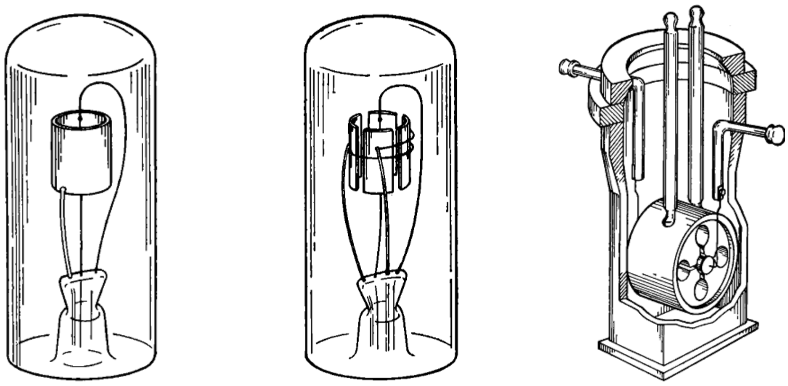

(a) **(b)** **(c)**

Figure 2.1 Early types of magnetrons (a) cylindrical diode (b) multi-segment anode magnetron (c) hole-and-slot resonator magnetron [50].

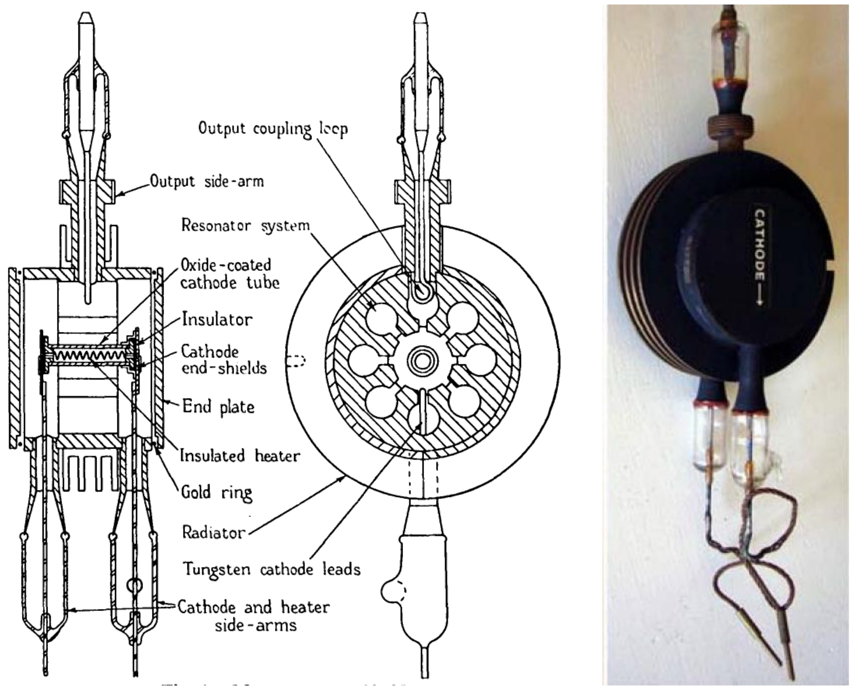

Figure 2.2 Early British cavity magnetron (NT98) [1].

These cavities generate an RF wave that travels at a phase velocity much less than the speed of light in order to allow for good synchronization with the electrons. This type of anode structure is called a slow wave circuit. In early 1940, an experimental radar system based on a pulsed 10-cm cavity magnetron was in operation, and by late 1940 a submarine periscope was able to be detected within a range of seven miles [1]. The early British pulsed cavity magnetron is shown in Figure 2.2. Since then, many microwave devices have been developed for the generation and amplification of microwave radiation. Magnetrons are used today in numerous applications such as radar, electron accelerator, electronic warfare, and microwave ovens [51].

2.2 Electron Motion

The electron trajectory and electron-wave interaction inside a magnetron have a very complicated mechanism. In this section a simplified planar diode and cylindrical diode will be discussed in the first to explain the basic kinetic motion of electron in a planar diode and cylindrical diode under the crossed electric and magnetic fields. On this basis the operation of magnetron will then be discussed in the following sections.

2.2.1 Electron motion in a planar diode

Figure 2.3 shows a schematic of a simplified planar diode consisting of two infinite large plane electrodes with potential difference of V_{dc}. The distance between the two electrodes is d. Thus, the electric field between the planar electrodes is $\vec{E} = \frac{\vec{V}_{dc}}{d}$. The direction of a uniform magnetic field B is normal to the electric field and parallel to the two electrodes.

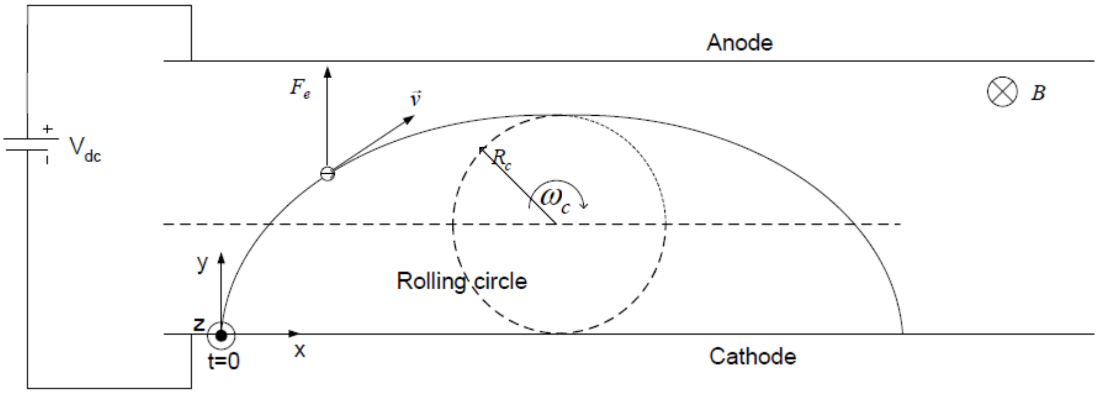

Figure 2.3 Electron trajectory in a planar crossed field diode [42].

An electron emitted from the cathode moves under the influence of electric force $\vec{F_e}$ and magnetic force $\vec{F_m}$between the anode and the cathode.

$$\vec{F_e} = e \cdot \vec{E} \tag{2.1}$$

$$\vec{F_m} = e\vec{v} \times \vec{B} \tag{2.2}$$

$$m\frac{d\vec{r}^2}{dt^2} = e(\vec{E} + \vec{v} \times \vec{B}) \tag{2.3}$$

In the Cartesian coordinate system, the electron motion equations can be rewritten as below:

$$e\vec{E} - e\vec{B}\frac{dx}{dt} = m\frac{d^2y}{dt^2} \tag{2.4}$$

$$e\vec{B}\frac{dy}{dt} = m\frac{d^2x}{dt^2} \tag{2.5}$$

Considering a simple condition that the electron starts with zero velocity ($v_{0x} = 0, v_{0y} = 0$) from the cathode, it can be seen in Figure 2.3 that the electron travels like a point on a circle rolling along the cathode surface with angular frequency ω_c

$$\omega_c = \frac{eB}{m} \tag{2.6}$$

Within one period $T = 2\pi/\omega_c$, the electron will complete a revolution and go back to the cathode. The radius of the rolling circle R_c is

$$R_c = \frac{mE}{eB^2} \tag{2.7}$$

The maximum distance an electron travel in x direction within one cyclotron period T is

$$x_{max} = 2\pi R_c = \frac{2\pi mE}{eB^2} \tag{2.8}$$

The electron motion can be approximately represented by superposing a slow drift motion along the cathode with the average drift velocity E/B and a cyclotron motion with the cyclotron angular frequency ω_c.

When an electron trajectory just grazes the anode, the cut off voltage is

$$U_c = \frac{e}{2m} B^2 d^2 \tag{2.9}$$

When the initial velocity of the electron is non-zero, the electron trajectory is quite different. Figure 2.4 shows the electron trajectories with different initial velocity components v_x and v_y, when *B*=0.4 T, U_a=5.7 kV, *d*=0.92 mm. In this diagram, electrons leave the cathode surface with zero velocity (curve 1), velocity normal to the cathode surface $v_x = 0$, $v_y = E/2B$ (curve 3), and velocity at 45^{o} to the normal (curve 2).

When the RF field is applied, the electrons will be either accelerated or decelerated. As shown in Figure 2.5, when an electron is accelerated by the RF field, the rolling circle of the cycloid path will increase; it will be deflected by the magnetic field sharply and strike back to the cathode quickly as demonstrated by cure “1”. This kind of magnetron will absorb energy from the RF field. When an electron is decelerated by the RF field, an electron will move horizontally with drifting velocity *E/B* as demonstrated by curve "2". This kind of electrons will give energy to the RF field.

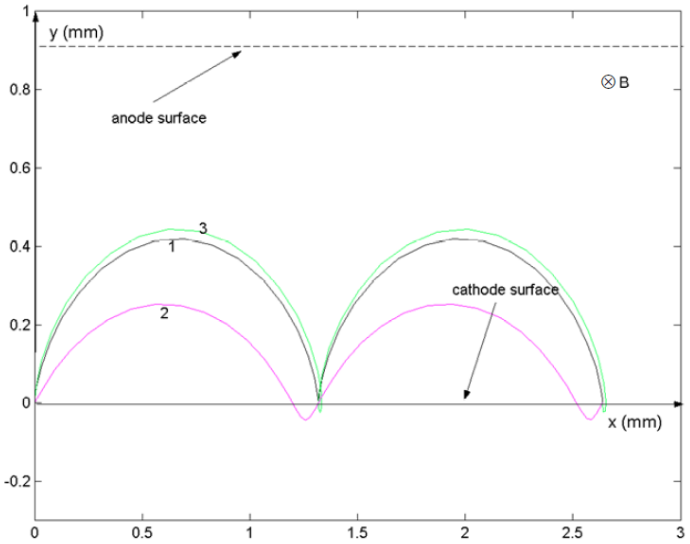

Figure 2.4 Electron trajectories with different initial velocities in a planar diode [42]. Curve 1: $v_x = v_y = 0$; Curve 2: $v_x = v_y = E/2B$; Curve 3: $v_x = 0,\ v_y = E/2B$.

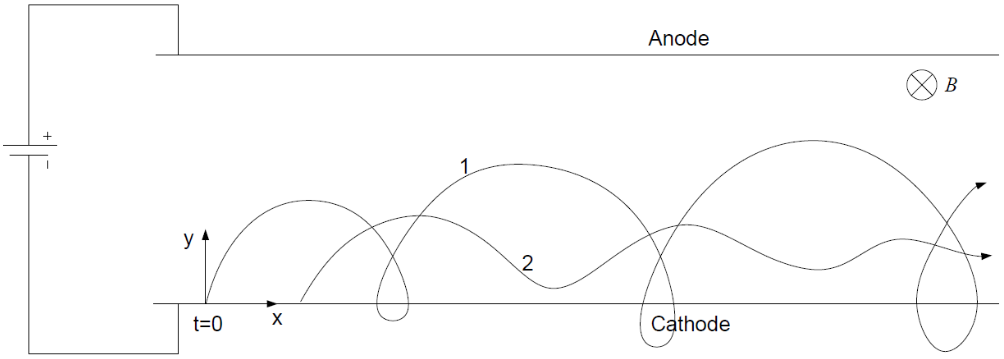

Figure 2.5 Electron trajectory in a planar crossed field diode [42].

2.2.2 Electron motion in a cylindrical diode

All the real magnetrons consist of coaxial cylindrical electrodes. Based on the above planar diode, a cylindrical diode with cathode radius r_c and anode radius r_a will be discussed here.

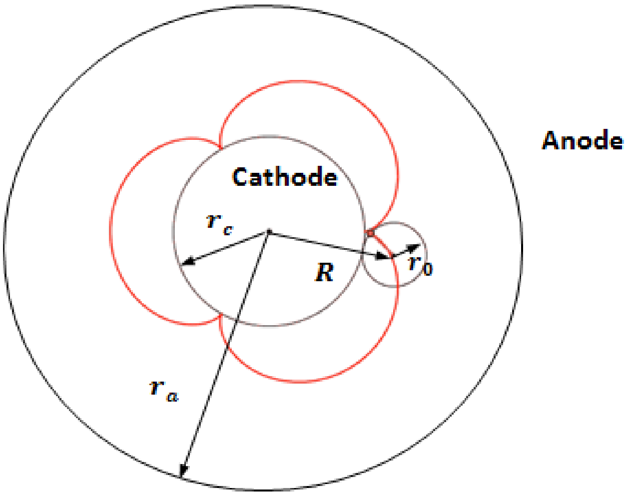

Figure 2.6 Electron motion in crossed field cylindrical diode.

The electron motion equations in a two dimensional cylindrical coordinates is given by

$$eE - eBr\frac{d\emptyset}{dt} = m\left[\frac{d^2r}{dt^2} - r\left(\frac{d\emptyset}{dt}\right)^2\right] \qquad 2.10$$

$$eB\frac{dr}{dt} = m\frac{1}{r}\frac{d}{dt}\left(r^2\frac{d\emptyset}{dt}\right) \qquad 2.11$$

Considering that the electron leaves the cathode surface with zero initial velocity, the electron angular velocity is then obtained

$$\frac{d\emptyset}{dt} = \frac{1}{2}\frac{eB}{m}\left(1 - \frac{r_c^2}{r^2}\right) \qquad 2.12$$

Figure 2.6 shows the electron trajectories in a cylindrical diode with zero initial velocity. It is an epitrochoid curve. When electron just grazes the anode (the radial velocity $\mathrm{v_r} = 0$), the electron velocity near the anode is

$$v_{\emptyset} = r_a \frac{d\emptyset}{dt} \qquad 2.13$$

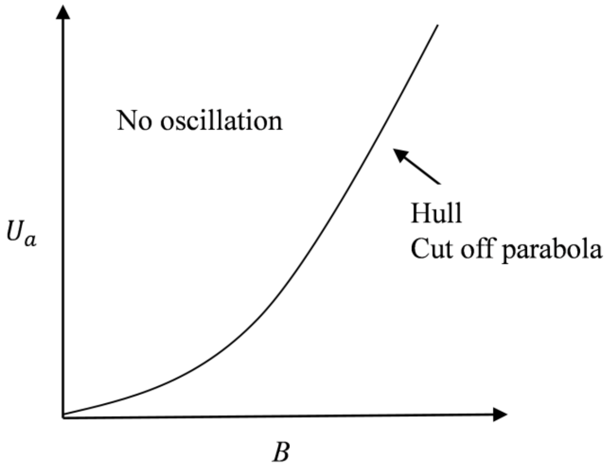

Figure 2.7 Hull cut off parabola of a static diode.

Substitute equation 2.13 to equation 2.12, the electron velocity at the anode is

$$v_{\emptyset} = \frac{1}{2}\frac{eB}{m} \qquad 2.14$$

According to the energy conservation, when the electron reaches the anode, its kinetic energy can be written as

$$\tfrac{1}{2}mv_{\emptyset}^2 = eU_a \qquad 2.15$$

Substituting equation 2.14 to 2.15, for a given magnetic field B, the cut off voltage is

$$U_c = \frac{e}{8m}r_a^2(1-\frac{r_c^2}{r_a^2})^2B^2 \qquad 2.16$$

Equation 2.16 is often called the Hull cut-off voltage equation [5]. When $U_a > U_c$, the electron strikes on the anode directly. When the anode voltage is below the cut off voltage, the electron trajectory is approximately in a form of epitrochoid which could be represented by superposing a slow guiding centre rotation around the cathode at nearly constant radius R (drift motion), and a faster rotating around the guiding centre with a smaller radius r_0 (cyclotron motion). Figure 2.8 shows electron trajectories in a cylindrical diode with r_a=2.25 mm and r_c=1.38 mm under 0.5875T magnetic field which are the operating parameters and dimension used for the Ka-band magnetron as presented in Chapter 3. The calculated cut off voltage is 16.8 kV.

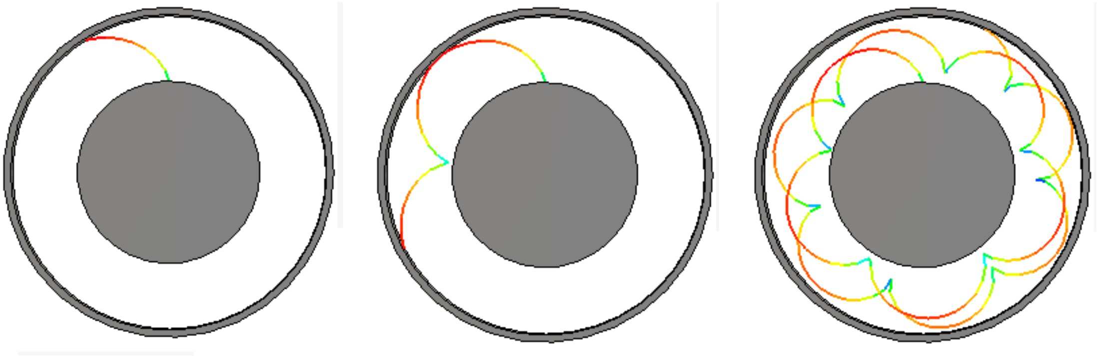

(a) U_a=18 kV ($U_a > U_c$) (b) U_a=16.8 kV ($U_a = U_c$) (c) U_a=12.8 kV ($U_a < U_c$)

Figure 2.8 Electron trajectories in a static cylindrical diode (r_a=2.25 mm, r_c=1.38 mm, B=0.5875 T) when the anode voltage is (a) above cutoff voltage (b) at cutoff voltage (c) below cut off voltage.

2.3 Oscillation Modes

In this section, the circuit theory is used to explain the range of possible RF oscillations. In a resonant cavity magnetron, individual cavities can be modelled as resonant circuits. An equivalent oscillating circuit of an eight-cavity magnetron is shown in Figure 2.9. ‘L’ and ‘C’ are inductance and capacitance representing a single side resonator. ‘c’ is the capacitance between the anode segments and the cathode.

The lines of magnetic flux in one individual cavity coupled to another cavity in the end spaces is represented by ‘M’ in the equivalent circuit.

The oscillation frequency of a side resonator is

$$\omega_0 = \frac{1}{\sqrt{LC}} \tag{2.17}$$

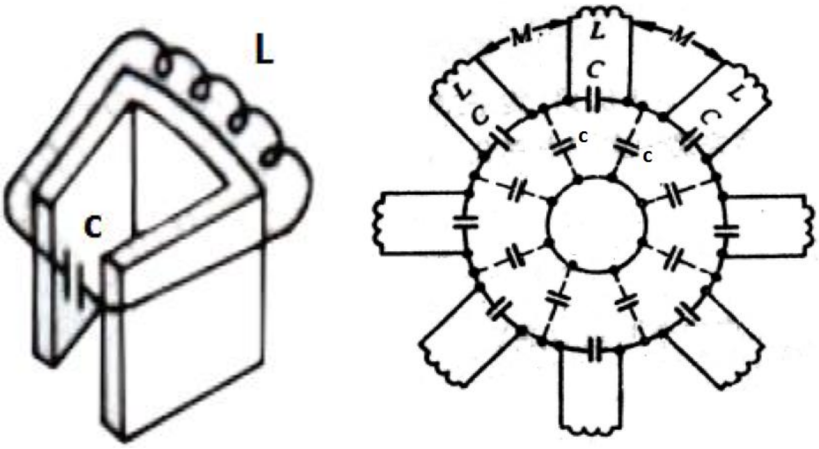

Figure 2.9 Equivalent circuit of an eight-cavity magnetron [50].

As the eight cavities are symmetrically distributed, the phase differences between adjacent side resonator are the same (labelled as $\emptyset$). In each side resonator, the oscillating voltage between the anode vanes can be described by

$$V_1 = V_m \, sin(\omega_0 \, t) \tag{2.18}$$

$$V_2 = V_m \, sin(\omega_0 \, t - \emptyset) \tag{2.19}$$

$$V_3 = V_m \, sin(\omega_0 \, t - 2\emptyset) \tag{2.20}$$

$$\dots$$

$$V_8 = V_m \, sin(\omega_0 t - 7\emptyset) \tag{2.21}$$

$$V_9 = V_m\, sin(\omega_0 t - 8\emptyset) \qquad 2.22$$

where V_m is the amplitude of the RF voltage.

Since magnetron anode is a closed circuit, when the system is oscillating, V_9 should be equal to V_1. This leads to $8\emptyset = 2\pi n$, (n=0,1,2,…). In general, the number of the side resonator is N, the phase condition for oscillations to exist is given by

$$N\emptyset = 2\pi n \qquad 2.23$$

Thus

$$\emptyset = \frac{2\pi n}{N} \qquad 2.24$$

Where n is an integer from 0 to N-1.

From Equation 2.24, it is obvious that there are several different modes that can satisfy the same phase condition for the oscillations to exist. Modes $n = N/2 + q$ and $n = N/2 - q$ (q = 1, · · · N/2) are pairs of degenerate modes. These modes are also called ‘doublets’. For a perfect symmetrical anode, the two components of a doublet would have the same wavelength. Thus, the total possible modes in a N-vane anode are from n=0 to N=N/2. When n=N/2, $\emptyset = \pi$, its corresponding doublet is the n=0 mode; this means zero charge on the anode segments, and the mode does not exist. Thus, for an eight-cavity magnetron (N=8), the possible modes are n=1, 2, 3, 4, where ‘n=4’ corresponds to the π mode. The charge and electric field distributions of these four possible modes are illustrated in Figure 2.10.

If ω is the resonant frequency of mode n, the time needed for traveling wave to travel around the anode for one round would be ‘nT’, where T = 2π/ω ; therefore its rotating frequency of mode *n* would be

$$\omega_n = \frac{\omega}{n} \tag{2.25}$$

So, the rotating phase velocity around the anode is slowed down by a factor ‘n’, which makes it possible for the electron to rotate in synchronism with the RF field.

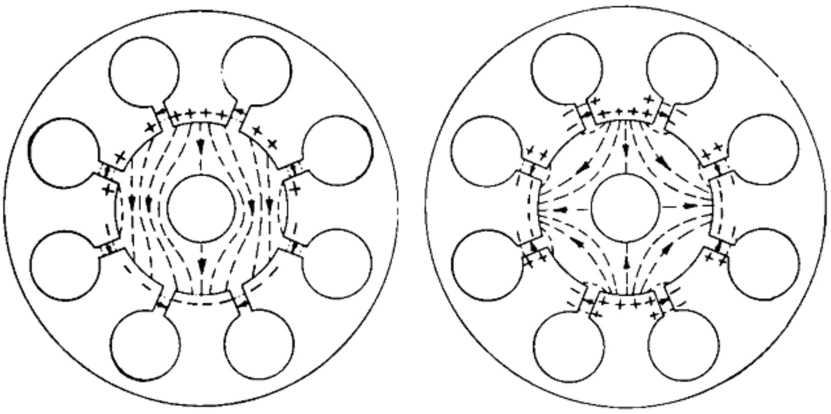

(a) n=1 **(b) n=2**

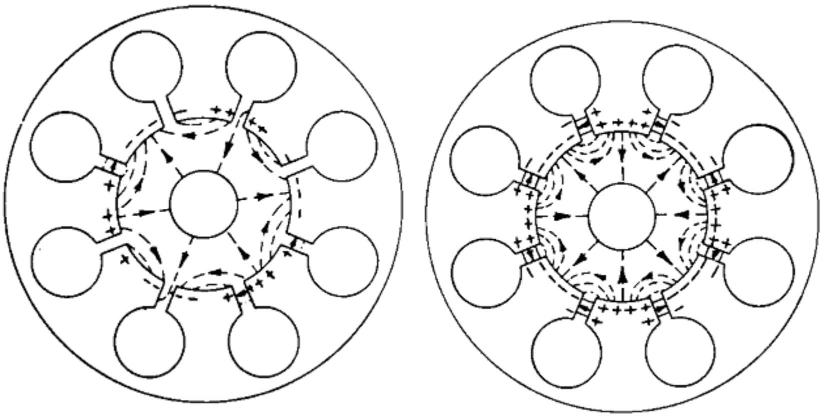

(c) n=3 **(d) n=4**

Figure 2.10 Field and charge distributions for different modes of an eight-cavity magnetron [50].

2.4 Increase of the Anode Diameter in SHMs

In this section, using the equivalent circuit approach, it will be shown that the anode diameter of a SHM is at least about 1.6 times larger than that of a π-mode magnetron which is of great importance at millimetre wave frequencies.

The equivalent circuit representation of a magnetron without straps is shown in Figure 2.11. In this network, the simple parallel resonant circuit represents the side resonators Figure 2.11 (a); the interaction space is also represented by a network which taken into account the capacitance “c” between the anode segments and the cathode.

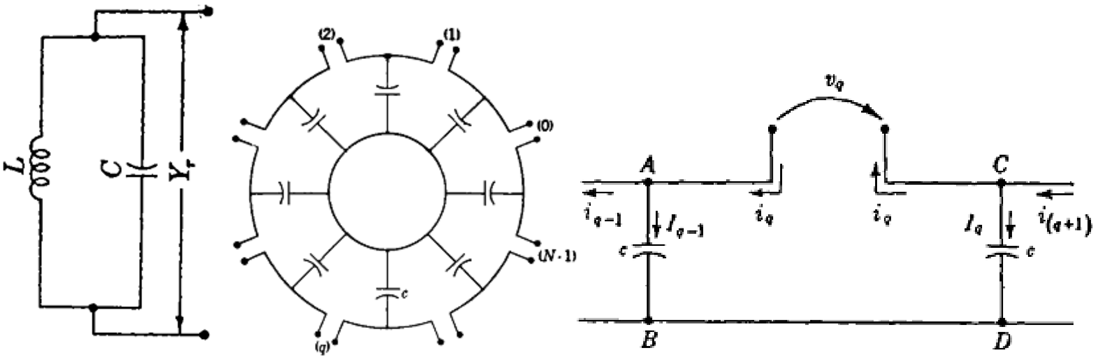

(a) **(b)** **(c)**

Figure 2.11 Equivalent network of (a) the side resonator and (b) the interaction space (c) a single section of the equivalent network of the interaction space.

Considering Figure 2.11 (c), the admittance looking from the q^{th} resonator into the interaction space is given by

$$Y = \frac{i_q}{v_q} \qquad 2.26$$

where

$$I_{q-1} = i_q - i_{q-1}, \qquad I_q = i_{q+1} - i_q \qquad 2.27$$

$$V_{AB} = \frac{I_{q-1}}{j\omega c}, \qquad V_{CD} = \frac{I_q}{j\omega c} \qquad 2.28$$

$$v_q = V_{AB} - V_{CD} \qquad 2.29$$

and thus

$$v_q = \frac{I_{q-1} - I_q}{j\omega c} = \frac{2i_q - (i_{q-1} + i_{q+1})}{j\omega c} \tag{2.30}$$

From the assumption that corresponding currents in adjacent sections differ only by a constant phase factor $\emptyset$, it follows that

$$i_{q-1} = i_q e^{-j\emptyset}, i_{q+1} = i_q e^{j\emptyset} \tag{2.31}$$

$$v_q = i_q \frac{2 - (e^{-j\emptyset} + e^{j\emptyset})}{j\omega c} \tag{2.32}$$

Since each section must be in phase with itself, $e^{jN\emptyset}$ must be equal to 1 and therefore $\emptyset = 2\pi/N$, where $n = 1,2, \ldots, N/2$ for the important magnetron modes. Using Equation 2.26 and 2.32, Y is calculated using

$$Y = \frac{i_q}{v_q} = \frac{j\omega c}{2(1 - cos\frac{2\pi n}{N})} \tag{2.33}$$

Considering the equivalent circuit of the side resonators Figure 2.11(a), resonance occurs if

$$-j\left(\omega C - \frac{1}{\omega L}\right) = Y_n = \frac{j\omega c}{2(1 - cos\frac{2\pi n}{N})} \tag{2.34}$$

Thus, the resonant frequencies of different modes are calculated as

$$\omega = \omega_0 \sqrt{\frac{1}{1 + \frac{\rho}{2(1 - cos\frac{2\pi n}{N})}}} \tag{2.35}$$

where,

$$\omega_0 = \frac{1}{\sqrt{LC}} \tag{2.36}$$

$$\rho = \frac{c}{C} \tag{2.37}$$

$$c = \frac{2\pi\varepsilon_0 h}{N\, ln(\frac{r_a}{r_c})} \tag{2.38}$$

where h, ε_0, r_a and r_c are the anode length, permittivity of vacuum, and the anode and cathode radius, respectively.

From Equation 2.35-2.38, the resonant frequencies of the π-mode (n=N/2) and the π/2-mode (n=N/4) are as follows:

$$f_{\frac{N}{2}} = \frac{\omega_0}{\sqrt{1 + \frac{c}{4C}}} \tag{2.39}$$

$$f_{\frac{N}{4}} = \frac{\omega_0}{\sqrt{1 + \frac{c}{2C}}} \tag{2.40}$$

Considering similar resonant frequencies f and similar side resonators (identical C values) for both the SHM ($\pi/2$ mode) and the classical magnetron (π mode), it follows that

$$\frac{r_{a-SHM}}{r_{c-SHM}} = \left(\frac{r_{a-classical}}{r_{c-classical}}\right)^2 \tag{2.41}$$

Where $r_{a-classical}$ and $r_{c-classical}$ are the anode and cathode radius of the classical magnetron, and $\mathrm{r_{a-SHM}}$ and $\mathrm{r_{c-SHM}}$ are the anode and cathode radius of the SHM. If assumes that $\mathrm{r_{c-classical}} = \mathrm{r_{c-SHM}}$ then

$$\frac{r_{a-SHM}}{r_{a-classical}} = \frac{r_{a-classical}}{r_{c-classical}} \qquad 2.42$$

For classical magnetron, $r_{a-classical}/r_{c-classical}$ is usually about 1.6 [50] and it should be mentioned that usually $r_{c-SHM} > r_{a-classical}$ [52]. Thus, the anode diameter of a $\pi/2$ mode magnetron can be up to 2 times larger than that of a π-mode magnetron.

2.5 Spatial Harmonic

Using Floquet theory, the RF field in periodical slow wave transmission line can be decomposed into infinite numbers of space harmonics by Fourier Transformation. It is similar with periodical signal which could be decomposed into infinite number of harmonics in time domain. The phase relationship between fundamental harmonic $\varphi_n = \frac{2n\pi}{N}$ and the m-th order spatial harmonic $\varphi_{n,m}$ is [53]

$$\varphi_{n,m} = \varphi_n + m2\pi \quad (|\varphi_n| \leq \pi \quad m = 0, \pm 1, \pm 2, \pm 3, \dots) \qquad 2.43$$

Thus, the phase change of m-th order spatial harmonic along the anode surface is

$$N\varphi_{n,m} = N(\varphi_n + m2\pi) = k2\pi \quad (k = n + mN) \qquad 2.44$$

Space harmonics with m=-1, m=0, and m=1 are called the first backward harmonic, the fundamental harmonic, and the first forward harmonic, respectively. The angular velocity of m-th spatial harmonic of the n-th mode is given by

$$\omega_{n,m} = \frac{\omega}{k} \qquad 2.45$$

In conventional magnetron, the rotating space charge synchronizes with the fundamental harmonic (m=0) while the synchronous harmonic in SHM is the first backward harmonic (m=-1). Comparing Equation 2.25 with Equation 2.45, at a given mode, the phase velocities of the space harmonics are much slower than that of the fundamental ones, $\omega_{n,m} < \omega_n$. Thus, the electrons require relatively lower magnetic field to be in synchronism with the spatial harmonic.

2.6 Hartree and Hull Voltages

When the magnetron is below the cut off voltage, the space charge is formed between the cathode and the anode. The synchronism condition requires that the electrons should rotate synchronously with the RF field at the anode surface, so that

$$\omega_e = \omega_{n,m} \qquad 2.46$$

ω_e is the electron angular frequency.

Applying this synchronous condition to the electron motion Equation 2.10 and 2.11 in a cylindrical coordinate system, the threshold voltage for RF oscillation to start in a magnetron can be obtained.

$$U_a = \frac{\pi f}{|k|}(r_a^2 - r_c^2)B - 2r_a^2 \frac{m}{e}\left(\frac{\pi f}{|k|}\right)^2 \qquad 2.47$$

This expression is also called the Hartree voltage, after Hartree who developed the theory. Rigorous solutions of this problem can be found in [2, 3]. The Hull cut off voltage in Equation 2.16 combined with Hartree threshold voltage in Equation 2.47 determines the operation zones of a magnetron. The magnetron operating region is above the Hartree line and below the cut off parabola. Typically, the operating point is quite close to the Hartree line in order to avoid spurious oscillations in higher voltage modes.

Figure 2.12 plots the Hull cut off voltage and Hartree threshold voltages for various k values in a 16-vane Ka-band magnetron as discussed in Chapter 3. For fundamental π mode, -1th spatial harmonic of π/2+1 mode, -1the spatial harmonic of π/2 mode, and -1th spatial harmonic of π/2-1 mode, values of k are 8, 11, 12, and 13 respectively. It indicates that SHMs operating on -1th spatial harmonic with large k value require lower threshold voltage. Therefore, spatial harmonic magnetron is a kind of low field magnetron.

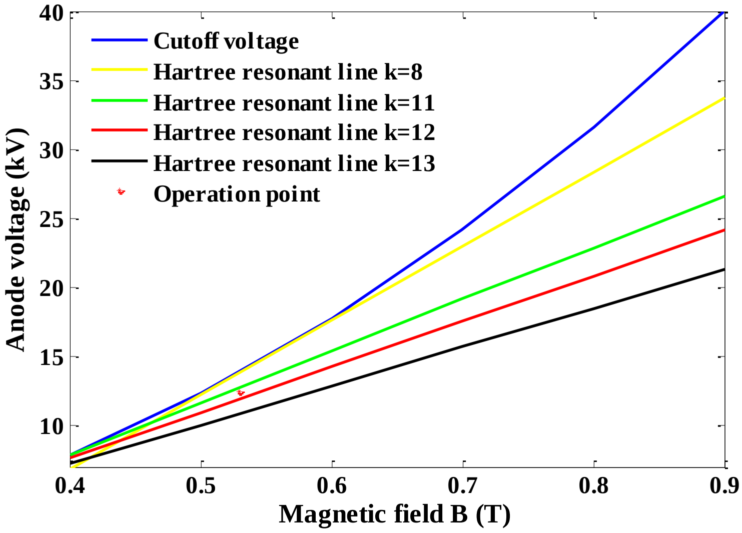

Figure 2.12 Hull cutoff voltage and Hatree threshold voltages for various k values in a 16-vane Ka-band SHM.

2.7 Electron Bunching and Back Bombardment

The electrons at different positions relative to the RF field have difference trajectories. The electron-wave interaction results in the formation of electron bunching. Figure 2.13 illustrates four typical initial positions of electrons emitted from the cathode which are labelled as “1” “2” “3” “4”.

Electron “1” is speeded up in the accelerating RF field, so the curvature of its trajectory will be increased. Under the combination effects of static electric field and magnetic field, electron “1” will strike back to the cathode quickly and thus be removed from the interaction region. This electron does not contribute energy to the RF field. On the contrary, it will consume a small amount of RF energy.

Electron ‘3’ is in the decelerating RF field. Its angular velocity is reduced, resulting in the reduction of its curvature. Such electrons move towards the anode. If the frequency of the RF field is appropriate, this electron will always be in the decelerating RF field when it passes through the successive anode segments. This electron will keep giving out energy to the RF field until it finally strikes the anode.

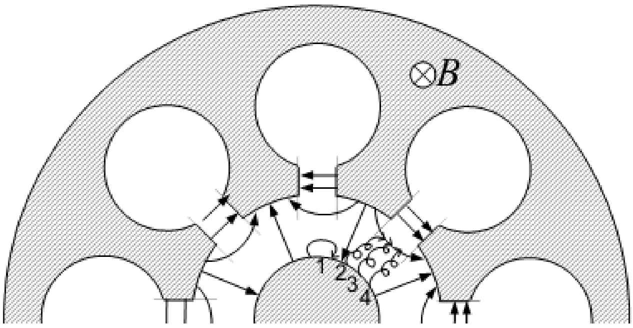

Figure 2.13 Electron trajectories in the RF field [6].

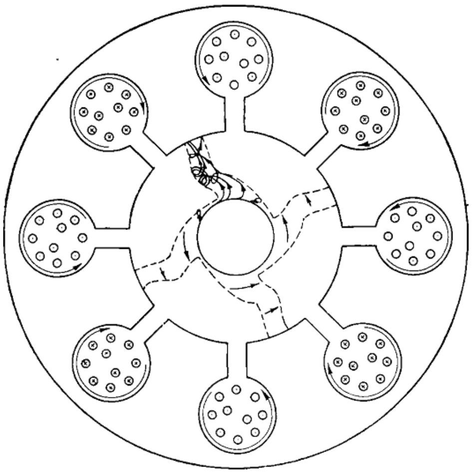

Figure 2.14 space charge focusing in oscillating magnetron.

Electrons ‘2’ and ‘4’ exchange little energy with the RF field. The effect of the RF field is to tune the velocity of their guiding centres. For electron ‘2’, this velocity is increased, thus its guiding centre will catch up that of electron ‘3’; but for electron ‘4’, its guiding centre velocity is reduced, thus it will fall back towards electron ‘3’. The final result is that electron ‘2’ and ‘4’ move into the decelerating region, and bunch together with electron ‘3’.

Electrons giving up energy to the RF field are called favourable electrons. Electrons absorbing energy from the RF field are called unfavourable electrons. The favourable electrons, which are in the majority, tend to bunch and move towards the anode while rotating around the cathode. When the oscillations are stabilized, the electron cloud is shaped into several spokes rotating around the cathode and continuously gives out energy to the RF field. It can be shown in Figure 2.14 that the number of the electron spokes is equal to the number of complete periods of the synchronous harmonic, i.e. k. Considering Equation 2.44 k is equal to 4 (m=0 and n =4) for a conventional 8-cavity magnetron.

The unfavourable electrons tend to be removed from the interaction region rather quickly and back bombard to the cathode with a considerable high energy. Consequently, secondary electrons are ejected from the cathode into the interaction space. By such repeated interactions of electrons with the cathode surface, it has been possible, in some cases, to obtain many times more total anode current from a cathode than could be supplied by the primary thermionic emission alone.

2.8 Thermionic Cathode and Cold Secondary Emission Cathode

The conventional magnetrons employ a thermionic cathode, while the SHMs employ a cold secondary emission cathode which is initialized by an auxiliary thermionic cathode. For thermionic cathode, the work function and temperature are critical parameters in determining the ability of the current emission. When the cathode is heated, some electrons have sufficient energy to overcome the potential barrier (work function) and escape out of the cathode surface.

The work function is the summation of energy inhibiting the escape of an electron from the cathode surface, which is due to the positive charge of the lattice attracting the electrons to the material. The typical units for work function are in electron-volts (eV). Therefore, to increase the electron emission rate, the materials with lower work function and high melting temperature are commonly used, such as barium, tungsten and nickel, as listed in Table 2-1 [47].

Table 2-1 Room temperature work function for various metals [47]

Metal	Work function (eV)	Melting temperature (^{o}C)
Copper	4.3	1083
Tungsten	4.6	3370
Gold	4.8	1063
Platinum	6.3	1773
Nickel	5	1445
Barium	1.8	720
Tantalum	4.1	2850
Strontium	2.0	800
Molybdenum	4.2	2620

In fact, the space charge and external DC electric field also have strong influence to the cathode emission ability, as they could affect the potential on the cathode surface. The potential reduction due to the negative space charge can be appreciable. As the electron emission rate is increased (by increasing temperature, for example), the potential on the cathode is further decreased. At a certain moment when a sufficient number of electrons are present, an equilibrium condition occurs when the potential adjacent to the cathode surface is zero. Then the cathode temperature and surface condition have no effect on emission. This emission is said to be space charge limited.

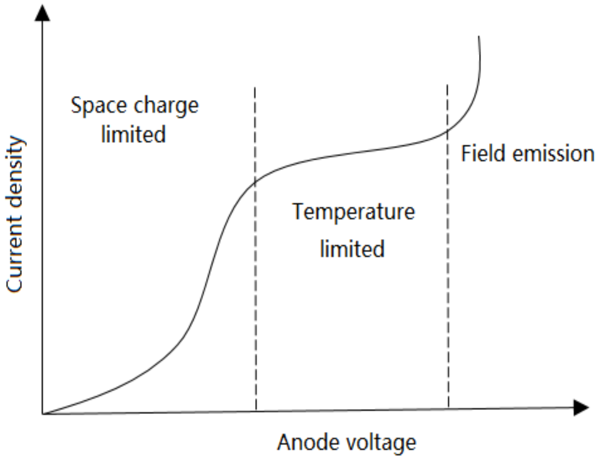

Figure 2.15 The relationship of anode voltage and emission current of the thermal cathode.

This is a very fortunate situation because it eliminates the necessity for extreme uniformity of temperature across the surface of a cathode. Thus, it eliminates the precise control to the heater of the cathode. When the anode voltage is increased with a space charge limited cathode, the potential at all points between the anode and cathode tend to increase. As a result, additional electrons flow from the cathode to cause the electric field at the cathode surface to remain at zero. When the voltage is increased to a high enough value so that the cathode cannot supply sufficient current to maintain the space charge limited condition, the cathode is said to be temperature limited as shown in Figure 2.15. When the electric field at the cathode surface increases to the level of 10^9-10^{10} V/m, electron emission increases rapidly almost independents of cathode temperature. This kind of emission type is named field emission which is not used commonly in magnetron. The primary reason is that to achieve the high electric field levels necessary for substantial emission, it has been necessary to fabricate the cathodes from array of very small needle-shaped emitters. The needle shape is used to enhance the electron emission so that emission occurs at the tip of each emitter.

Thermionic oxide cathodes are usually prepared by coating a base-metal structure (nickel or nickel alloys) with a definite weight of alkaline earth oxides (Barium Carbonate ($BaCO_3$), Strontium Carbonate ($SrCO_3$) and Barium Strontium Carbonate $BaSr(CO_3)_2$). These oxide cathodes have a short lifetime which is insufficient for practical applications due to the intense current density occurring in millimetre-wave magnetrons and the low coating resistance to the high-energy back-bombarded electrons.

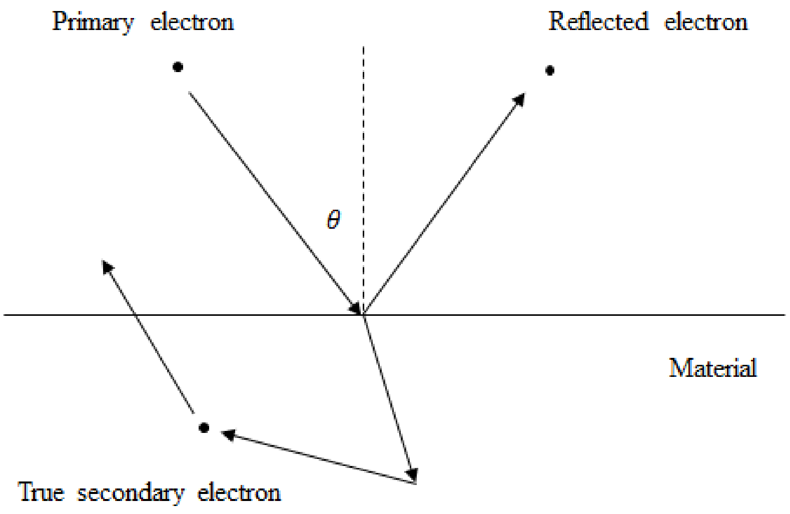

Figure 2.16 Schematic of electron secondary emission.

In order to improve the life time, cold secondary emission cathode is used in the SHMs. In the secondary process as shown in Figure 2.16, when a primary electron strikes a solid, it gives up energy by repelling electrons within the solid. The electrons within the solid thereby gain energy and may or may not be emitted, depending on how much energy they receive, how close they are to the surface, and direction of their motion. The amount of secondary emission depends on the secondary emission coefficient δ and on the impact energy V_b and angle of incidence θ of the primary electrons as shown in Figure 2.17.

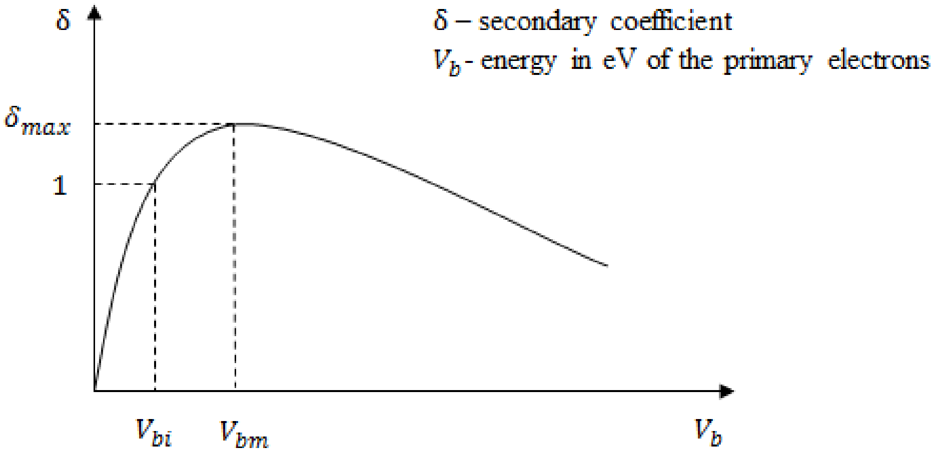

Figure 2.17 Typical curve of secondary emission coefficient versus incident electron energy (normal incidence $\theta = 0$).

Table 2-2 Secondary emission properties of several pure metals [54]

Metal	δ_{max}	V_{bi} (eV)	V_{bm} (eV)	Melting (°C)	Room temperature work function (eV)
Molybdenum	1.2-1.3	150	400	2620	4.2
Tungsten	1.2-1.4	200-300	500-700	3370	4.6
Copper	1.2-1.3	100-200	300-500	1083	4.3
Gold	1.2-1.4	200	400-1100	1063	4.8
Sliver	1.5	200	800	960	4.6
Nickel	1.3-1.4	200	500	1455	5
Platinum	1.7-1.8	200	900	1773	6.3

Under the conditions of good vacuum and arcing free operation, the secondary emission properties of the pure metal is very stable [6]. Table 2-2 lists the secondary emission coefficient for several common metals. It can be seen that platinum has relatively high secondary emission coefficient.

The description of platinum secondary emission process is complicated by the lack of an adequate mathematical model. Usually, experimental data is used to establish relations between primary and secondary electrons. To obtain the properties of platinum secondary emission, the following assumptions are applied in accordance with [55] and [56]. The platinum secondary electrons can be divided into two groups [55]: true secondary-emission electrons driven out of the platinum cathode, and primary electrons inelastically reflected from the cathode surface. Both the true secondary emission coefficient δ_t and the inelastic reflection coefficient δ_η depend on the incident energy E_0 and the incident angle θ of the primary electron.

During the starting stage of the oscillation, the incident electrons are near the cusps of the cycloidal loops, which are approximately normal to the cathode and there is no appreciable effect of the incidence angle [56]. The secondary emission coefficient versus impact energy E_0 for normal incidence angle ($\theta = 0$) is approximated given by [55]

$$\delta_t(E_0)=\begin{cases} \sqrt{5E_0}, & E_0 < 0.3keV \\ 1.39\text{-}0.8(0.8\text{-}E_0)^2, & 0.3keV \leq E_0 \leq 1keV \\ 1.57e^{-0.14E_0}, & E_0 \geq 1keV \end{cases} \qquad 2.48$$

$$\delta_r(E_0) = 0.47(1 - e^{-2.3E_0}) \qquad 2.49$$

The comparison between the approximated Equation 2.48, 2.49 and the measured results is given in Figure 2.18 and Figure 2.19 [57]. The good agreement could verify that equation 2.48 and 2.49 are accurate enough to mimic the platinum secondary emission properties.

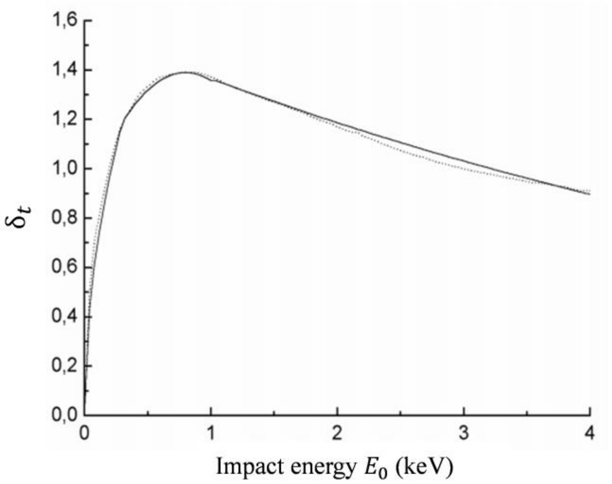

Figure 2.18 Comparison of platinum truly secondary emission coefficient δ_t between experimental data (dotted line) and the Equation 2.48 [57].

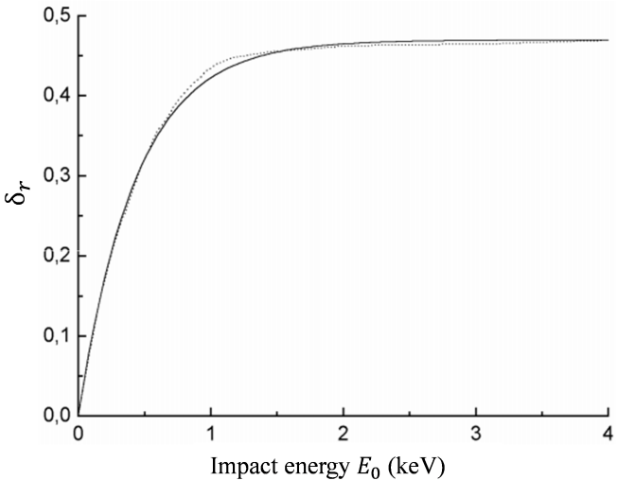

Figure 2.19 Comparison of platinum inelastic reflection coefficient δ_r between experimental data (dotted line) and Equation 2.49 (solid line) [57].

2.9 Frequency Stability and Mode Separation

2.9.1 Strapped anode and rising sun anode

The π mode is always selected as the operating mode in a magnetron. Unfortunately, the mode separation between π and other modes is not as great as would be desired if the anode cavity is without any additional mode separation approaches as shown in Figure 2.20 (a). It may cause the oscillation unstable or even fail to start. In order to improve the mode stability, strapped (Figure 2.20 (b)) anode and rising sun anode (Figure 2.20 (c)) are commonly used.

In strapped anode as shown in Figure 1.8 and Figure 2.21, alternate anode segments are connected together to help to make the phase difference between them to be zero or 2 π, thus enforcing the anode to work in the π mode. According to the circuit theory, strapping affects the capacitance and inductance of the equivalent circuit, which determines the resonating frequency of the anode system. When operating in π mode, all the segments connected to one set of straps are at the same potential. There will be no current flowing along the straps. But since the two sets of straps are at different potentials, there will be effective capacitance in parallel with the resonator capacitance, which increases the wavelength. When operating in non- π modes the two ends of a strap are at different potentials. There will be net current flowing along the straps. The magnitude the current depends on the potential difference between the ends. The straps therefore act as inductive path, connected in parallel with the effective resonator inductance, the wavelength is therefore reduced. The effect of strapping is therefore that the frequencies of the non-π modes are increased and that of the π mode is decreased. So, by tuning the strapping system, the π mode and non-π modes can be separated appreciably as shown in Figure 2.20(b). However, in millimetre-wave and THz band the small strapped anode is very difficult to be constructed and also prone to arcing.

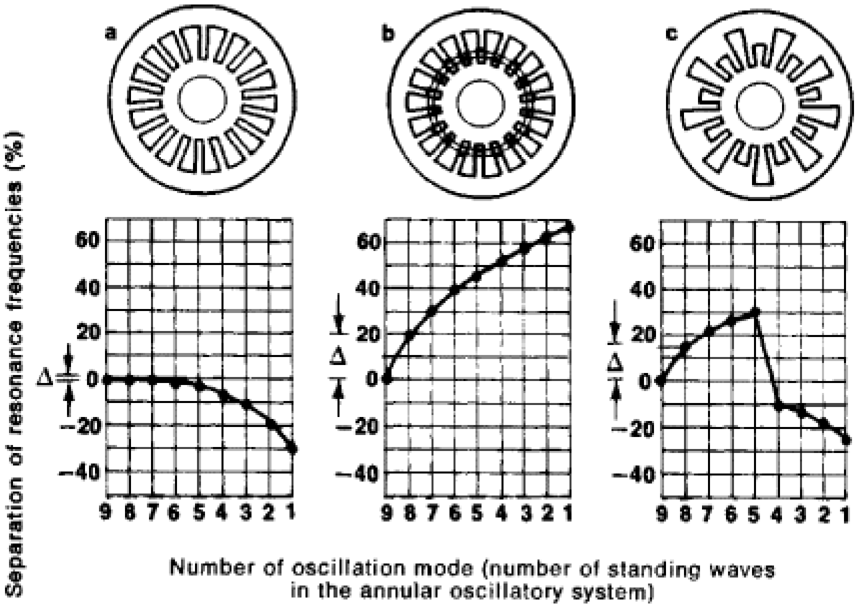

Figure 2.20 Mode separation of 18-cavity anode cavities operating on π mode (n=9). (a) Bare anode ; (b) strapped anode; (c) rising sun anode [50].

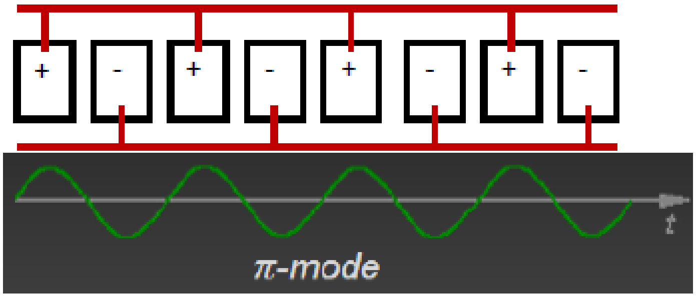

Figure 2.21 Alternate anode segments at same potential for π mode strap [42].

The rising sun can be considered as having two resonating systems, one consisting of small cavities with high frequencies and the other of large cavities with low frequencies. Naturally coupling exists between the two resonant systems. The resonant frequency of a rising sun anode is between those of the small and large cavities. By adjusting the ratio of the frequencies of the small and large cavities, the optimum frequency separation between π mode and other modes can be obtained (Figure 2.20 (c)).

2.9.2 Increase of the mode separation by non-π mode operation in SHMs

SHMs are operated on non-π mode (usually π/2 mode or π/2-1 mode) rather than π mode. The non-π mode operation enable SHMs have a naturally good mode separation constructed without any additional mode separation approaches. The simple anode structure is possible to be realized in millimetre and THz band. Figure 1.9 shows a dispersion diagram of a 16-vane unstrapped anode cavity of a Ka-band SHM which will be discussed in Chapter 3. The π/2-1 mode (point b) has much better mode separation than π mode (point a). From the cold simulation results in Chapter 3, the mode separation of $\pi/2-1$ mode is 8.3%, which is around 22 times higher than that of π mode (0.36%).

2.10 Summary

This chapter introduces the operation principles of the conventional magnetron and the spatial harmonic magnetron. As introduced above, the operating mode, operating harmonic, anode structure, cathode, and resonance condition of the SHMs are all different from that of conventional magnetrons. The comparison between conventional magnetron and the SHM is summarized in Table 2-3. The SHMs have the advantages of simple anode structure, long lifetime cathode, and low field operation.

Table 2-3 Comparison between conventional magnetron and spatial harmonic magnetron

	Conventional magnetron	Spatial harmonic magnetron
Mode	π mode n=N/2	π/2 or its neighboring mode n=N/4 or N/4±1
Spatial harmonic	Fundamental harmonic (m=0)	First backward spatial harmonic (m=-1)
Mode separation	Straps or rising sun	Without mode separation structure
Cathode	Thermionic cathode	Cold secondary emission cathode initialized by thermionic cathode
Field period ($k=n+mN$)	k =N/2	k =3N/4 or 3N/4∓1
Anode voltage	U	$U/4$ - $U/2$
Magnetic field	B	$B/4$ - $B/2$

Chapter 3 Spatial Harmonic Magnetron in Ka Band

This chapter presents 3-D particle simulations of a 35 GHz π/2-1 mode spatial harmonic magnetron with thermionic side cathode and cold secondary emission main cathode. Transient behaviour and steady state of the oscillations, electron back bombardment, electron secondary emission and the effect of the side cathode are investigated in simulation. To speed up the simulation, a simplified model has been developed to examine the effects of the cathode secondary emission coefficient and the anode quality factor. In addition, the mode stability in a π/2 mode SHM is investigated.

3.1 Introduction

In the SHM, the side cathode provides an electron beam in the axial direction into the interaction space. The space charge in the interaction space interacts with the RF field in the crossed plane. Therefore, the modelling of the SHM should be considered in 3D rather than 2D.

Despite a large number of papers devoted to the numerical simulation of the nonlinear beam-wave interaction dynamics of in the conventional magnetrons through the use of commercial simulation software or in-house developed codes [58-61], investigation of nonlinear interaction in the case of SHMs has been addressed in just a few publications mainly based on self-consistent mathematical model [55] and equivalent network approach [62]. The self-consistent mathematical model considers only the fundamental and first backward harmonic of the operating mode and neglects all other higher harmonic. It prohibits the possibility of examining mode competition and build-up process of the oscillation. A 3D simulation of 20-vane SHM was studied in [63] by the use of MAGIC. But the electron secondary emission was not taken into account.

As is known, the conventional magnetron operating on the fundamental spatial harmonic has the largest amplitude and it has relative weak mode competitions due to the strapped anode. Therefore, RF priming or pre-injection of a finite-amplitude RF signal of π mode neglecting all other modes is a popular method in the particle simulation of conventional magnetron. This technique could considerably reduce the simulation time. However, in the SHMs, the -1th spatial harmonics are always weaker than the fundamental one. Therefore, the influence of the fundamental harmonics should not be neglected. In addition, RF priming eliminates the natural formation of spokes from electromagnetic noise, and even more important, it prevents analysing the important characteristics of magnetrons such as mode competition.

In order to reveal the physics of the SHM, the simulation is performed by the use of CST Particle Studio without artificial RF priming and restrictive assumptions on the mode of operation or on the number of harmonics to be considered. Hence, it enables us to investigate not only the steady state, but also the transient behaviour of the magnetron. The software is based on the finite integration technique (FIT) and particle in cell (PIC) algorithm for a 3D analysis of charged particle dynamics in EM fields. It is able to self-consistently solve the full set of time dependent Maxwell’s equations and the complete Lorentz force equations through the use of a PIC code [64].

The PIC method as the name suggests defines macro particles inside a physical domain discretized by a mesh. The macro particle can be looked as a cluster of particles with the same charge mass ratio of a single electron. The idea is to solve for the scalar potentials or fields in the entire physical domain using Finite Integration Technique (FIT) with appropriate initial and boundary conditions and interpolate the force exerted by these fields on all particles that lie inside the corresponding mesh cell. Once the force on each particle is known, the motion equations are integrated to get the new particle positions and velocities. The charge carried by each macro particle is then assigned to the cell nodes in which it lies. To complete the interaction between particles and EM fields, the particle movement is written back as current to the Maxwell equations. The above procedure is repeated in each time step. The general PIC computational cycle for the interaction between electrons and electromagnetic field is shown in Figure 3.1.

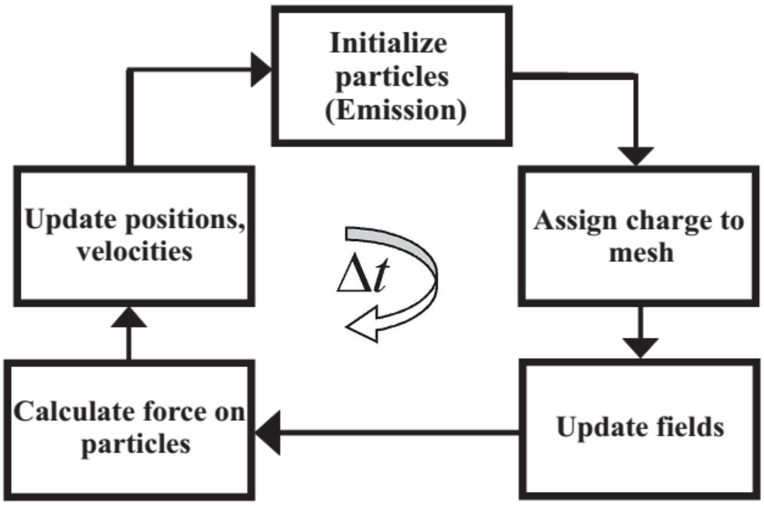

Figure 3.1 Particle in cell computational cycle [65].

3.2 Investigation of a 35GHz π/2-1 Mode SHM

3.2.1 Simulation model

The simulation model build in Cartesian coordinate system (x y, z) in CST Particle Studio is shown in Figure 3.2. The most important geometrical dimensions of this model were determined from the practical geometry of a 35 GHz π/2-1 mode SHM reported and investigated both theoretically and experimentally in [55]. The model consists of the following parts: (1) a 16-vane unstrapped anode block, assuming that the conducting material has a conductivity $\sigma = 5.8 \times 10^7$ S/m which corresponds to that of copper; (2) a Ka-band (WR-28) rectangular output waveguide; (3) a quarter-wavelength transformer, located between the WR-28 waveguide and one of the side resonators, which is used for the impedance matching and RF power coupling; (4) an auxiliary thermionic cathode (also named side cathode) placed out of the interaction space, which is to inject a small primary current into the interaction space; (5) a platinum cold secondary emission cathode (also named main cathode) located in the centre of the interaction space, which is to generated a large secondary emission current; (6) to prevent electron leakage in the axial direction, a pair of nonmagnetic endcaps are located at the ends of the main cathode. The geometrical parameters are presented in Table 3-1. The magnetic field circuit is not introduced in this model. Instead, the axial magnetic flux with a uniform profile is provided by an external magnetic field source.

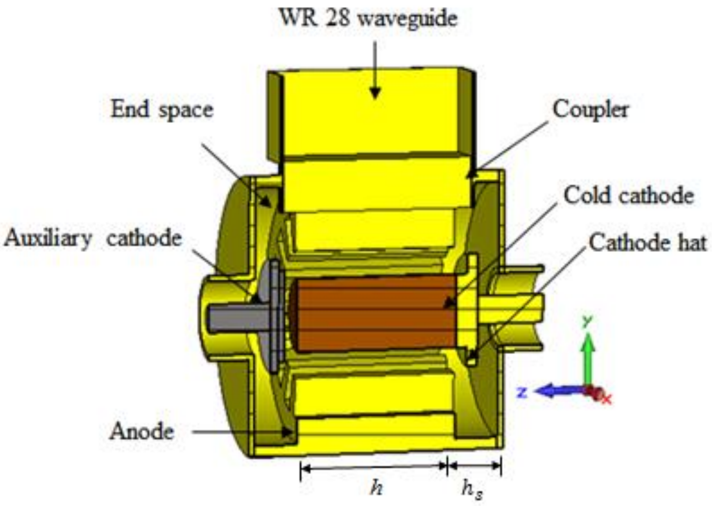

(a)

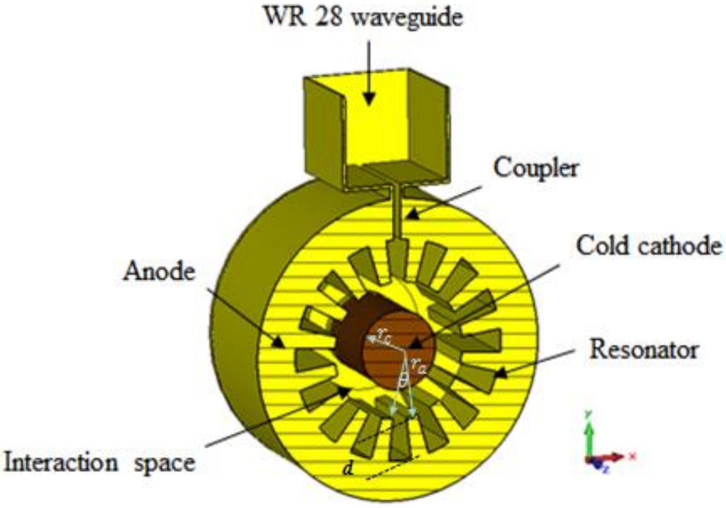

(b)

Figure 3.2 Simulation model of a 35 GHz π/2-1 mode SHM with auxiliary side cathode and platinum cold secondary emission main cathode (a) cross section plotted in the y-z plane; (b) cross section plotted in the x-y plane.

Table 3-1 Geometrical parameters of a 35GHz magnetron simulation model

Number of vanes N	16
Anode radius r_a, mm	2.25
Cathode radius r_c, mm	1.3
Side resonator depth d, mm	1.38
Aperture opening θ	12.5^{o}
Anode length h, mm	6
End space height, h_s, mm	1.2

3.2.2 Cold cavity simulation

3.2.2.1 Anode block

The cold cavity simulation by using CST eigen mode solver can reveal the resonance properties of the anode cavity, such as frequencies, mode patterns and Q values. There are two methods in the eigen mode solver: Advanced Krylov Subspace (AKS) and Jacobi-Davidson Method (JDM). The AKS solver calculates resonant modes in a predefined frequency interval, whereas in the JDM solver, there is no frequency limit but an increased solver time. The JDM solver is selected in this simulation.

The resonant frequencies of the anode cavity mainly depend on the geometry of the anode block. The anode block without end space and output structure is relatively simple and does not need a large number of mesh cells to obtain the cold cavity resonance properties. As shown in Figure 3.3, the anode block consists of 16 vanes, a cylinder cathode, and vacuum interaction space. To ensure the magnetic field along the axial direction and the electric field in the cross section are without any distortion, perfect magnetic conductor (PMC) boundaries are assumed at the top and bottom of the anode block.

To examine the effect of the mesh cell, the simulation is performed with two different mesh types. One is tetrahedral mesh with mesh number of 50043 (Figure 3.4 (a)); the other is hexahedral mesh with mesh number of 202500 (Figure 3.4 (b)). As shown in Table 3-2. The simulation results are close to each other. The slight frequency deviation is due to the different mesh types. Resonant modes can be identified from the profiles of the vector electric field. The phase differences between the neighbouring side resonators of $\pi/2$-1 mode (n=3), $\pi/2$ mode (n=4), and π mode (n=8) are 67.5^o, 90^o, and 180^o respectively. The distributions of electric field pattern and amplitude are presented in Figure 3.5.

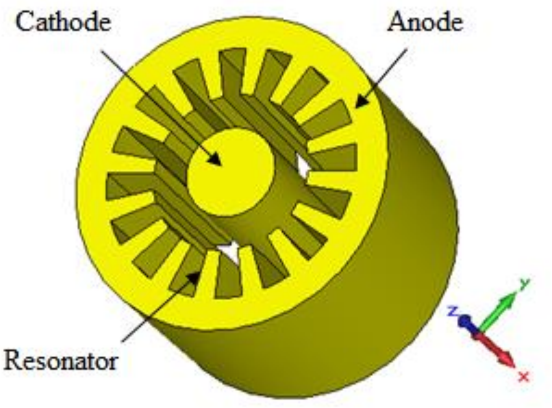

Figure 3.3 3-D structure of an anode block with PMC boundaries.

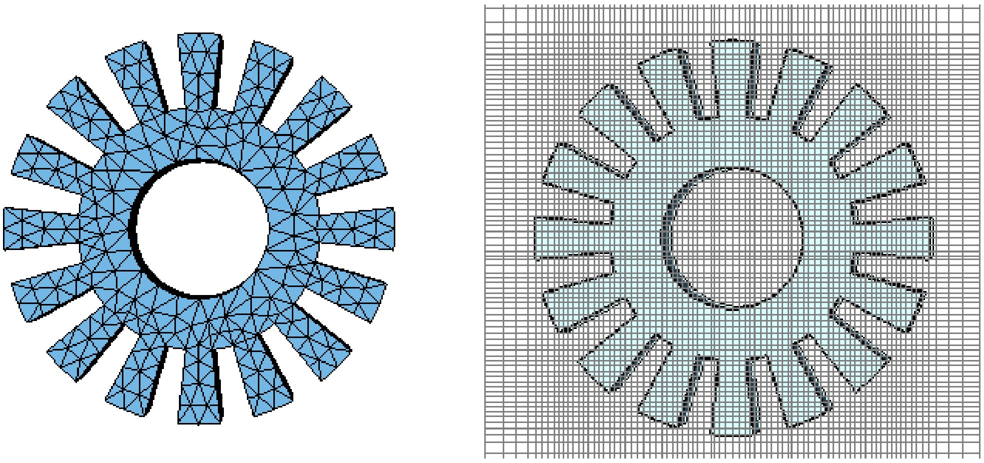

(a) **(b)**

Figure 3.4 Simulation models of anode block with two different mesh types: (a) 50043 tetrahedral mesh cells; (b) 202500 hexahedral mesh cells.

Table 3-2 Cold simulation results of anode block with Tetrahedral and Hexahedral mesh types

Mode number, n		1	2	**3**	4	5	6	7	8
Tetrahedral	f (GHz)	17	28.9	**34.99**	37.9	39.5	40.4	40.89	41.04
Hexahedral	f (GHz)	17.09	28.99	**34.92**	37.87	39.37	40.47	40.79	40.93

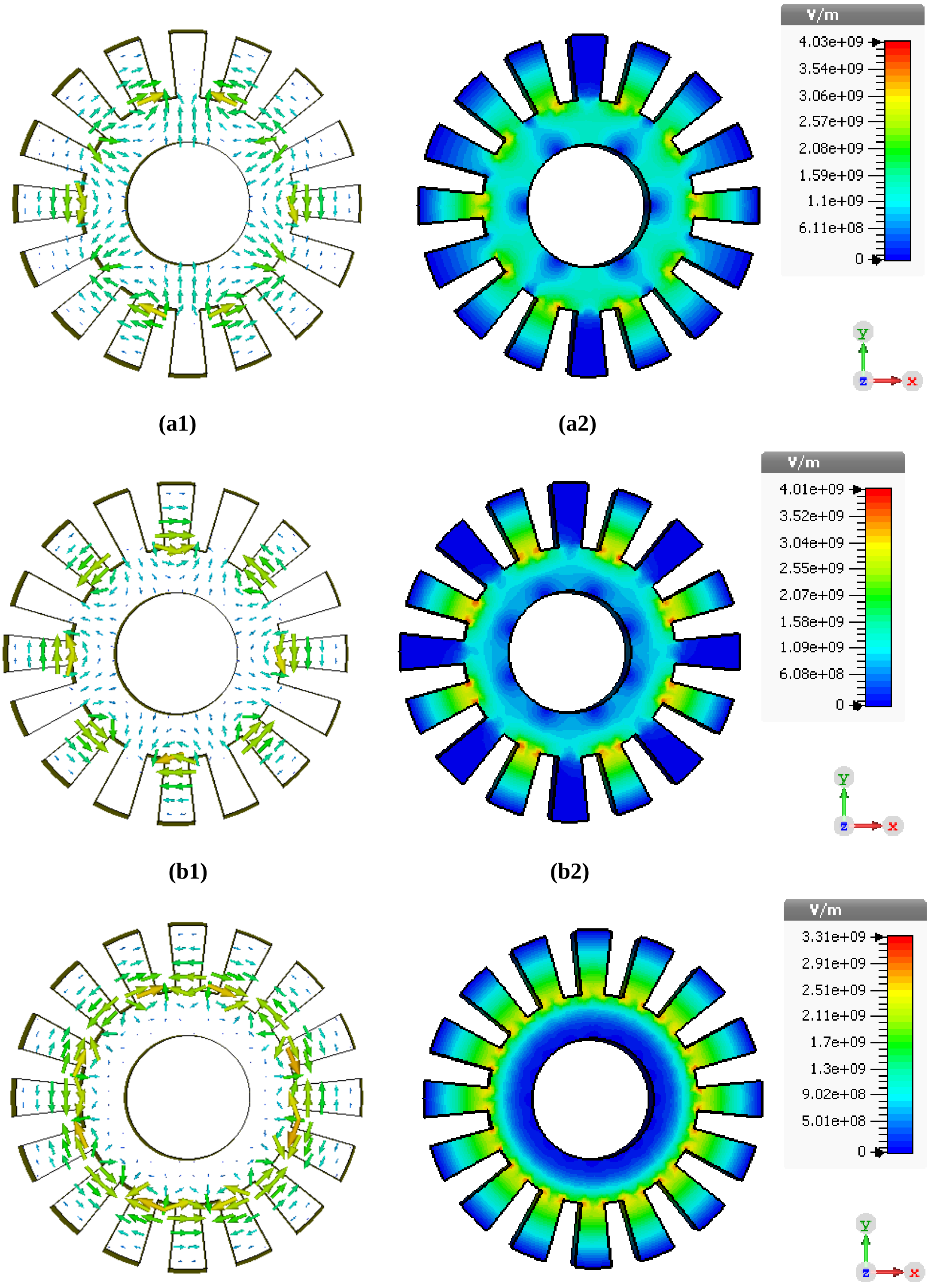

(a1) (a2)

(b1) (b2)

(c1) (c2)

Figure 3.5 Distributions of E-field vector and amplitude of π/2-1 mode (a1, a2), π/2 mode (b1,b2), and π mode (c1, c2) in the anode block.

The π/2-1 mode resonant frequency is found to be 34.99 GHz. For the n-th mode, the mode separation can be calculated by

$$\frac{f_{n+1} - f_n}{f_n} \qquad 3.\ 1$$

Considering the simulated frequencies in Table 3-2, the mode separation of π mode (n=8) is 0.36%, while the mode separation of π/2-1 mode (n=3) is 8.3% which is about 22 times higher. Thus, the π/2-1 mode SHM has naturally good mode separation even without any mode separation straps.

It can be observed that the E-field is concentrated in the area close to the anode and attenuated with the distance away from the anode. As shown in Figure 3.5(c), the e-field amplitude of π mode is uniformly distributed in the vicinity of the cathode. However, for the non-π mode such as π/2-1 mode and π/2 mode, the E-field distributions near the cathode are periodical and the periodic number is equal to the mode number *n* as shown in Figure 3.5 (a) and (b),

The effects of the geometrical parameters of the side resonators are examined by a series value of vane depth *d* and the opening angle θ. Figure 3.6 is simulated dispersion diagrams when the vane depth is varying from 1.3 mm to 1.46 mm with a constant 12.5° resonator opening angle. Figure 3.7 shows simulated dispersion diagrams when the opening angle is varying from 12.3° to 12.9° with a constant 1.38 mm vane depth. The comparison with these two diagrams indicates that the resonant frequencies depend on vane depth rather than the opening angle. The resonant frequencies increase with shorter vane depth.

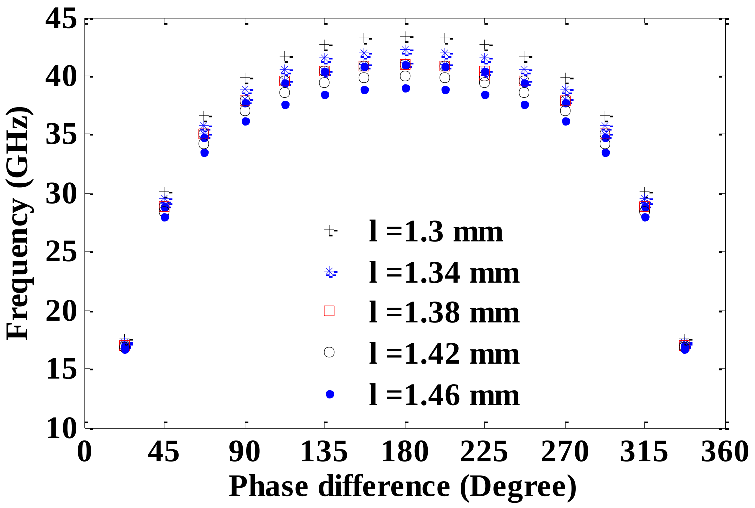

Figure 3.6 Dispersion diagrams when vane depths are varying from 1.3mm to 1.46 mm at 12.5o opening angle.

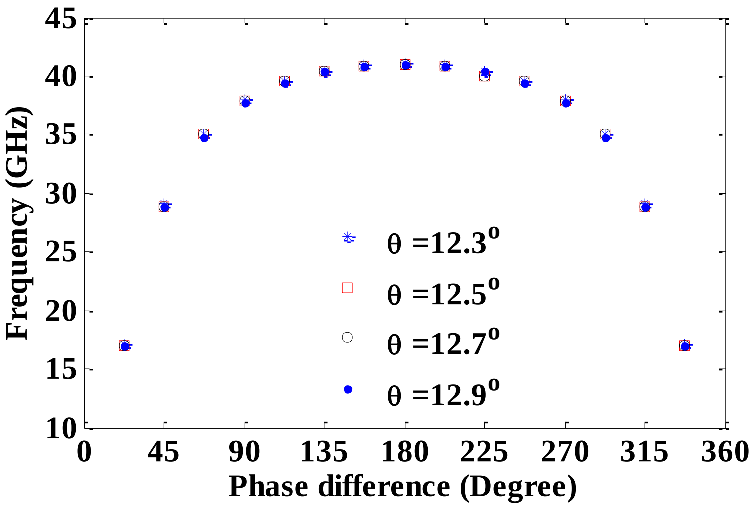

Figure 3.7 Dispersion diagrams when opening angles are varying from 12.3o to 12.9o at 1.38mm vane depth.

3.2.2.2 Anode cavity

Putting back the end space, coupler and the output waveguide, the resonance properties of the anode cavity are obtained according to cold cavity simulation. The E-field patterns of π/2-1 mode and π/2 mode of the anode cavity are shown in

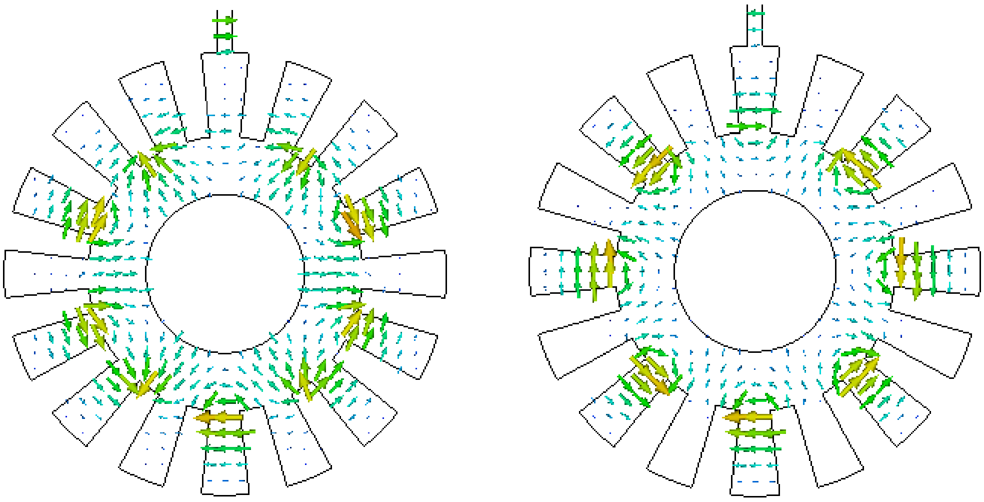

(a) (b)

Figure 3.8 E-field patterns of (a) π/2-1 mode (35.16 GHz) and (b) π/2 mode (37.9 GHz).

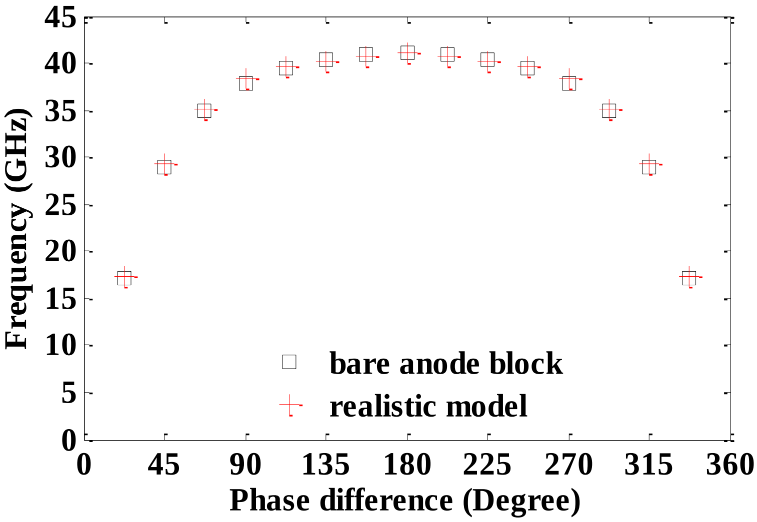

Figure 3.9 Dispersion diagrams of anode block and realistic anode cavity.

Figure 3.8 which is similar with the E-field patterns of the anode block presented in Figure 3.5. The π/2-1 mode of the anode cavity resonates at 35.16 GHz and has a loaded quality factor Q_L of 264. The loaded quality factor of π/2 mode is found to be 207 at 37.9 GHz. The dispersion diagrams of anode block and anode cavity are plotted in Figure 3.9. It shows that the resonant frequencies of the anode cavity are very close to those of the anode block. The slight difference is due to the effect of cathode hat, end space, side cathode, and coupler.

3.2.3 Particle-in-cell simulation

3.2.3.1 Electron dynamics

The electron-wave interaction is investigated by using the CST PIC solver. Figure 3.10 shows an annular electron source of the side cathode. The outer radius r_o of the emission area is 1.5 mm. The inner radius is 1.3mm which is the same as the radius of the cold cathode $\mathrm{r_c}$. The emission current is constant at 400 mA. The side cathode and the main cathode are connected to the same voltage source while the anode cavity is grounded. Figure 3.11 shows the anode voltage signal which increases monotonously from 0V to 12.8 kV within 10 ns rise time. The potential distribution when anode voltage rises to 4 kV is shown in Figure 3.12.

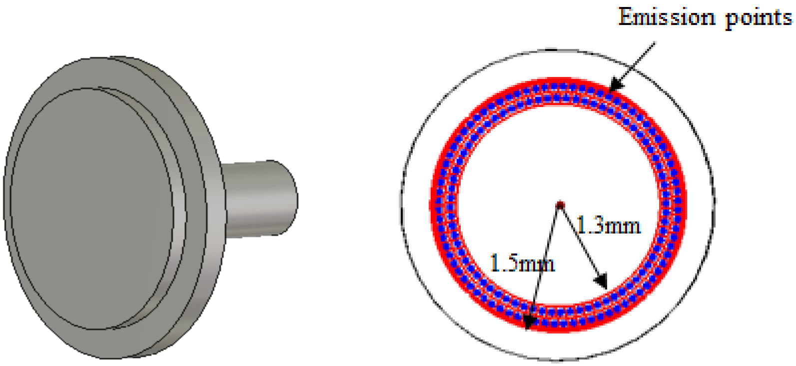

(a) (b)

Figure 3.10 Electron source on the side cathode with 400 mA DC emission current (a) side cathode; (b) annular emission area with1.3 mm inner radius and 2.1 mm outer radius.

As shown in Figure 3.13, the electrons emitted from the side cathode are injected into the interaction space during the leading edge of the anode voltage in the axial direction. As the uniform magnetic field (B=0.5875 T) is parallel to the electron trajectory and the anode voltage at this stage is small, the radial component of the electron velocity is negligible. These injected electrons accumulate near the surface of the cold cathode. The thickness of the electron sheath is equal to 0.2 mm ($r_O - r_c$).

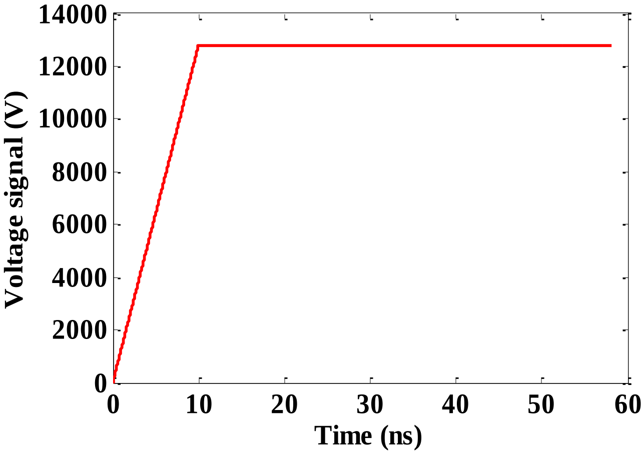

Figure 3.11 12.8kV anode voltage with 10ns rise time.

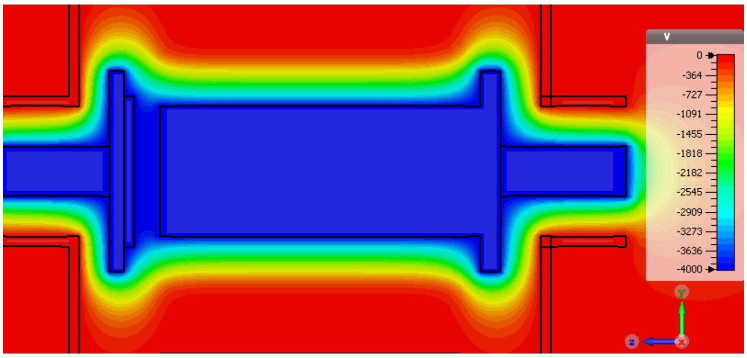

Figure 3.12 Static electric potential when anode voltage rises to 4kV.

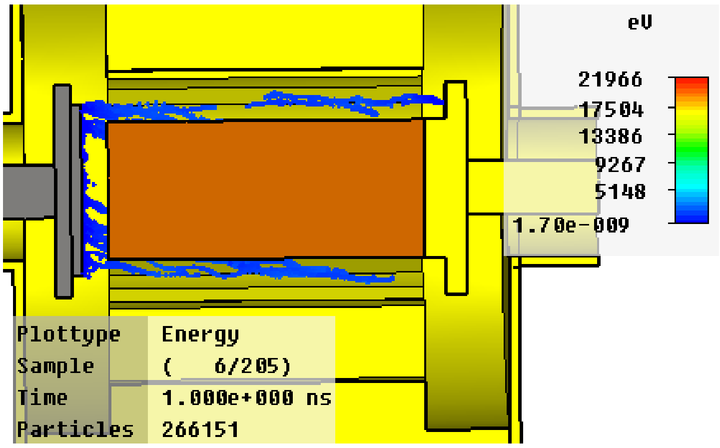

Plottype Energy
Sample (6/205)
Time 1.000e+000 ns
Particles 266151

Figure 3.13 Electron injection from the side cathode into the interaction space during the leading edge of the anode voltage.

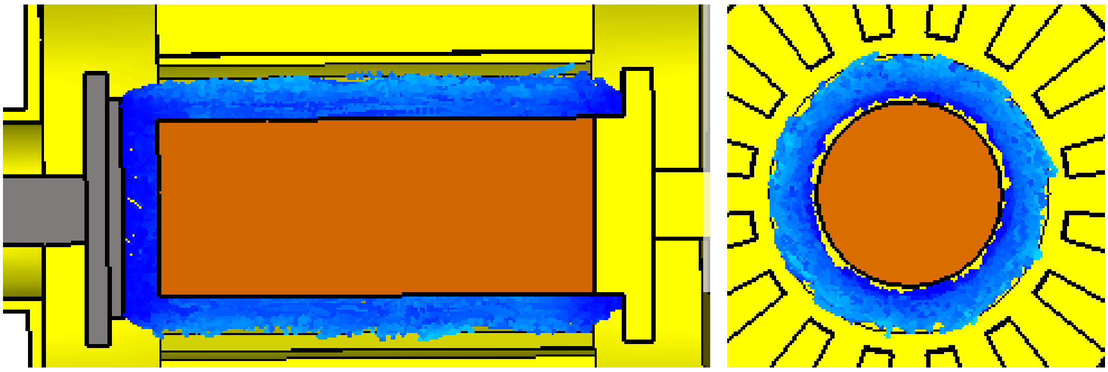

Figure 3.14 Electrons accumulated in the vicinity of the main cathode and expand toward the anode after 3 ns.

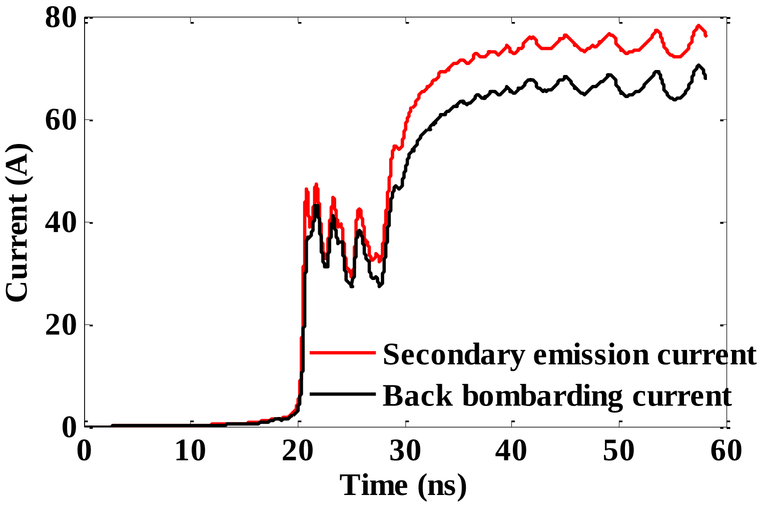

Figure 3.15 Secondary emission current and back bombarding current.

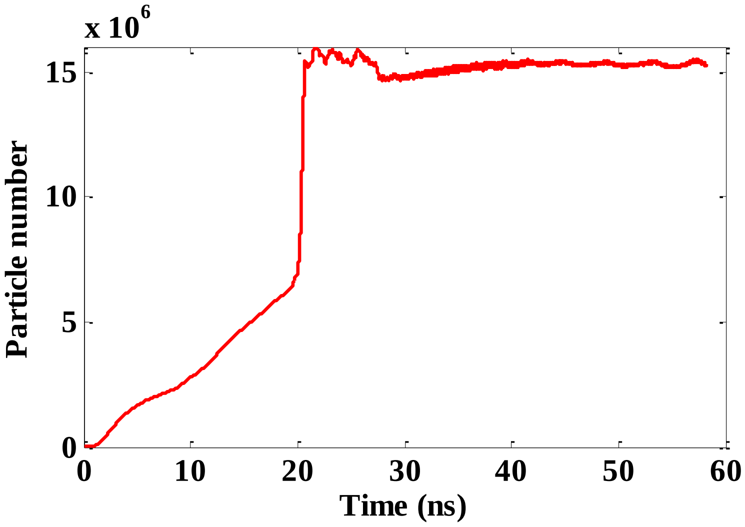

Figure 3.16 Time dependence of particle number in the interaction space.

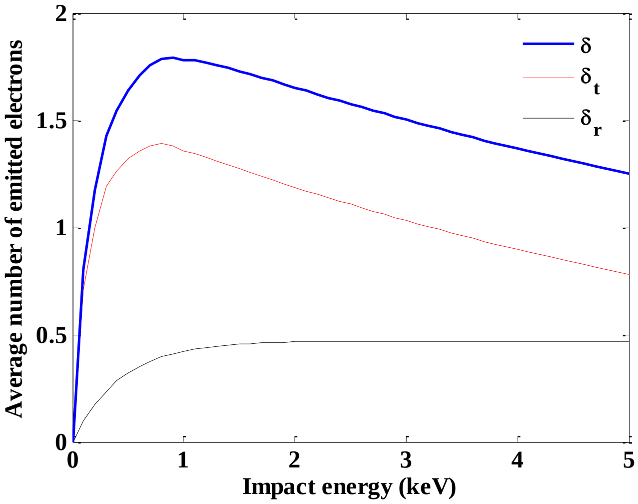

Figure 3.17 Platinum secondary emission coefficient versus impact energy for normal incidence angle. δ_t: true secondary emission coefficient; δ_r: inelastic reflection coefficient; δ: the total secondary emission coefficient.

As shown in Figure 3.14, with the anode voltage increasing, these accumulated electrons are rotating around the cold cathode and expanding toward the anode. The outer layer of the electron sheath interacts with the RF field. As shown in Figure 3.15 and Figure 3.16, at about 20 ns, the back bombarding electrons have sufficient energy to initialize the secondary emission coefficient higher than 1 and there is an avalanche process of the electron secondary emission. When the oscillation is stable, the average secondary emission current is 75 A. The back bombarding current is 62 A. The average secondary emission coefficient is 1.2 calculated by the ratio of the secondary emission current to the bombardment current (75A/62 A). Considering the cathode radius of 1.3 mm and cathode height of 6 mm, the area of the cold cathode surface is 0.48984 cm^2. The calculated secondary emission current density emitted from the cold cathode is 153.1 A/cm^2.

The calculated average back bombarding energy on the cold cathode is 430 eV. Representing the platinum secondary emission coefficient in Figure 3.17, one can see that the secondary emission coefficient is more sensitive to the impact energy in the region below 500eV than the region above 900eV. As the secondary emission is the main contributor to the cathode emission current, it could deduce that any conditions affect the stable of the secondary emission coefficient, such as the cold cathode contamination and surface roughness, may obviously affect the magnetron output power. The influence of the electron secondary emission coefficient will be investigated in the following sections.

As shown in Figure 3.18, when the oscillation is stable after 30 ns, there are 13 electron spokes along the anode surface. As is known, when the space charge effectively synchronizes with the operating mode, the number of spokes is equal to the complete period k of the RF wave around the anode circumference, where

$$k_{m,n} = |mN + n| \tag{3.2}$$

N is the number of the side resonators (N=16); m is the order of the spatial harmonic (m=-1 for the first order of the backward spatial harmonic); n is equal to 3 for the π/2-1 mode. So, k=13. Therefore, the formation of 13 electrons spokes indicates that the magnetron is operating on the π/2-1 mode of -1th spatial harmonic.

As is well known that, in classical magnetrons, the electron cloud consists of electron sheath embracing the cathode and electron spokes distribute periodically and regularly along the anode as shown in Figure 3.19 (X band classical magnetron E2V MG5240). However, as shown in Figure 3.18, the space charge distribution in this SHM is obviously different.

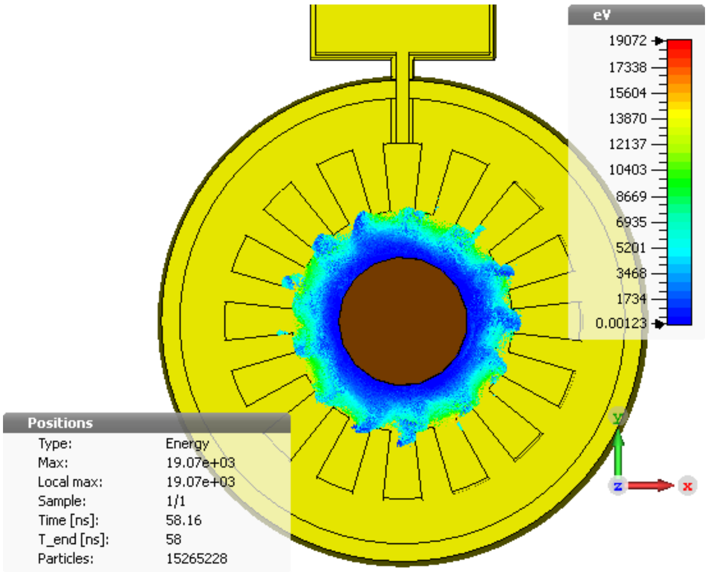

Positions
Type: Energy
Max: 19.07e+03
Local max: 19.07e+03
Sample: 1/1
Time [ns]: 58.16
T_end [ns]: 58
Particles: 15265228

Figure 3.18 Space charge distribution at the steady state of the oscillation (13 electron spokes; V_{dc}=12.8 kV; B=0.5875 T, 400 mA side cathode current).

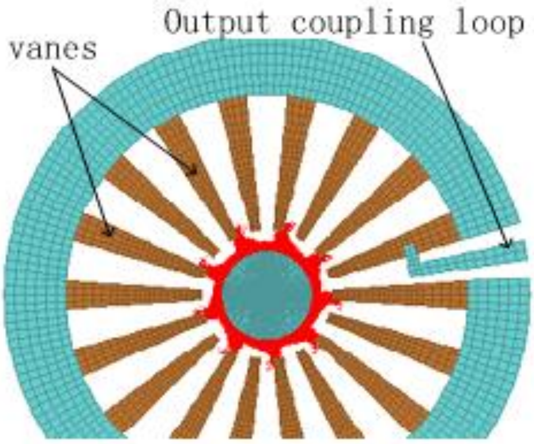

Figure 3.19 Periodical space charge distribution in a 18-vane classical magnetron (E2V MG5241) [42].

3.2.3.2 Comparison between the simulation results and the experimental data

In order to verify the simulation, it is necessary to compare the simulation results with the experimental data. Figure 3.20 depicts the simulated amplitude of the output voltage V_{out} monitored at the centre line across broad walls of WR28 output waveguide. The output voltage reaches a saturation value V_{out}= 3570 V at the steady state of the oscillation.

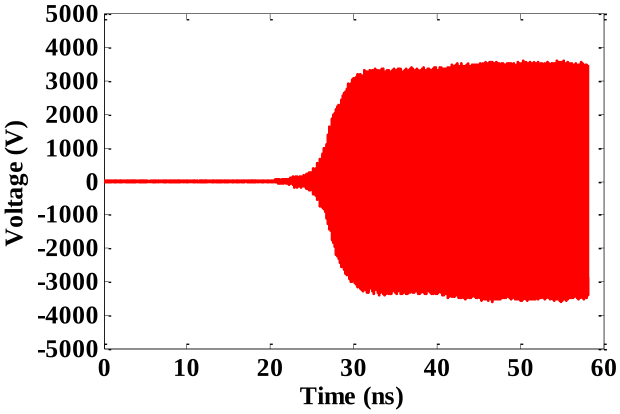

Figure 3.20 Simulated output voltage monitored at the central line of the output port.

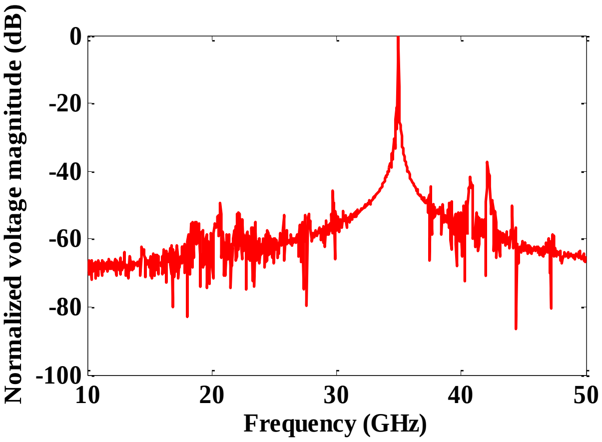

Figure 3.21 Output frequency obtained by Fourier Transform of the output voltage.

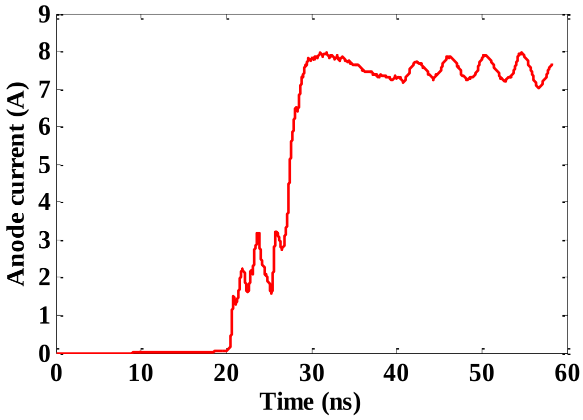

Figure 3.22 The time evolution of anode current.

Figure 3.21 plots the oscillation frequency spectrum with normalized amplitude, which is obtained from a Fourier transform of the time-varying voltage. The oscillation frequency f is 34.96 GHz, which is close to the cold cavity frequency of 35.16 GHz of the π/2-1 mode. It is reasonable for the frequency shift between the cold cavity and the hot cavity due to the effect of the space charge.

The saturated output power is calculated using [63]

$$P_{out} = \frac{a}{4bZ_0} V_{Out}^2 \sqrt{1 - (\frac{f_c}{f})^2} \tag{3.3}$$

a: width of WR28 waveguide. a=7.11 mm.

b: height of WR28 waveguide. b=3.55 mm.

Z_0: wave impedance. Z_0 =377 ohm.

f_c: cut off frequency of the WR28waveguide. f_c =21.08 GHz.

f: oscillation frequency, f=34.96 GHz.

The calculated saturated output power is equal to 13.5 kW.

Figure 3.22 shows the time evolution of anode current I_a. In CST Particle Studio, this current is calculated by the average charge hitting the anode surface during each time step. There is no anode current before 10 ns during the electron injection period. A small amount of anode current appears during 10 ns – 20 ns when the interaction space is filled with space charge. The value of the anode current increases during the starting up of the oscillation and reaches to around 7.5 A at the steady state.

The simulated power conversion efficiency η is 14.2%, calculated by

$$\eta = \frac{P_{out}}{U_a I_a} \tag{3.4}$$

The simulation results, including frequency f, output power P_{out}, anode current I_a, efficiency η, together with the experiment data are summarized in Table 3-3, where one can find a good agreement between them. Therefore, this SHM model is verified by experiment.

Table 3-3 Simulation results and experiment results

	f GHz	P_{out} kW	I_a A	η %	U kV	B T
Simulation	34.96	13.5	7.5	14.2	12.8	0.5875
Experiment[55]	35	15.23	7.5	15.5	12.8	0.5875

3.2.3.3 Distribution of the Electron Back Bombarding Energy and Secondary Emission Current

In order to investigate distribution of the electron back bombarding energy and secondary emission current on the cold cathode, the cold cathode is divided into 6 units equally as shown in Figure 3.23. Figure 3.24 plots the simulation results of distribution of the back bombarding energy, which shows that the back bombarding energy follows an approximately Gaussian distribution along the cathode length. The impact energy on the central parts of the cold cathode is around 500eV, which is higher than that on the ends of the cathode. Unite “1” and Unite “6” at the ends of the cathode suffer nearly the same back bombarding energy around 350eV. Figure 3.25 presents the time evolution of secondary emission current of each unite. It shows that the secondary emission current of Unite “1 (12A) is much higher than that of Unite “6” (9A). As is known, the secondary emission coefficient depends not only on the impact energy, but also on the incident angle of the back bombarding electron. With the same incident energy, the secondary emission coefficient increases with incident angle [66]. Therefore it can be deduced that the primary electrons on Unite “1” which is near the

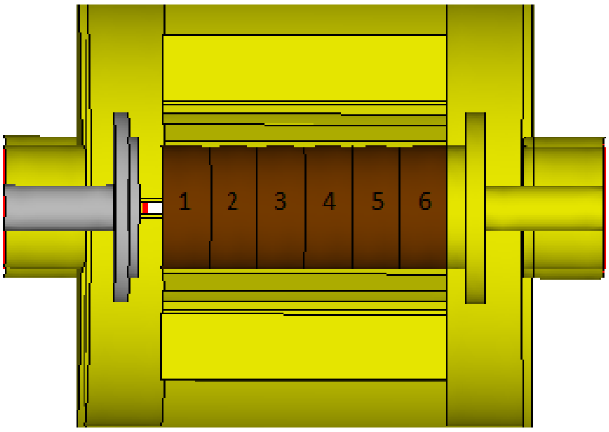

Figure 3.23 The length of the cathode is divided into 6 units.

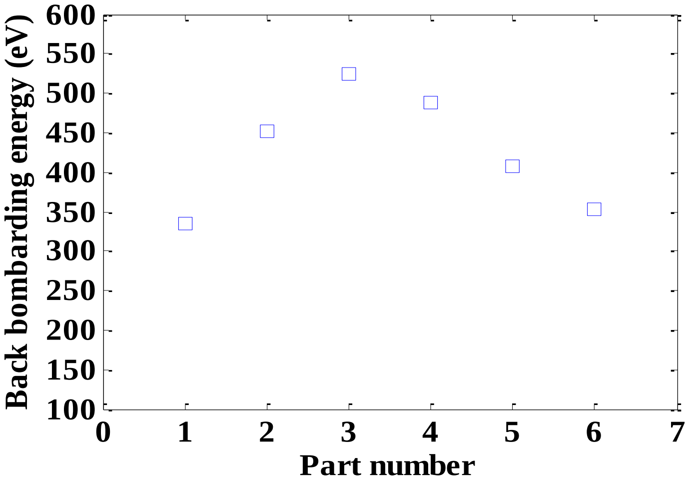

Figure 3.24 Distribution of bark bombarding energy along the cathode.

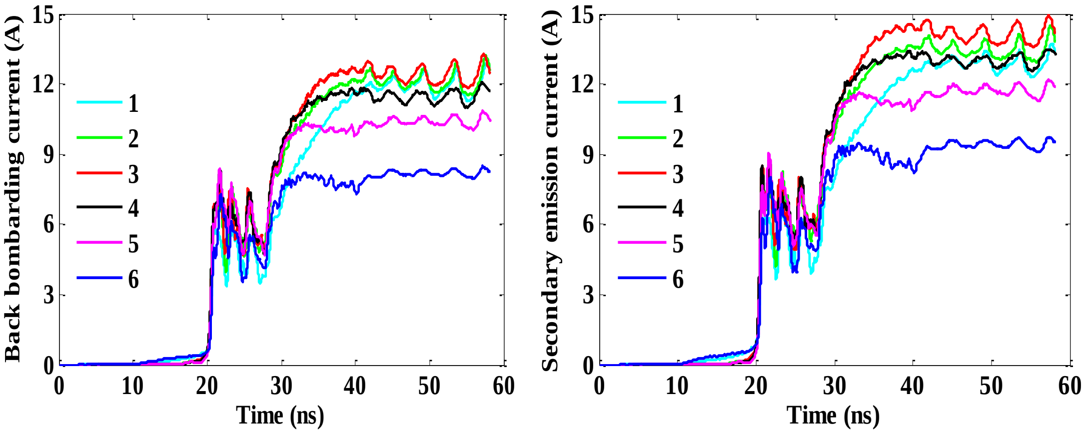

(a) (b)

Figure 3.25 Time evolution of the distributed back bombarding current (a) and secondary emission current (b) along the cold cathode.

side cathode has larger incident angle due to the effect of the side cathode and the static electronic field. Unite “6” which is far from the side cathode has smaller incident angel.

3.2.3.4 Transient behaviour - mode competition

The transient behaviour of oscillation can be investigated through the observation of frequency spectrum inside the anode cavity. Figure 3.26 shows the frequency spectrum monitored at the aperture of side resonators at different moments 8ns, 10ns, 15ns, 20ns, 22ns, 23ns, 25ns, and 40ns, respectively.

As shown in Figure 3.26 (a) and (b), when electrons are injecting into the interaction space before 10 ns, there is no any oscillation. During this stage, there is no anode current, no back bombarding current, no secondary emission current. As shown in Figure 3.26(c) and (d), when electrons are accumulating near the cathode during 10 ns – 20 ns, 40.96 GHz is the dominant frequency. Referring to the cold cavity frequencies, π-mode is the dominant mode. The main reason is that π-mode has the largest amplitude than other modes. 29.76 GHz and 47.03 GHz do not belong to any oscillation modes.

As shown in Figure 3.26(e)-(g), when the oscillation starts up during 20 ns – 30 ns, there is a strong mode competition. In the beginning, π/2+1 mode (n=5) with a resonant frequency of around 39.16 GHz is the dominant mode which competes with the π/2-1 mode (35.02 GHz). With time elapsing, the amplitude of the π/2-1 mode grows up when the electron speed is close to its phase velocity. During this period, the neighbouring π/2 mode (37.52 GHz) competes with the operating π/2-1 mode, since their phase velocities are close to each other.

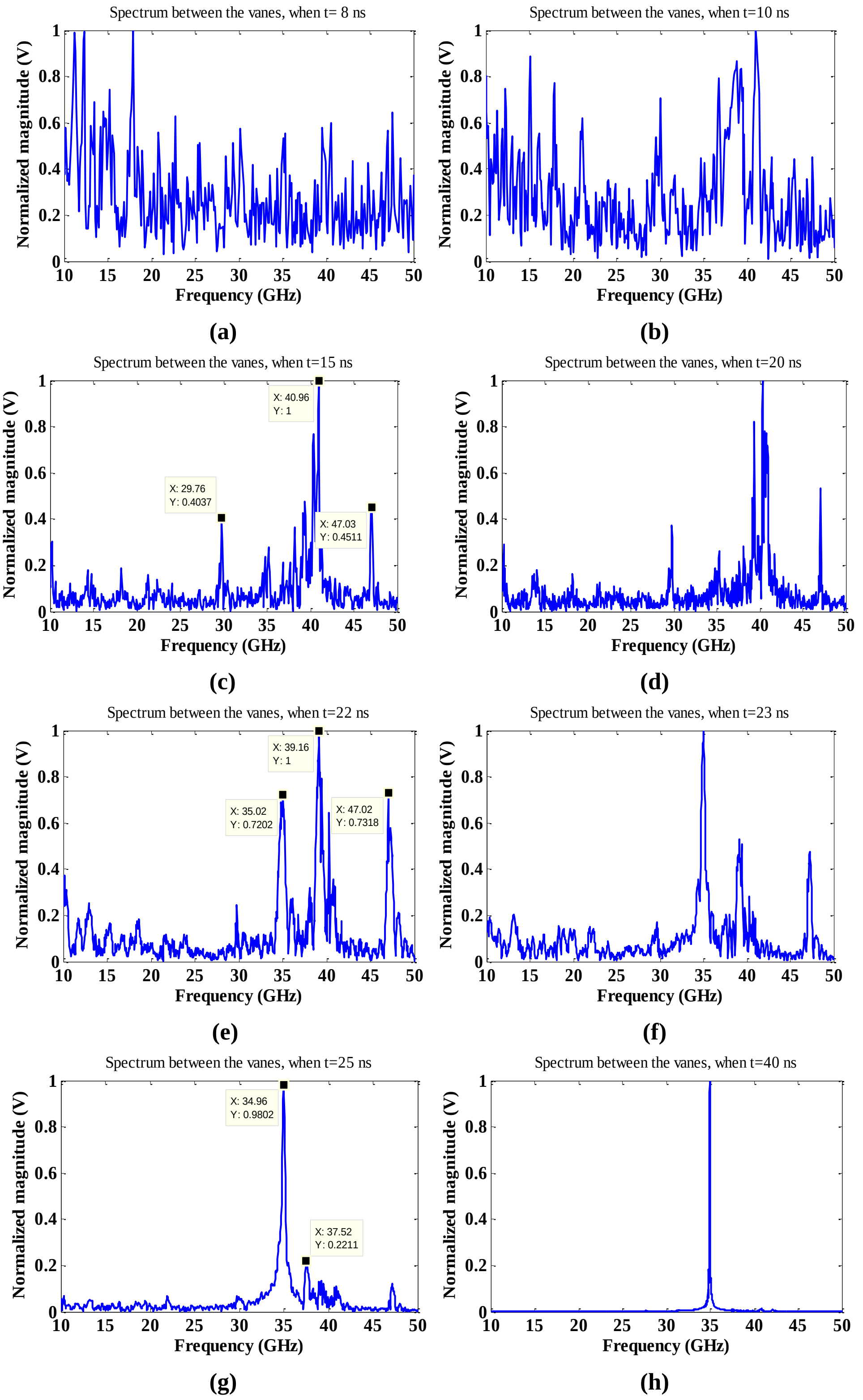
Spectrum between the vanes, when t= 8 ns

Spectrum between the vanes, when t=10 ns

Spectrum between the vanes, when t=15 ns

Spectrum between the vanes, when t=20 ns

Spectrum between the vanes, when t=22 ns

Spectrum between the vanes, when t=23 ns

Spectrum between the vanes, when t=25 ns

Spectrum between the vanes, when t=40 ns

(a) (b)

(c) (d)

(e) (f)

(g) (h)

Figure 3.26 Spectrum of the voltage monitored at the aperture of one of the vanes at (a)8ns; (b)10ns; (c)15ns; (d)20ns; (e)22ns; (f)23ns; (g)25ns; (h)40ns.

As shown in Figure 3.26 (h), when the oscillation is stable after 30 ns, the oscillation is stable on the π/2-1 mode at 34.96 GHz. The output power, anode current, and the secondary emission current are nearly constant.

According to the investigation of the transient behaviour, one can see that π mode, π/2+1 mode, and π/2 mode are competitors to the operating π/2-1 mode at different moments. The oscillation of the SHM requires a relatively long electron residence time to start, which is different from classical magnetrons.

3.2.4 Higher injection current

The emission current from the thermionic side cathode is temperature dependant. The typical injection current is several hundred milliamps at around 1250K (a typical temperature for the magnetron operation) [43]. In this section, the simulation is performed with 10A injection current which exceeds the necessary value by several orders of magnitude. Although it is too high for practical operation of the magnetron, it is useful to investigate the effect of the injection current to the magnetron operation.

The simulated output voltage profile and oscillation spectrum are presented in Figure 3.27. Compared with the model with 400 mA side current as studied in the last section, the time of pre-oscillation reduces from 30ns to 10ns. The main reason may be that the higher injection current reduces the time that the electrons require to accumulate near the cathode. The output power increases from 13.5kW to 17.2 kW but with more fluctuations. Table 3-4 is the comparison between the simulation results of the models with 400mA and 10A injection currents and the experimental data. It indicates that the value of injection current I_p does not affect the magnetron output performance significantly. The injection current is just to trigger the secondary emission of the cold cathode.

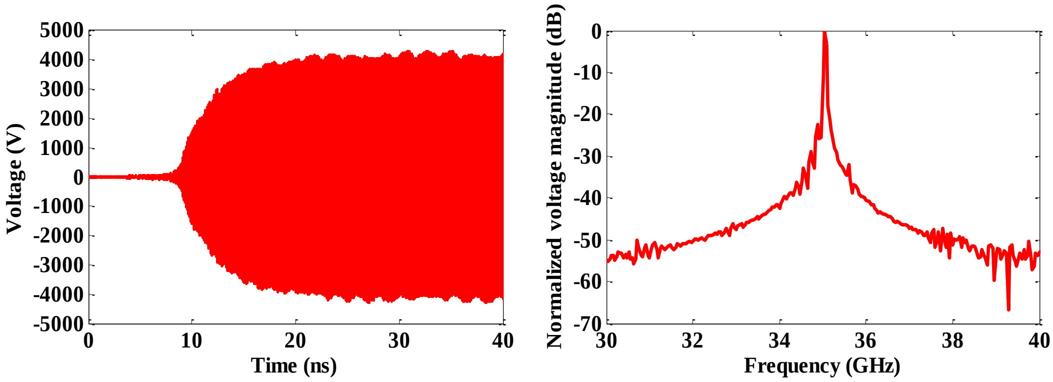

(a) (b)

Figure 3.27 Simulation results with 10 A injection current (a) profile of the output voltage; (b) oscillation spectrum.

Table 3-4 Comparison between the simulation results and experimental results

	I_p (A)	f (GHz)	P_{out} (kW)	I_a (A)	I_s (A)	I_b (A)
Simulation results	0.4	34.96	13.5	7.4	73	65
	10	35.04	17.2	10	76	69
Experiment results	0.1-0.4	35	15.23	7.5	--	--

3.3 Development of a Simplified Model without Side Cathode to Speed up the Simulation

3.3.1 Introduction to the simulation model

Compared with conventional magnetron, particle simulation of the SHM is very time consuming due to the electron injection and electron secondary emission. One simulation for a simulation time of 58ns of the previous model takes about 220 hours with computer equipped with quad-core Intel 3.3-GHz processor, which hinders our research on the SHM. Therefore, it needs to develop an approach to speed up the simulation while capturing the main features of SHM. The study in the last section shows that the performance of SHM mainly depends on the electron multiplication rather than the injection current. This may open a way to develop a simplified model without side cathode to speed up the particle simulation.

The simplified model without side cathode is shown in Figure 3.28. The geometrical dimensions of anode cavity and cathode are the same as the model in Figure 3.2. Hence, as presented in Table 3-5, the simulation results of the cold cavity including resonant frequencies and Q factors are close to the realistic one. The slight difference is due to the effect of the side cathode and the end space.

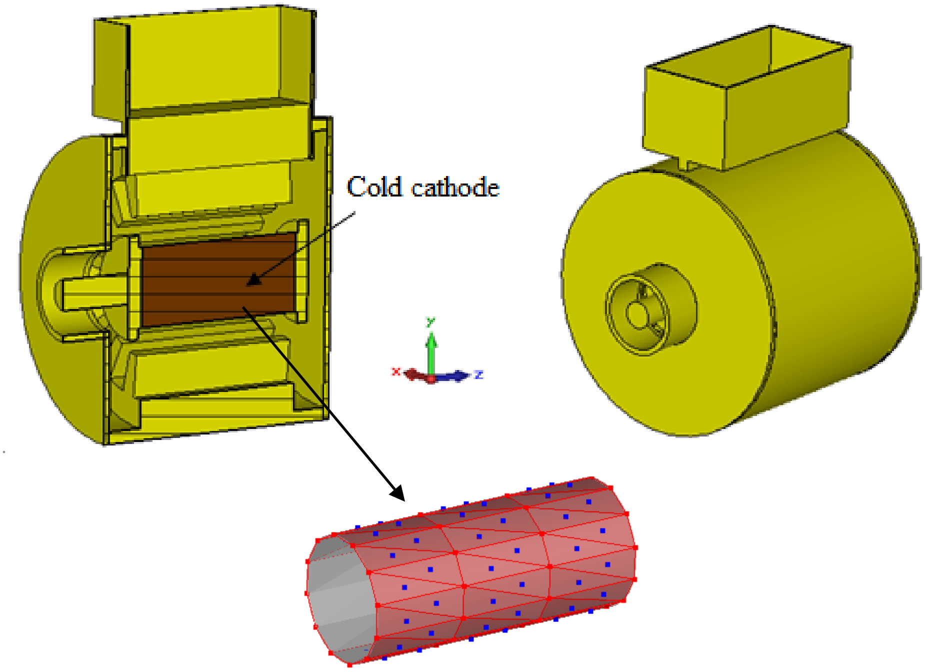

Figure 3.28 Simplified SHM model without side cathode.

As shown in Figure 3.28, to trigger the electron secondary emission, a small amount of seed current is specified on the surface of cold cathode. The emission points are located at the centre of the mesh cells. A uniform magnetic field is in the axial direction along the cathode. When the anode voltage is applied through the discrete port of the filament, primary electrons are emitted from these emission points. These electrons rotating around the cathode under the crossed field form an electron sheath near the cathode surface. With the rising of the anode voltage, the electron sheath expands towards the anode and the outer layer of the electron sheath interacts with the cavity RF field. The secondary emission will be triggered under the intense back bombardment energy. Therefore, a large value of secondary emission current is triggered by a small value of the seed current.

Table 3-5 Cold simulation results of the simplified model without side cathode

n	1	2	**3**	4	5	6	7	8
f (GHz)	21.47	30.11	35.35	37.9	39.6	40.2	40.95	41.18
Q_{ext}	--	393.8	407.8	388	--	--	--	--
Q_o	--	1775	1757	1736	--	--	--	--
Q_L	--	322	330	317	--	--	--	--

3.3.2 Verification of the simplified model

3.3.2.1 Electron dynamics

In this simplified model, 5A DC emission current is specified on the cathode surface with 78 emission points. The applied anode voltage V_{dc} is 12.8 kV and the magnetic field B is 0.5875 T, which are the same as the realistic model. But to speed up the pre-oscillation, the rise time of the anode voltage is 1ns instead of 10ns.

The electron dynamic can be observed by the space charge distribution at different moments. Figure 3.29 presents the time evolution of space charge in the interaction space plotted in a half of x-z plane. In the beginning, the electron sheath initially forms in the areas near the emission points assumed on the cathode. In the regions, i.e., the areas between the centres of the mesh cells, there is no space charge. As time elapses, the space charge expands until it fills the whole interaction space. The number of particles increases and the distribution of space charge becomes uniform in the interaction space (see Figure 3.29 c).

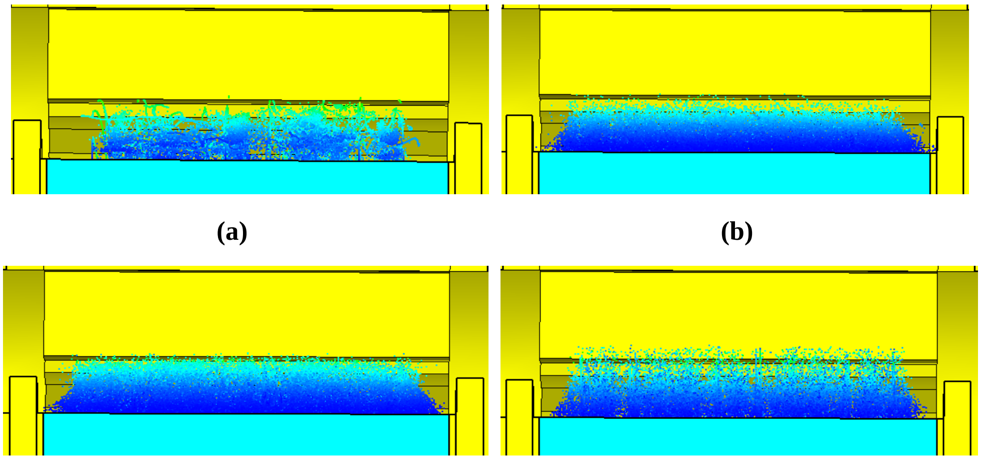

(a) **(b)**

(c) **(d)**

Figure 3. 29 Time evolution of the space charge in the interaction space plotted in a half of x-z plane at (a) 0.2 ns, (b) 3.2 ns, (c) 10 ns, and (d) 25 ns. The charge profiles are plotted for V_{dc}=12.8 kV, B=0.5875 T, and 5A seed current.

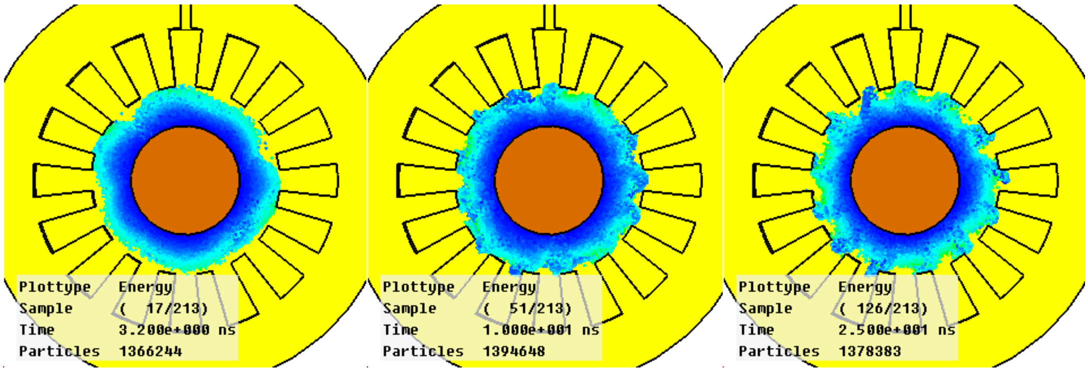

(a) **(b)** **(c)**

Figure 3.30 Time-evolved spoke formation plotted in the x-y plane at (a) 3.2ns, (b) 10 ns, and (c) 25 ns. The charge profiles are plotted for V_{dc}= 12.8 kV, B = 0.5875 T, and 5A seed current.

Figure 3.30 shows cut away views of the space-charge distribution in the x-y plane at 3.2ns, 10ns, and 25ns. After 13ns, the existence of 13 electron bunches is clearly distinguishable (see Figure 3.30 c) which is the same as that in the realistic model (see Figure 3.18), which indicates that the model is operating on the $\pi/2$-1 mode (n = 3) of the -1th spatial harmonic. Thus, it is verified that this simplified model could reflect the main process of electron dynamic of the SHM except the electron injection.

3.3.2.2 Comparison with the experimental data

The profile of the output voltage signal and the oscillation spectrum are presented in Figure 3.31. Compared with Figure 3.20, the pre-oscillation time reduces from 30ns to 10ns. The amplitude of the output voltage is 3786 V and the corresponding output power is 15.17 kW which is close to the experimental result of 15.23 kW. The simulated frequency as shown in Figure 3.31 (b) is 35.1 GHz.

In fact, the cathode current in this model consists of two parts in this simplified model. One is the 5A seed current. The other is 73A secondary emission current as shown in Figure 3.32. The seed current is around 6% of the total current. Therefore, the secondary emission current is the main contributor to the cathode current. The simulation results show a good agreement with the experimental data as shown in Table 3-6. Thus, this simplified model has been proved to provide a relative accurate predication of the SHM performance.

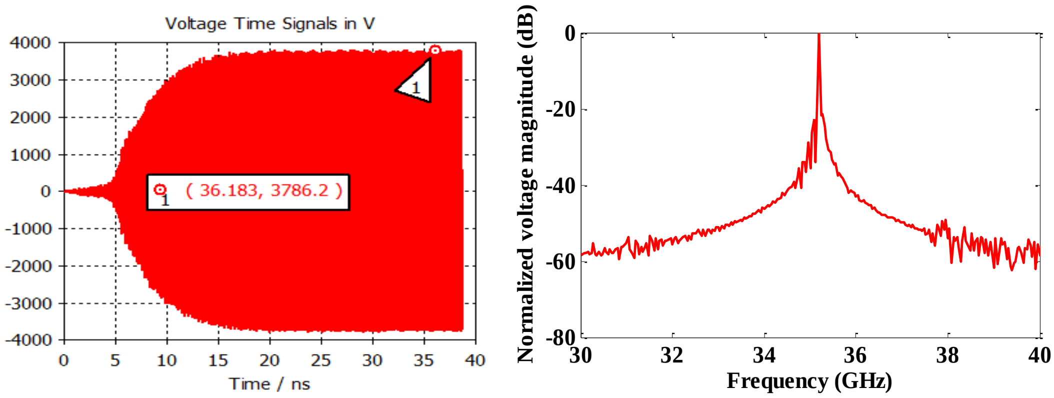

(a) **(b)**

Figure 3.31 (a) Simulated output voltage monitored at the central line of the output waveguide and (b) spectrum, when the anode voltage rising time is 1 ns, V_{dc}= 12.8 kV, B = 0.5875 T.

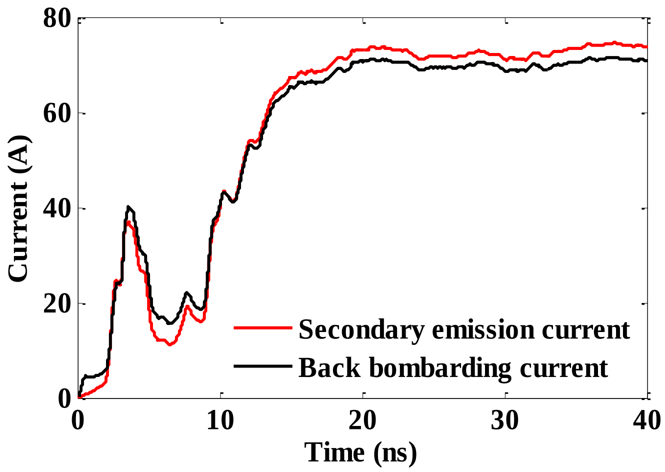

Figure 3.32 Secondary emission current and back bombarding current.

Table 3-6 Simulation results and experimental data (I_p: seed current; I_a: anode current; I_s: secondary emission current)

	I_p A	f GHz	P_{out} kW	I_a A	I_s A	η
Simulation results	5A	35.15	15.17	7.43	73	15.95%
	10A	35.15	16.2	7.78	80	16.2%
Experimental data	-	35	15.23	7.5	-	

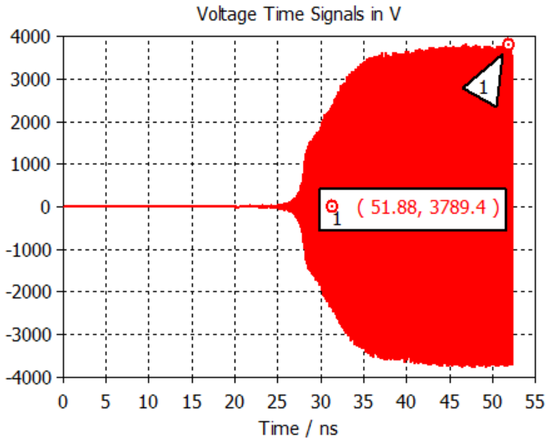

Figure 3.33 Simulated output voltage monitored at the central line of the output waveguide when the rising time of the anode voltage is 10 ns and the seed current is 5A.

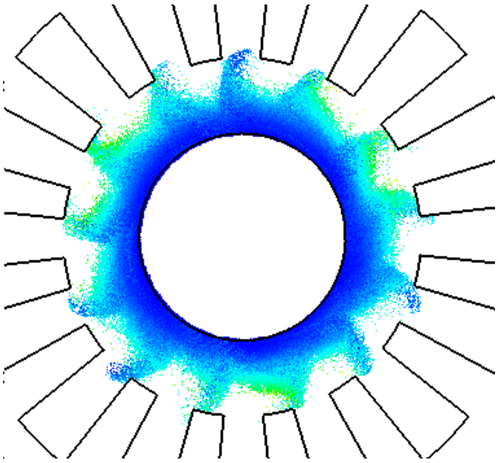

Figure 3.34 Distribution of Electron spokes when primary current is 10 A.

To examine the effect of the voltage rise time, simulations are carried out with 10 ns anode rise time of the anode voltage with 5A seed current. Comparing Figure 3.33 with Figure 3.31 (a), it confirms that the anode voltage rise time does not affect simulation results in this simplified model. The only difference is that the oscillation starts much slowly due to the slow leading edge of voltage.

To examine the effect of the seed current, the model is simulated with 10A seed current. As seen in Table 3-6, the output power, anode current and efficiency are slightly higher. The percentage of the seed current to the total cathode emission current increases from 6.4% to 11%. There are 13 electron spokes at the steady state of oscillation as shown in Figure 3.34 which is the same as Figure 3.30(c), but appears more regularly.

3.3.2.3 Transient behaviour - mode competition

The time involved frequency spectrum of the voltage at the aperture of the side resonator is presented in Figure 3.35. Since the secondary emission current and the space charge density is so weak before 2 ns that it is hard to see the dominant oscillation modes in Figure 3.35(a). The dominant frequency 40.95GHz in Figure 3.35 (b) is the same as that in the realistic model in Figure 3.26 (c). During the pre-oscillation, the

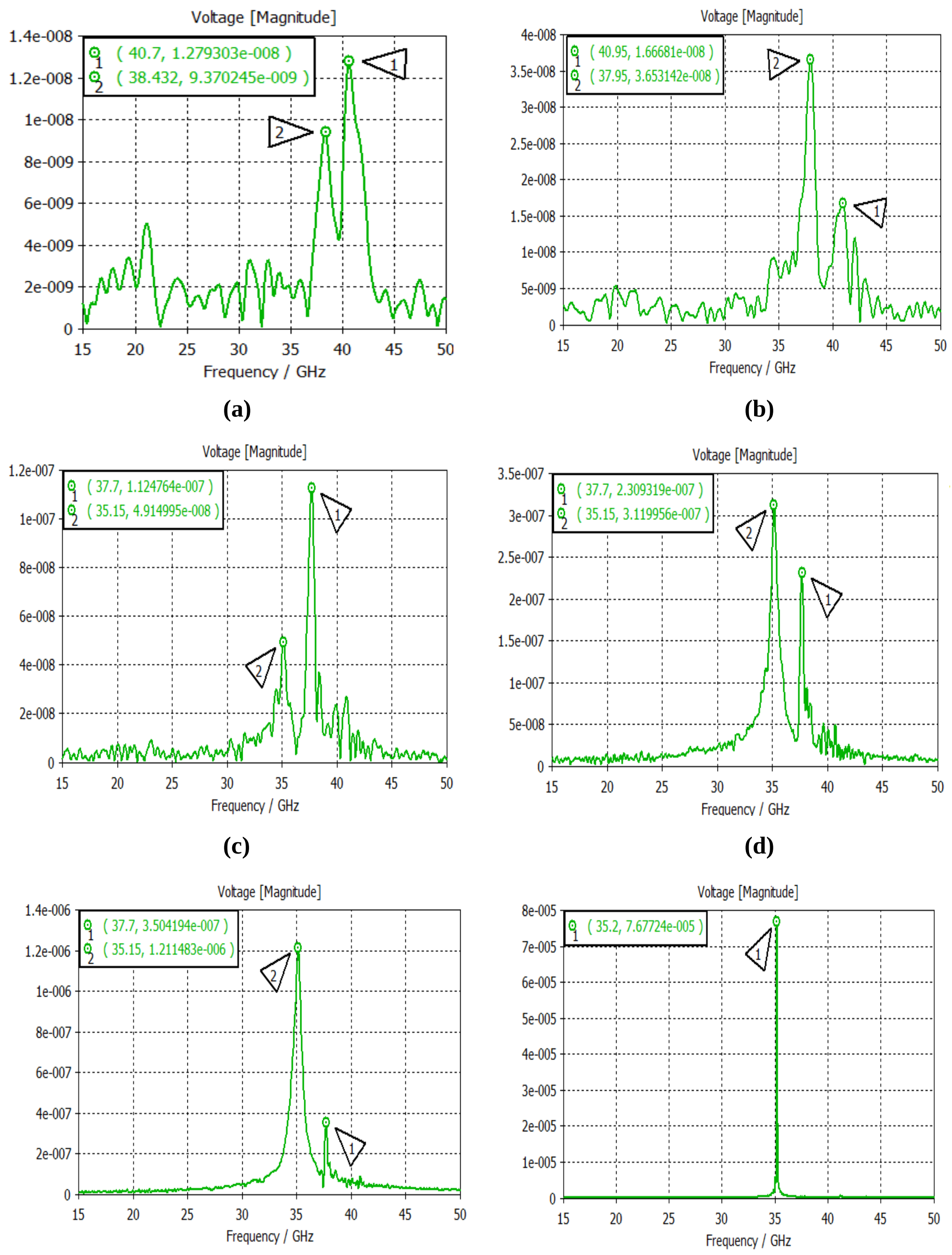

(a) **(b)**

(c) **(d)**

(e) **(f)**

Figure 3.35 Spectrum of the simplified model with 5 A seed current at different moments: (a) 1ns (b) 2ns (c) 4ns (d) 5ns (e) 6ns and (f) 10ns.

mode competition between π/2 mode (37.7GHz) and the π/2-1 mode (35.15GHz) can be clearly observed in Figure 3.35 (c)-(e). Finally the oscillation settles down in the π/2-1 mode at 35.15GHz in 3.35 (f). This mode competition process is similar to that in the realistic model in Figure 3.26.

The simulation results in section 3.3.2 show that the operating parameters of this simplified model including output power, anode current, space charge distribution, steady state and transient behaviour are all close to those in the realistic model and the experimental data. Therefore, it is verified that this simplified model is accurate enough in the investigation of the SHM. Compared with the realistic model, the simplified model reduces the simulation time from 200 hours to 40 hours on the same computer.

3.4 Investigation of the Secondary Emission Coefficient

Practically, the cold cathode is made of a copper core plated with platinum foil to reduce the cost. However, it causes the fabrication of the cold cathode more complicated. There is a practical need for cheaper materials to simplify the cathode fabrication. Therefore, the dependence of magnetron characteristics on secondary emission coefficient is investigated. The investigation is based on the simplified model with a cold cathode having various secondary emission coefficients: 0.6*δ, 0.8*δ, 1.2*δ, 1.4*δ, where δ is the secondary emission coefficient of platinum. The operation is set at V_{dc}=12.8 kV and B=0.5875 T. Figure 3.36 shows that the smaller secondary emission coefficient results in more irregular space charge accompanied with noisy spectrum. As shown in Figure 3.36, the secondary emission current dramatically increases with the secondary emission coefficient. When the secondary emission coefficient increases to 1.4*δ, the secondary emission current is as high as 220 A. Figure 3.36 indicates that the threshold value of the electron secondary emission coefficient for the magnetron operation is about 0.8*δ, below which the oscillation is not stable or even fails to start. The output power and efficiency increase with the secondary emission coefficient and drops down obviously when the secondary emission coefficient is 1.4δ.

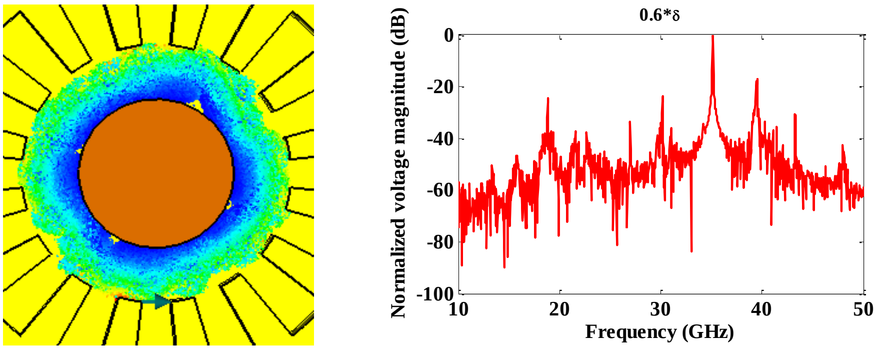

(a) 0.6*δ

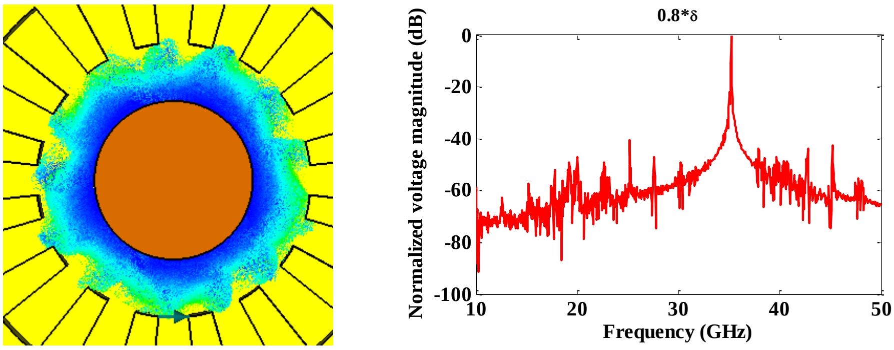

(b) 0.8*δ

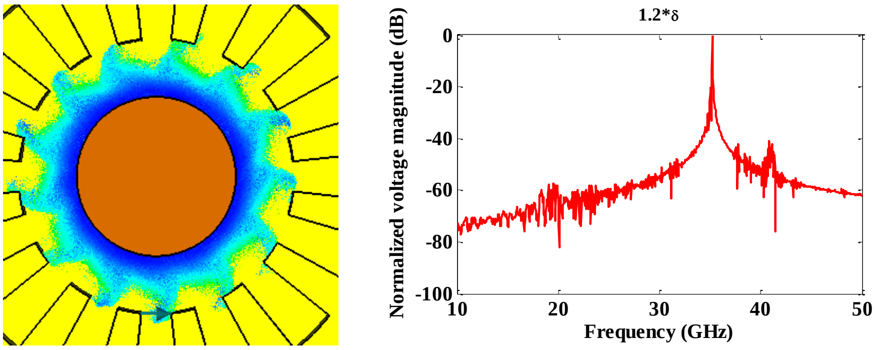

(c) 1.2*δ

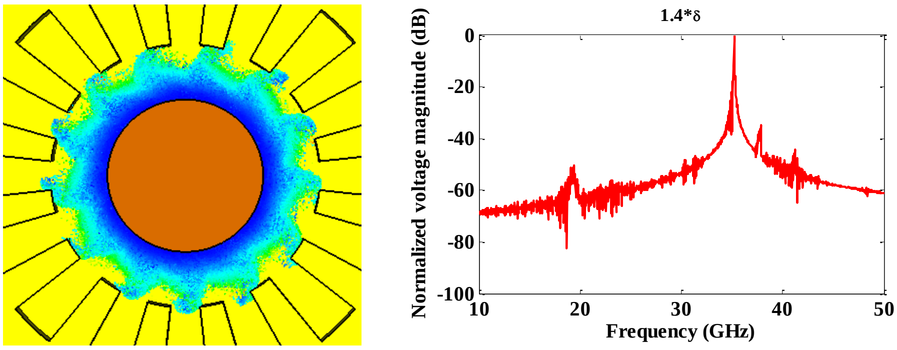

(d) 1.4*δ

Figure 3.36 Space charge distribution and output spectrum after 20ns, when secondary emission coefficient are 0.6*δ, 0.8*δ, 1.2*δ, 1.4*δ respectively.

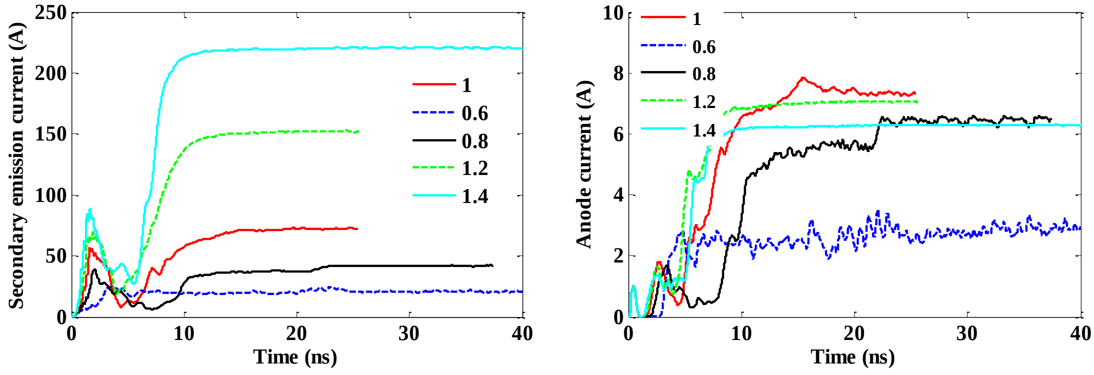

(a) (b)

Figure 3.37 Secondary emission current (a) and anode current (b) when secondary emission coefficients are 0.6*δ, 0.8*δ, 1.2*δ, 1.4*δ.

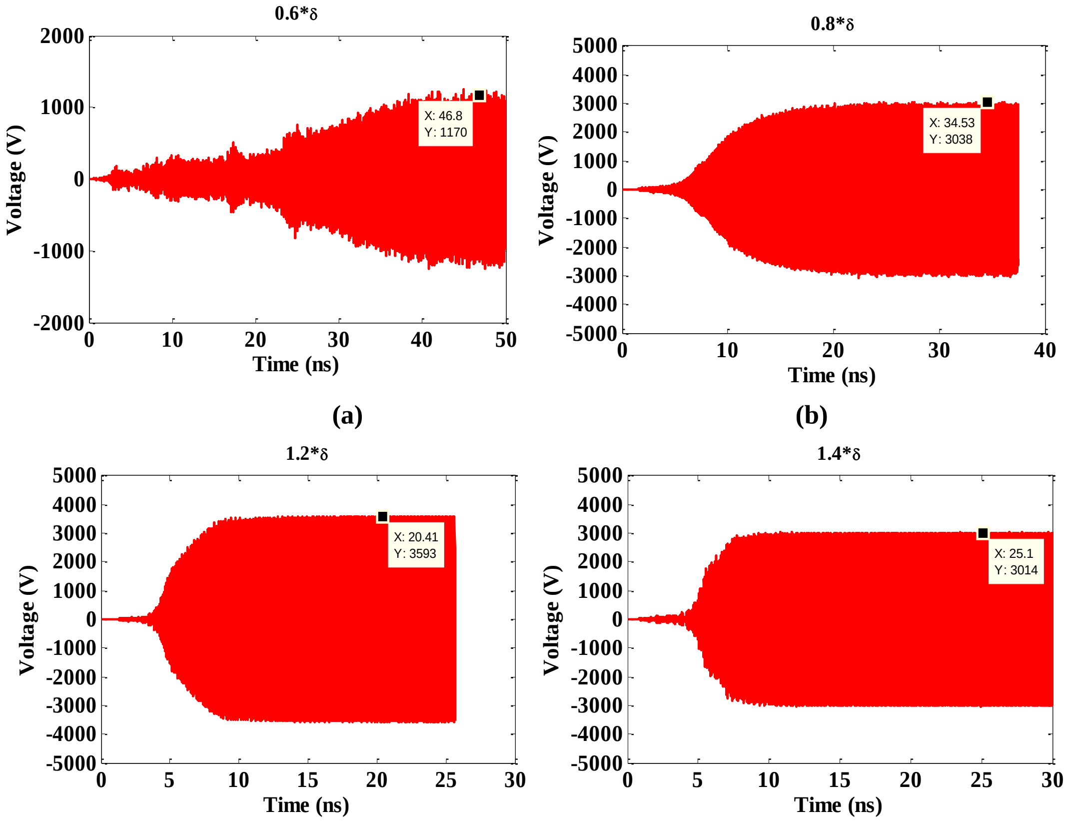

(a) (b)

(c) (d)

Figure 3.38 Output voltages when secondary emission coefficients are (a) 0.6*δ, (b) 0.8*δ, (c) 1.2*δ, (d) 1.4*δ.

The simulation results including frequency, output power, anode current, secondary emission current (I_s), back bombarding current (I_b), and efficiency for various electron secondary emission coefficients are summarized in Table 3-7. The investigation of the magnetron performance with different secondary emission coefficients indicates that the effective range of the secondary emission coefficient is from 0.8*δ to 1.2*δ. It is possible to simplify the manufacturing by make the cold cathode by pure inexpensive metals with relative lower secondary emission coefficient, like copper or molybdenum, rather than plating it with platinum. The resulting decrease of the efficiency and the output power is small enough to justify for a lower manufacturing cost.

Table 3-7 Simulation results with various secondary emission coefficients

Secondary emission coefficient	f GHz	P_{out} kW	I_a A	I_s A	I_b A	η %
0.6δ	35.2	1.4	2.7	21	23	4
0.8δ	35.2	9.8	6.4	41.8	40	12
δ	35.2	15.9	7.3	72	70	17
1.2δ	35.2	13.7	7.06	152	150	15.1
1.4δ	35.2	9.6	6.3	220	219	11.9

3.5 Effects of the External Quality Factor

In the SHM, the RF power is coupled through a slot at one of the side resonators. External quality factor Q_{ext} can be adjusted by tuning coupler widths. As shown in Figure 3.39, the values of the external quality factor Q_{ext} reduce from 680.4 to 170.5 when the coupler widths increase from 0.15 mm to 0.45 mm. For all of these simulations, Q_{ext} and B are set to be equal to 12.8 kV and 0.5875 T, respectively. The external quality factor does not change the oscillation mode. All of them oscillate on the π/2-1 mode of the -1th spatial harmonic. The simulation results in Table 3-8 shows that the efficiency monotonically increases with smaller Q_{ext}. The output power decreases from 16kW to 10.2kW when Q_{ext}>600.

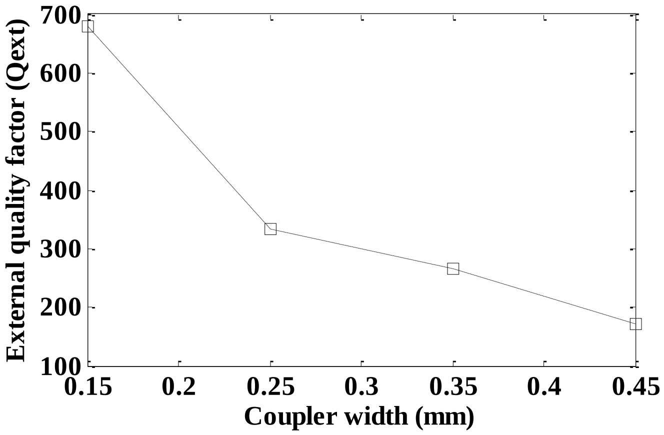

Figure 3.39 External quality factors versus with various coupler widths.

Table 3-8 Simulation results with various external quality factors

Coupler width (mm)	0.15	0.25	0.35	0.45
Q_{ext}	680.4	333	264.7	170.5
P_{out} kW	10.2	15.9	16	15.2
I_a A	7.6	7.3	6.7	5.1
η %	10.5%	17%	18.6%	23.2%
f GHz	35.2	35.2	35.2	35.25
$\|k\|$	13	13	13	13
I_s A	88	72	64	43

3.6 Investigation of the Stability of a $\pi/2$-mode SHM

3.6.1 Introduction

The transient behaviour of the π/2-1 mode SHM shows that the neighbouring π/2 mode competes with the operating π/2-1 mode during the pre-oscillation, due to the fact that their frequencies and phase velocities are close to each other. Thus, it is possible to develop a π/2 mode SHM model based on the π/2-1 mode SHM according to the modification of the anode parameters and correct selection of the operating points [67]. However, the higher mode number has worse mode separation.

In the SHM, there is no additional mode separation structure. Therefore, the SHM operating on higher mode number may suffer from mode instability or narrow dynamic range of the operating points. To verify this, this section will investigate the stability of a $\pi/2$ mode SHM.

3.6.2 Particle simulation of a $\pi/2$ mode SHM

The structure of the simulation model is the same as Figure 3.28, but with different geometrical parameters. The main geometrical parameters of the simulation model are determined from a $\pi/2$ mode SHM as reported in [67], which is developed based on a slight modification of a $\pi/2$-1 mode SHM. The dimensions of anode radius, cathode radius, and anode height are the same as the e $\pi/2$-1 mode SHM. The only differences are that the opening angle of the side resonators increases from 12.5^o to 13.5^o and the vane depth increases slightly from 1.38mm to 1.39mm to obtain maximum output power and efficiency. The geometrical parameters, one of the operation points, and cold simulation results of this simulation model are presented in Table 3-9.

Figure 3.40 shows the dispersion diagrams of the anode block and anode cavity. The frequency of the $\pi/2$ mode (n=4) is 37.47 GHz with the mode separation of 4.3%. Particle simulation is carried out with 5 A seed current from 72 emission points on the cold cathode surface. The axial magnetic flux density B is equal to 0.53 T with a uniform profile in the interaction space. The anode voltage is 12.6 kV with 0.1 ns rise time. The evolution of the space charge is shown in Figure 3.41. The processes of the electron motion, electron secondary emission and spokes formation are similar with those of the $\pi/2$-1 mode SHM. The significant difference is that the number of electron spokes reduces from 13 to 12 at the steady state of the oscillation as shown in Figure 3.41 (d).

Table 3-9 Geometrical parameters of a 16-vane π/2 mode SHM

Number of vanes (N)	16
Cathode radius r_c (mm)	1.3
Anode radius r_a (mm)	2.25
Side resonator depth (mm)	1.39
Aperture opening	13.5
Anode height (mm)	6
Output waveguide	WR28
Copper conductivity (S/m)	5.8e7
Cathode end hat radius (mm)	1.9
The height of the end space(mm)	1
Transformer length (mm)	1.8
Magnetic field (T)	0.53
Anode voltage (kV)	12.6
π/2-1 mode frequency (GHz)and Q_{ext}	34.49, 440
π/2 mode frequency (GHz) and Q_{ext}	**37.47, 453**
π/2+1 mode frequency (GHz) and Q_{ext}	39.08, 455

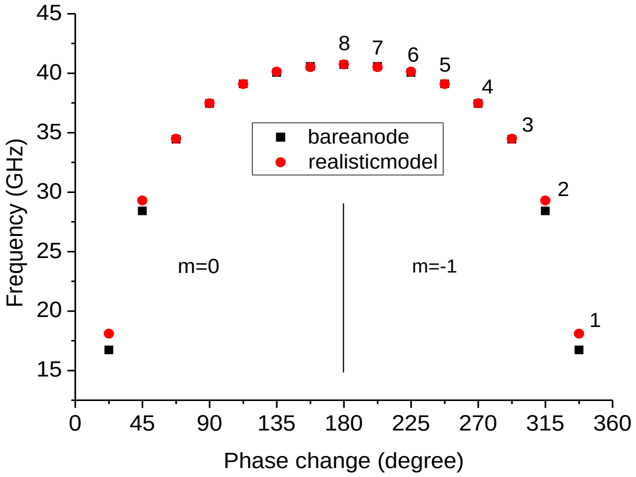

Figure 3.40 Dispersion diagrams of the bare anode and realistic magnetron of a 16-vane π/2 mode SHM.

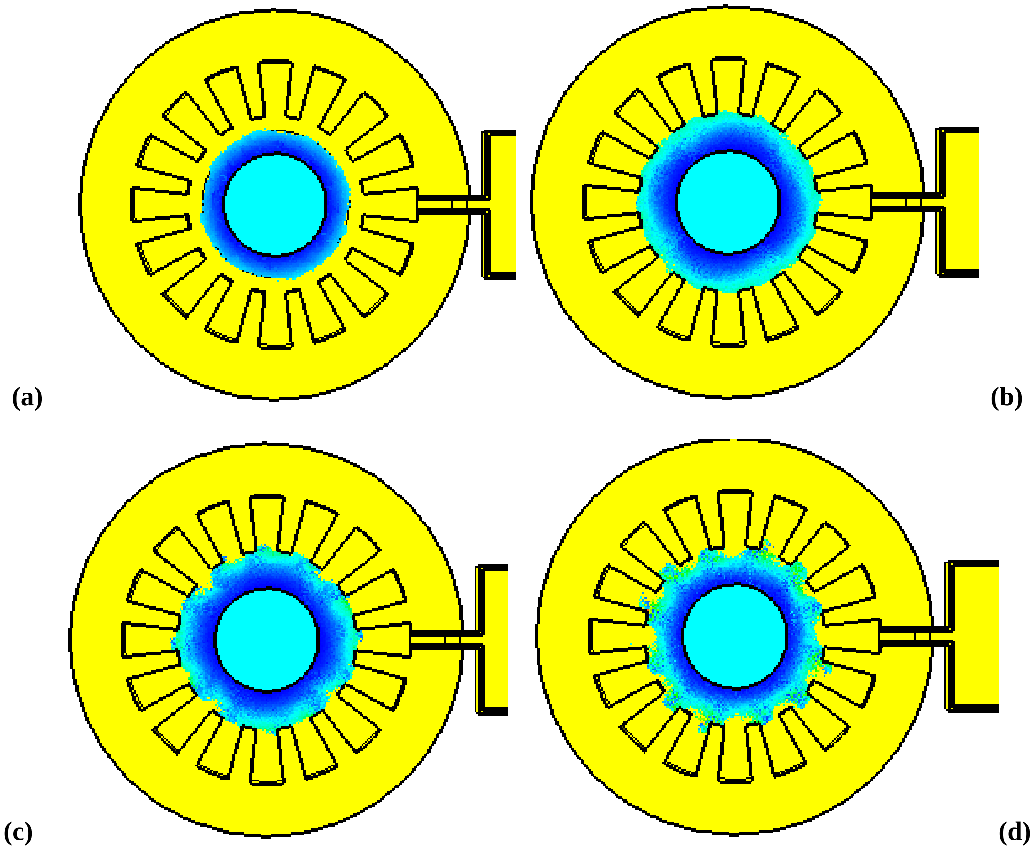

Figure 3.41 Time-evolved spoke formation plotted in the x-y plane at different moments: (a) 0.3 ns, (b) 2 ns, (c) 4 ns, and (d) 20 ns. (12.6kV anode voltage and 0.53T magnetic field).

The output voltage monitored at the centreline of the output port across the WR28 waveguide broad walls is presented in Figure 3.42 (a). Output RF voltage starts to grow abruptly at about 4ns and reaches its saturation value of 4603.7V after 15ns. The corresponding output power is 23.2 kW, which is substantially higher than that of the π/2-1 mode SHM. The oscillation frequency is found to be 37.26 GHz as shown in Figure 3.42 (b). As shown in Figure 3.42 (d), during the pre-oscillation before 10ns, the secondary emission current is lower than the back bombarding current due to the insufficient back bombarding energy. However, after 10 ns when the electrons start to synchronize with the working mode, the back bombarding electrons have sufficient energy to trigger the secondary emission coefficient higher than 1 (leading to the secondary emission current higher than the back bombarding current). The simulation results are summarized in Table 3-10. The simulation is also carried out with 300 emission points. The results have no difference with the model with 70 emission points, but the required simulation time increases from 40 hours to 70 hours.

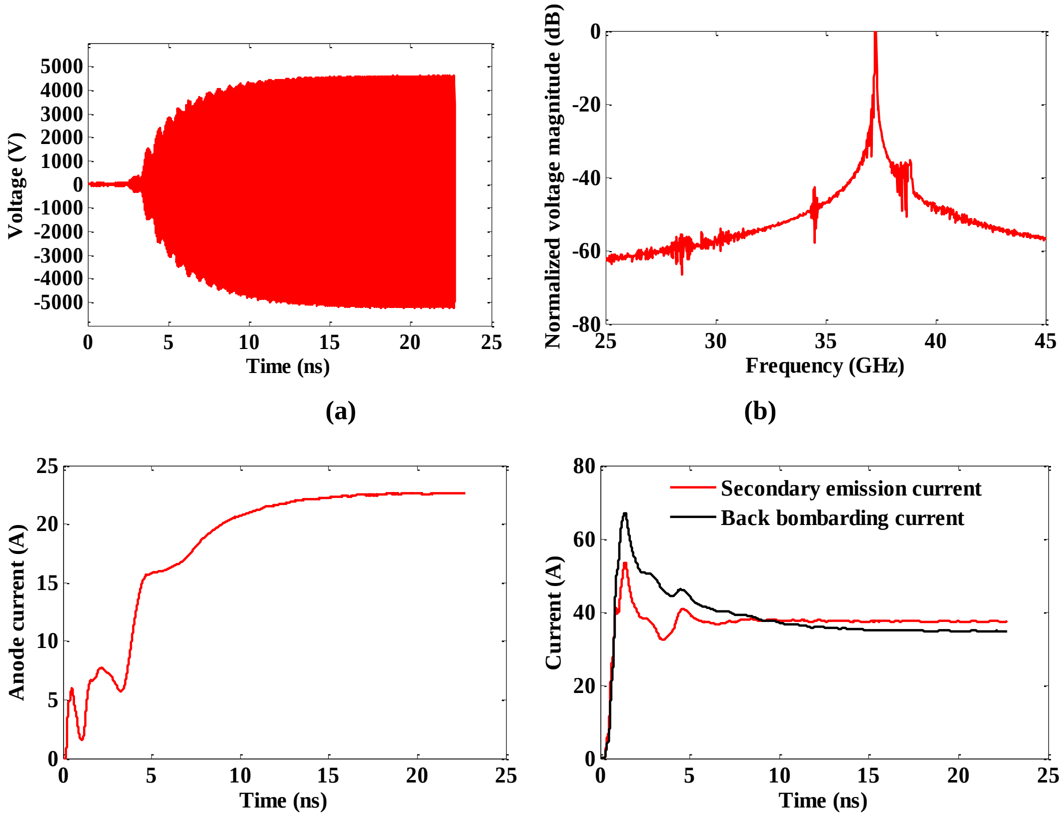

(a) (b)

(c) (d)

Figure 3.42 Simulation results of a $\pi/2$ mode SHM. (a) Output voltage monitored at the centreline of the output port across the WR28 waveguide broad walls; (b) output spectrum with normalized amplitude; (c) anode current; (d) secondary emission current and back bombarding current.

Table 3-10 Simulation results of a π/2-mode SHM

Frequency, GHz	37.26
Output power, kW	23.2
Anode current, A	22.59
Efficiency, %	8%
Secondary emission current, A	37.4
Anode Voltage, kV	12.6
Magnetic field, T	0.53

3.6.3 Mode jumping

In order to investigate the operation range of the anode voltage and to observe if mode jumping happens due to the changing of the anode voltage, the simulations are performed by tuning the anode voltage from 11.4 kV to 13.8 kV while magnetic field keeps constant at 0.53T. Figure 3.43 shows the simulation results of oscillation frequency and electron spokes at the steady state of the oscillations. It can be observed that mode jumping happens due to the voltage tuning.

When the anode voltages are set in 11.2 kV-11.6 kV, there are 13 electron spokes with 34.47 GHz oscillation frequency, which indicates that the SHM is operating on $\pi/2$-1 mode. When the anode voltages are set in 11.6 kV-12.2 kV, 34.47GHz and 37.26 GHz frequencies coexist and there are 13 undistinguishable electron spokes which indicates that it is a transition region from $\pi/2$-1 mode to $\pi/2$ mode. When the anode voltages are set in 12.2 kV-12.8 kV, there are 12 electron spokes with 37.26 GHz frequency which indicates that $\pi/2$ mode is the dominated mode. The output power is quite high in the $\pi/2$ mode operation due to a high anode voltage. When the anode voltages are further increased, the oscillations starts to jump from $\pi/2$ mode to $\pi/2+1$ mode and there are 11electron spokes with 38.9 GHz oscillation frequency.

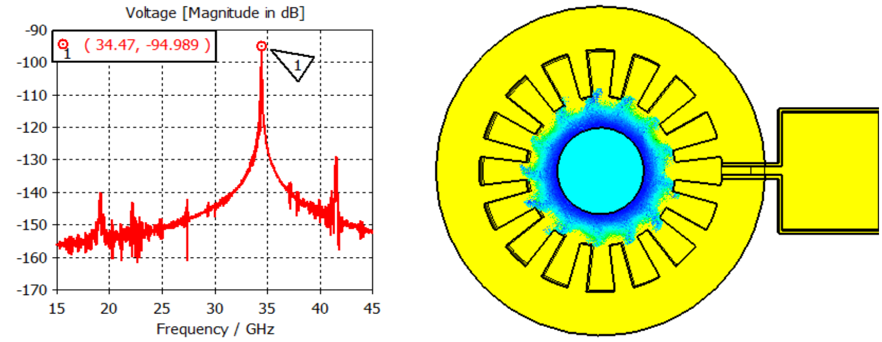

(a) 34.47 GHz; 13 electron spokes versus anode voltage 11.2 kV-11.6 kV.

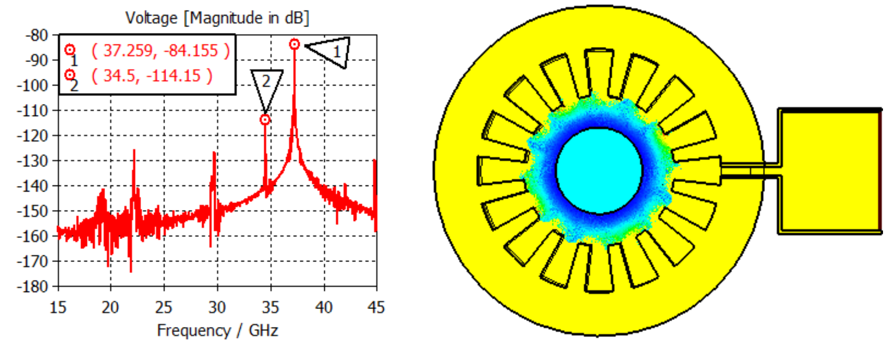

(b) 37.26GHz and 34.5GHz; 12 electron spokes versus anode voltage 12kV.

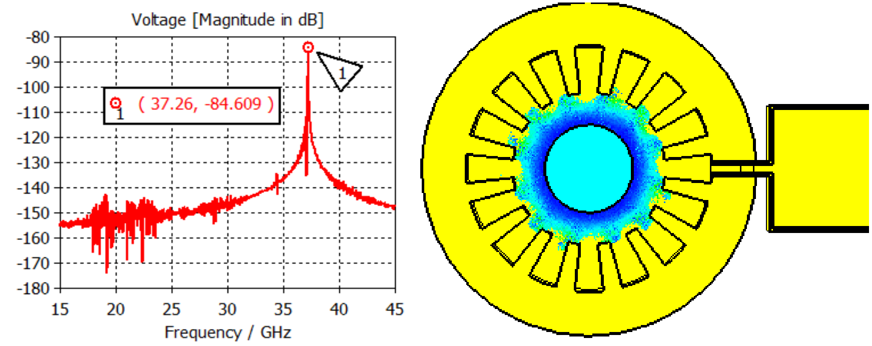

(c) 37.26GHz; 12 electron spokes versus anode voltage 12.2 kV-12.8kV.

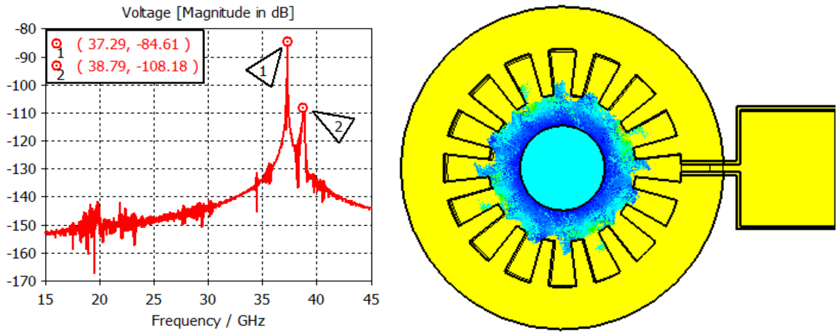

(d) 37.29GHz and 38.79GHz; 12 electron spokes versus anode voltage 13kV-13.2kV.

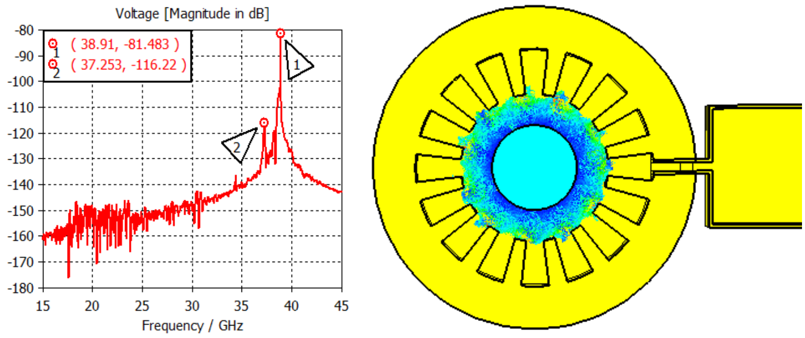

(e) 38.9GHz and 37.25GHz; 11 electron spokes versus anode voltage 13.4kV-13.8kV.

Figure 3.43 Output frequency and electrons spokes when anode voltage increases from 11.4 kV to 13.8kV.

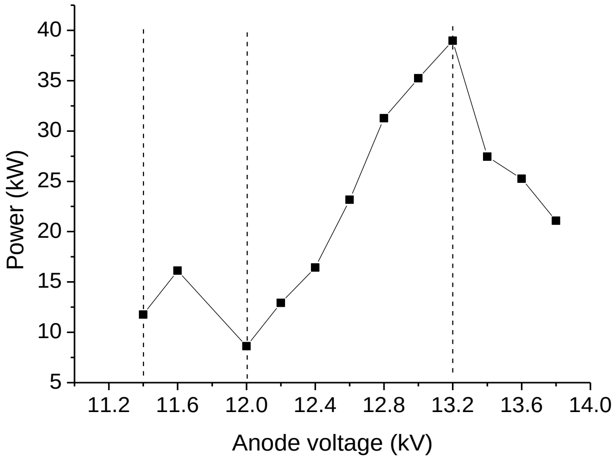

Figure 3.44 Output power versus anode voltages 11.2kV-13.8kV when B= 0.53 T.

The oscillation fails to start if the anode voltage is above 13.8kV, exceeding the Hull cut-off voltage. Figure 3.44 shows that the output power linearly increases when the magnetron is operating on $\pi/2$ mode (anode voltage 12 kV- 12.8 kV) and reaches its maximum value of 39 kW at 13.2 kV. The output power obviously drops when it is operating on $\frac{\pi}{2}-1$ mode (anode voltage below 11.4 kV-12 kV) or when it is operating on $\frac{\pi}{2}+1$ mode (anode voltage 13.4 kV-13.8 kV). The anode currents are shown in Figure 3.45.

From the theory of the electron wave interaction, the electron velocity can be decomposed into radial direction component and azimuthal direction component. When the anode voltage increases, the radial velocity increases faster than the azimuthal one. As we know, the electron-wave interaction mainly depends on the electron azimuthal velocity. Therefore, the slowly increasing azimuthal velocity allows magnetron operate on $\pi/2$ mode in a wide anode voltage range (12.2kV-12.8kV). However, when the anode voltage further increases or decreases, the space charges lose the synchronization with the operating mode and the efficiency drops down.

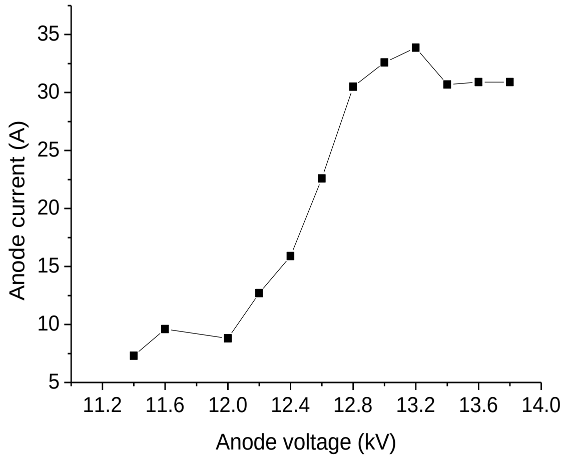

Figure 3. 45 Anode currents versus anode voltages 11.2kV-13.8kV when B=0.53 T.

Mode jumping can also be explained with Hartree resonant conditions of different modes. Figure 3.46 shows Hull cut off parabola and Hartree resonant lines of different modes. The Hartree resonant lines of π/2-1 mode (k=13), π/2 mode (k=12) and π/2+1 mode (k=11) are close with each other. The operating point of the π/2 mode is located above k=12 curve and below k=11 curve. When the anode voltage is varied, the operating point may shift to its neighbouring resonant lines. Thus, mode jumping happens.

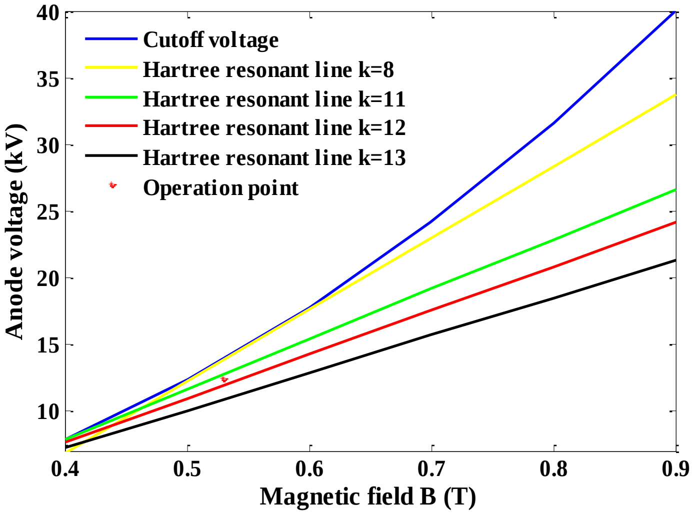

Figure 3. 46 Hull cut off parabola, Hartree resonant condition of different modes, and operation point of π/2 mode.

3.7 Summary

In this chapter, the operation of a 35 GHz $\pi/2-1$ mode SHM with side cathode and main cathode has been investigated by using 3-D particle simulation, including cold cavity properties, transient behaviour and steady state of the oscillations, and electron dynamics. The transient behaviour shows that the neighbouring mode is the main competitor to the operating mode. The particle dynamic shows that there are several main stages of the particle trajectories: electron injection, electron accumulation, electron secondary emission and space charge-wave interaction. The injection current is just to provide accumulating electrons near the cathode and its value does not affect the magnetron output performance obviously. As compared with conventional magnetron, the electron spokes in the SHM distributes irregularly.

A fast and reliable simulation approach has been developed. The magnetron output performances with different secondary emission coefficients and the effect of the external quality factor have been investigated by using this simulation approach. It demonstrates that there is a threshold value of the secondary emission coefficient for the magnetron operation. This may open a way to select cheaper cathode materials with relative lower secondary emission coefficient to simplify the magnetron construction and reduce the cost.

The operation of a $\pi/2$ mode SHM has also been investigated in simulation. A substantially higher output power can be achieved in this mode. However, the mode jumping might spoil the SHM operation because of a narrower mode separation.

Chapter 4 W-band Spatial Harmonic Magnetron for the Application of Cloud Radar

4.1 Introduction

Millimetre-wave Doppler radars are considered now as the most practical instruments for permanent monitoring and investigation of cloud. At present, most of the millimetre-wave Doppler radars are based on truly coherent system. However, the lack of cost-effective, high power millimetre-wave amplifier, especially for the frequencies of 95 GHz and higher, limits the development of such types of radars intended for long distance operation. In order to tackle this problem, the main objective of this chapter is to model and develop a cost effective 95GHz SHM for the application of coherent-on-receiver cloud radar.

4.2 3-D Modelling of a 95 GHz π/2-1 Mode SHM

The basic structure of a 95 GHz SHM is the same as the Ka-band SHM, but with more side resonators and smaller dimensions. It consists of thermionic side cathode, platinum cold secondary emission cathode, anode block and output structure. The simulations are performed by the use of a simplified model which is without the side cathode as introduced in Chapter 3. Instead, the initialized bombarding current which is a small amount of the total current in the SHMs, is provided by specifying a relatively small seed current 5A to the cold cathode. This primary emission is sufficient to initiate the emission of secondary electrons.

Figure 4.1 illustrates cut away views of the simulation model. It consists of the following: 1) 24-vane unstrapped anode block; 2) a quarter-wavelength transformer; 3) WR-10 output waveguide; 4) platinum cold secondary emission cathode together with non-magnetic end caps; 5) DC voltage input port. The most important geometrical dimensions of this model are presented in Table 4-1.

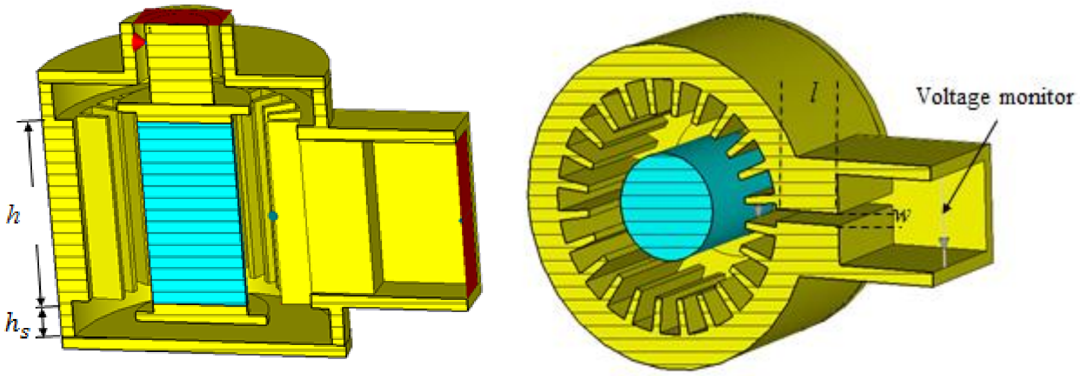

Figure 4.1 Simulation model of a 24-vane 95 GHz π/2-1 mode SHM.

Table 4-1 Geometrical parameters and cold simulation results of a 95GHz SHM

Number of vanes	24
Cathode diameter (mm) N	1.52
Anode diameter (mm) r_a	2.6
Anode length (mm) h	3
Vane depth (mm) d	0.5
Resonator opening θ	10.6^{o}
Output waveguide	WR 10
Copper conductivity (S/m)	5.8e7
End space (mm) h_s	0.6
Transformer length (mm) l	1
Transformer width (mm) w	0.17
Primary current	5 A

Table 4-2 Cold cavity simulation results

π/2-1 upper mode frequency (GHz)	**95.43**
π/2-1 upper mode Q_0,Qext, Q_L	**890, 248.6, 194**
π/2-1 upper mode circuit efficiency	**78%**
π/2-1 lower mode frequency (GHz)	95.12
π/2-1 lower mode $Q_{0,}$ Qext, Q_L	879,1.9e6, 879
π/2 upper mode frequency (GHz)	100.3
π/2 upper mode Q_0,Qext, Q_L	881, 4e6, 881
π/2 lower mode frequency (GHz)	99.83
π/2 lower mode Q_0,Qext, Q_L	870, 207.8, 167.7

As magnetron cavity consisting of equal resonators, all modes except for the π-mode are degenerates. Due to the energy output in one of the anode resonators, the degenerate modes form doublets, a pairs of modes with close resonant frequencies and essentially different Q factors. It causes the over coupling of the low Q mode to the output and at the same time suppress the oscillation of the high Q mode. The cold cavity simulation results are shown in Table 4-2.

The external quality factor of a 95.43 GHz upper π/2-1 mode is 248, while that of the 95.12 GHz lower π/2-1 mode is 1.9e6. The external quality factor $\mathrm{Q_{ext}}$ is defined as

$$Q_{ext} = 2\pi f_0 \frac{W}{P_{out}} \tag{4.1}$$

where W is the system's stored RF energy, f_0 is the resonant frequency, P_{out} is the output power. Thus, for the 95.12 GHz doublet, there is a very low energy coupled to the load. Thus, the degenerated modes are well separated.

The simulated electric field pattern of the upper π/2-1 mode is shown in Figure 4.2, where the phase difference between the neighbouring resonators is 75^{o}. The mode separation is 4.6%. The circuit efficiency of the cavity is < 100% due to copper surface loss and it is can be expressed in terms of η_c

$$\eta_c = \frac{Q_{load}}{Q_{ext}} \qquad 4.2$$

The calculated circuit efficiency of 95.43 GHz π/2-1 mode is 78%.

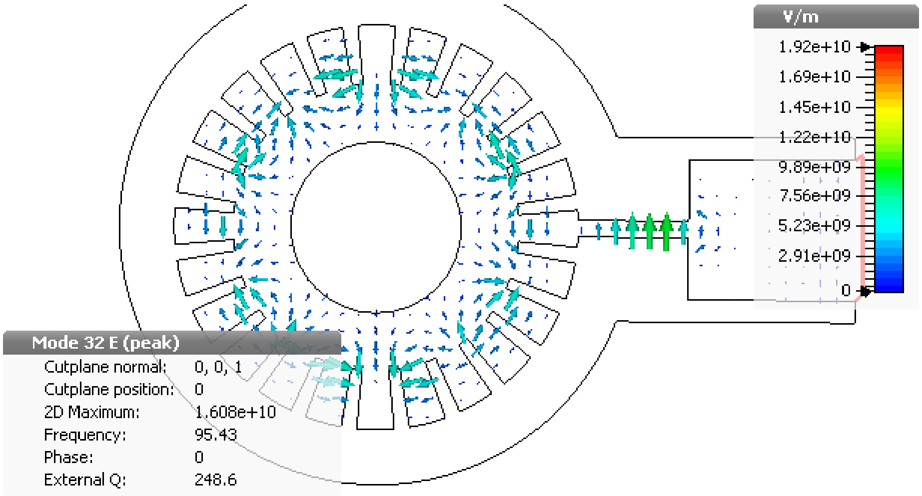

Mode 32 E (peak)
Cutplane normal: 0, 0, 1
Cutplane position: 0
2D Maximum: 1.608e+10
Frequency: 95.43
Phase: 0
External Q: 248.6

Figure 4.2 Electric field pattern of the π/2-1 mode.

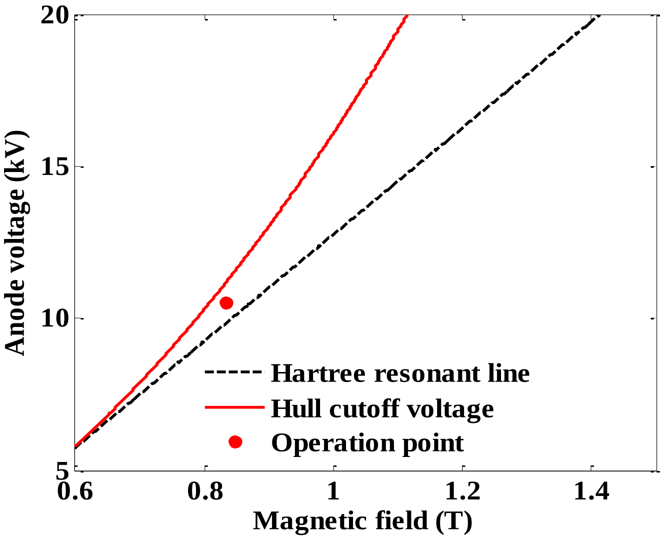

Figure 4.3 Hull cut off voltage, Hartree voltage, and operation point.

Figure 4.3 depicts the Hull cut off parabola, Hartree resonant condition, and one of the operation points of this SHM (V_{dc}=10.5kV; B = 0.833T). The operation conditions are in the region between the cut off parabola and Hull resonant line. Figure 4.4 (a)-(c)

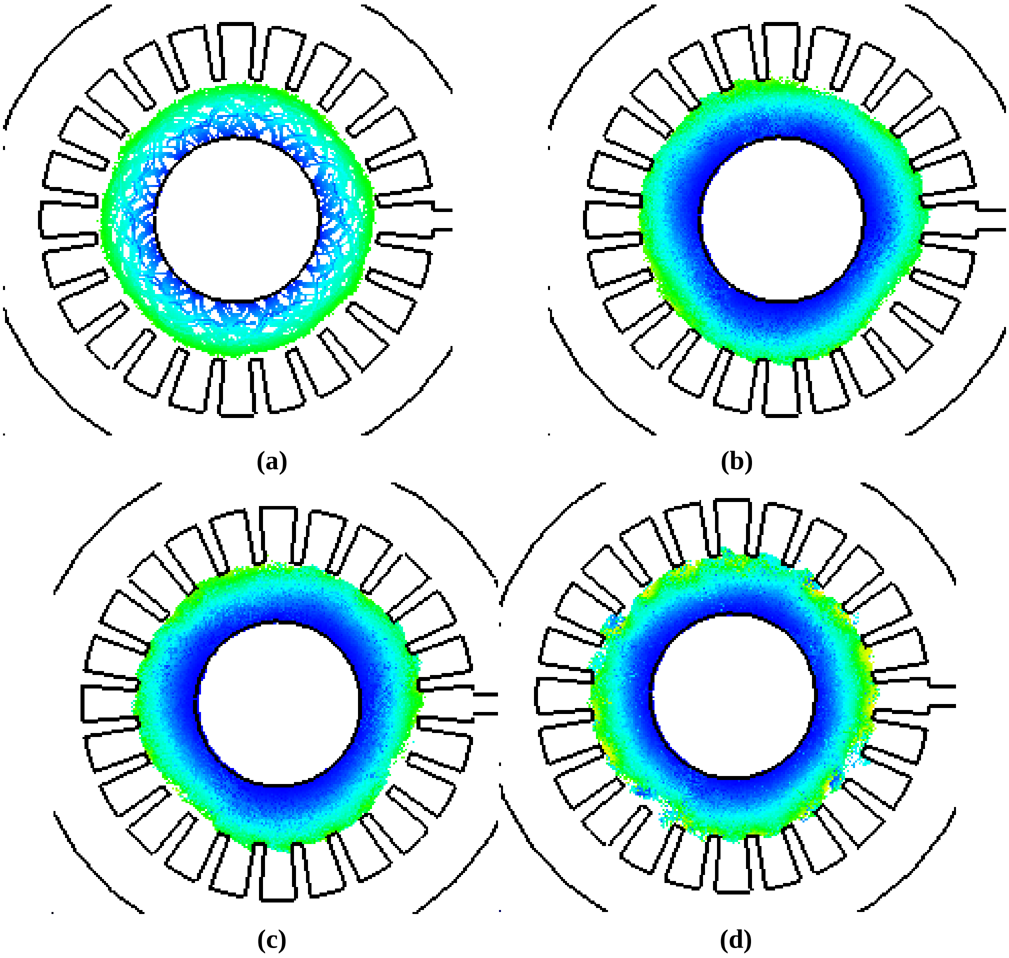

Figure 4.4 Time-evolved spoke formation plotted in the x-y plane at (a) 0.2 ns, (b) 2ns, (c) 5 ns, and (d) 15 ns. There are 19 electron spokes at the steady state of the oscillation, which conforms that it is operating on the -1th spatial harmonic of π/2-1 mode. V_{dc}=10.5kV; B = 0.833T.

shows the space charge distributions in the x-y plane during the pre-oscillation state at 0.2 ns, 2 ns and 5 ns respectively. The electron cloud initially forms in the area near the emission points assumed on the cathode and then expands until it fills the whole interaction space. When the simulation time is 5 ns, there are indications of electron spokes originated near the anode surface due to the synchronous interaction between the rotating electron cloud and the spatial harmonic mode in the interaction space. After the oscillations are saturated after 15ns, as shown in Figure 4.4 (d), the 19 electron spokes are fully formed, which confirms that the spatial-harmonic magnetron is operating at π/2 -1 mode of -1th spatial harmonic.

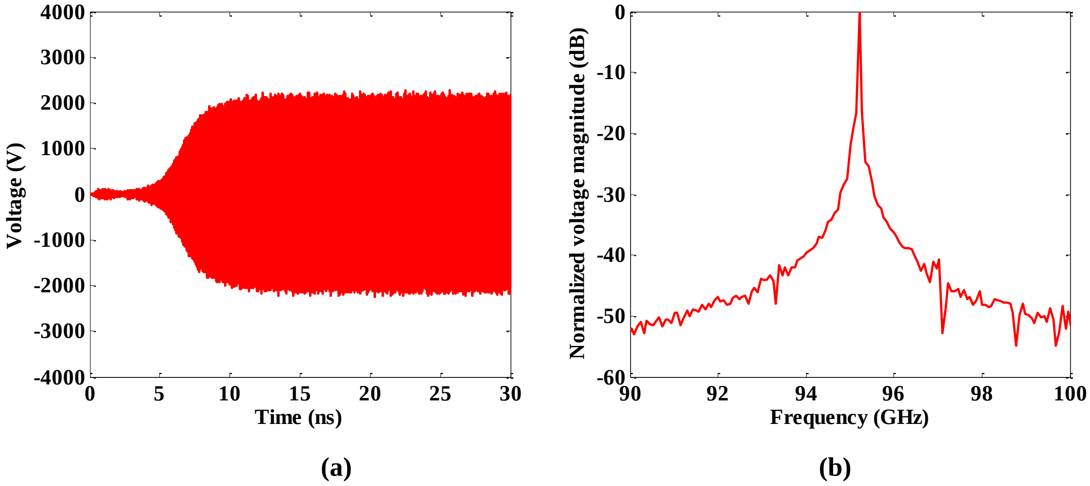

Figure 4.5 (a) Output voltage amplitude measured at the centre line of the output port across the output waveguide broad walls. (b) Normalized amplitude of the frequency spectrum obtained from a Fourier transform of the time-varying output voltage. The results are for V_{dc}=10.5kV; B = 0.833T.

Figure 4.5 (a) shows the time evolution of the output voltage amplitude measured at the centre line of the output port across the output waveguide broad walls, while Figure 4.5 (b) shows its corresponding spectrum. Output voltage starts to grow abruptly at about 7ns and reaches its saturation value 2280V after 12ns. Considering 59.05GHz cut off frequency of WR-10 waveguide, the saturated output power is equal to 5.4 kW calculated using Equation 3.3. As it can be observed in Figure 4.6, there is a nearly constant current of about 9.6 A collected on the anode (I_a). Considering 10.5 kV anode voltage (V_{dc}) and 5.4 kW saturated output power (P_{out}), the input power is 110.8 kW. The power conversion efficiency η is 5.35% calculated by

$$\eta = \frac{P_{out}}{U_a I_a} \qquad 4.3$$

Figure 4.6 shows that 38.3A secondary emission current is generated under 33.5A secondary emission current. The averaged secondary emission coefficient is 1.14. The cathode current density is as high as 267 A/cm^2 which is hard to be achieved by classical thermionic cathode. High emission current density is one of the advantages of the secondary emission cold cathode. The primary current specified on the cold cathode is 5 A which is much smaller than the secondary emission current. Therefore, the total cathode current comes from the electron secondary emission.

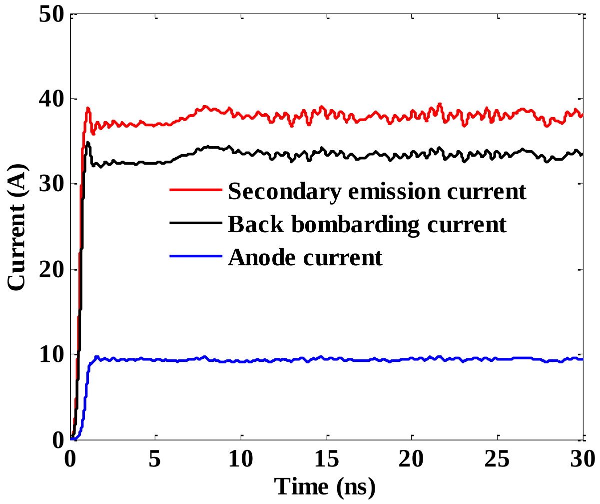

Figure 4.6 Secondary emission current (38.3A), back bombarding current (33.5A) and anode current (9.6A). V_{dc}=10.5kV; B = 0.833T.

Table 4-3 Output performance of the magnetron for different values of the magnetic field and the anode voltage

V_{dc} kV	B T	P_{out} kW	I_a A	η %	I_s A	f GHz
10.3	0.833	4.1	8	4.97	35	95.21
10.4	0.833	4.4	8.3	5	36.1	95.21
10.46	0.833	4.8	9	5.1	36.8	95.21
10.48	0.833	5.06	9.2	5.24	37.5	95.21
10.5	0.833	5.4	9.6	5.35	38.3	95.21
10.6	0.833	6	10.5	5.4	38.3	95.21
10.5	0.83	5.82	10.4	5.3	38.6	95.21
10.5	0.835	4.9	9	5.18	38.2	95.21

The output parameters of the simulation model including output power (P_{out}), anode current (I_a), efficiency (η), and secondary emission current (I_s) for different operation points are presented in Table 4-3. When the magnetic field is 0.833T and anode voltages are varied from 10.3kV to 10.6kV, the output power is increased from 4.1kW to 6kW. The output power is sensitive to the value of the magnetic field. When anode voltage is 10.5kV and the magnetic field reduces from 0.833T to 0.83 T, the output power is increased from5.4kW to 5.82kW.

4.3 Considerations Regarding the Pulse Duration Selection and Vacuum Break Down

The copper surface of the anode cavity is heated up during each pulse and is cooled down between the pulses. Expansion and contraction of the anode surface cause internal stress which in turn creates non-uniformities. When the number of the pulse and the pulse width is large, the non-uniformities join together and create micro cracks which make heat conduction more difficult and causes a sharp rise in the anode temperature, so that the outer layer of the anode starts to melt, spray out, and evaporate. It leads to intensive metal condensation onto the cathode which may cause frequency shift, unstable secondary electron emission, electrical breakdown, short life time and eventually make devices fail.

Copper is a commonly used material of the magnetron anode, the equation of the temperature on the anode surface (T) can be simplified as below [68]

$$T = \frac{0.3\, P_a \sqrt{\tau}}{S_a} \tag{4.4}$$

$$S_a = 2\pi r_a h \gamma \tag{4.5}$$

where P_a is the dissipated power on the anode in kW, τ is the pulse duration in us, $\mathrm{S_a}$ is the anode surface area in cm^2, γ is the ratio between the anode vane thickness and the width of the side resonator, h is the height of the anode, and r_a is the anode radius. For this magnetron, r_a=1.3mm, h=3mm, γ=0.707, thus, S_a is 0.173 cm^2.

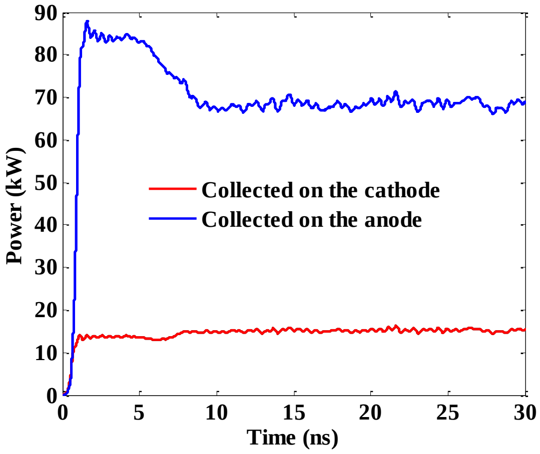

Figure 4.7 70 kW power dissipated on the anode.

According to the safety rule, the temperature of the copper anode T should not exceed 110 ◦C. As shown in Figure 4.7, for an output power of 5.82 kW whenV_{dc} =10.5kV and B=0.83T, the dissipated power on the anode block P_a is about 70 kW. Using Equation 4.4 and considering P_a=70 kW, it can be conclude that the pulse duration τ should be less than 900ns.

On the other hand, the vane tips of the designed SHM are only 0.24 mm apart and vacuum breakdown may occur due to the high RF field between vanes. A threshold value for the electric field and voltage at which breakdown may be expected to occur depends on the pulse duration τ which is determined using [69]

$$E_t < \frac{8000}{V_t} \quad \text{(For long pulse } \tau \geq 1\text{ms)} \tag{4.6}$$

$$E_t < \frac{1000}{V_t \tau^{0.34}} \quad \text{(For short pulse } \tau < 1\text{ms)} \tag{4.7}$$

Where V_t is voltage in kV, E_t is the electric field amplitude in kV/cm. τ is in s. Using equation 4-4 and considering pulse width τ=900 ns, the electric field magnitude threshold E_t of this magnetron is equal to 2177 kV/cm.

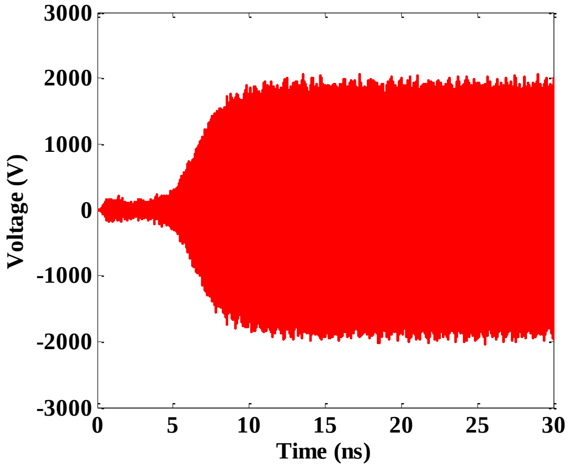

Figure 4.8 Voltage amplitude monitored between the neighbouring vanes of the anode cavity.

At the resonator opening, the electric field which is nearly uniform can be calculated using

$$E = V/r_a\theta \qquad 4.8$$

where V is the voltage amplitude between the neighbouring vanes, r_a and θ are the anode radius and resonator opening angle, respectively.

As shown in Figure 4.8, the voltage amplitude between the neighbouring vanes is 1.9 kV. The calculated electric field amplitude E at the resonator opening is 248 kV/cm. This value is far below the threshold electric field. Thus, from both thermal and vacuum breakdown analysis point of view, the pulse duration of this magnetron should not exceed 900 ns.

4.4 95 GHz Magnetron Transmitter

4.4.1 Introduction

Based on this magnetron, a transmitter has been developed in the Institute of Radio Astronomy of National Academy of Science of Ukraine (IRA NASU). It is remote controlled by a standard interface RS-422. The supply voltage is 220V-240V AC. The weight is 14kg with dimension of 46.cm × 41.2cm× 14.7 cm. The photograph and a simplified block diagram of the transmitter are shown in Figure 4.9 and Figure 4.10, respectively. The main parts of the transmitter are high voltage power supply, high voltage modulator, filament power supply, control board and magnetron.

Figure 4.9 Photograph of a transmitter based on 95 GHZ SHM.

The modulator utilizes a circuit with partial discharge of capacitors and a single-pole floating switch to form pulsed near-rectangular waveform across the magnetron. Two 0.05μF capacitors in parallel are used as the energy storage in the magnetron modulator. The essential difference of such type of the modulator from the line modulator is that only a small part of energy accumulated in an appropriate storage is used to form the output pulse. Since this type of modulator does not require the utilization of the matching circuit to the magnetron, it provides a much better shape of the output pulse than the line modulator [70]. The pulse width and duty cycle can be adjusted by 3V TTL trigger signal from an external pulse generator.

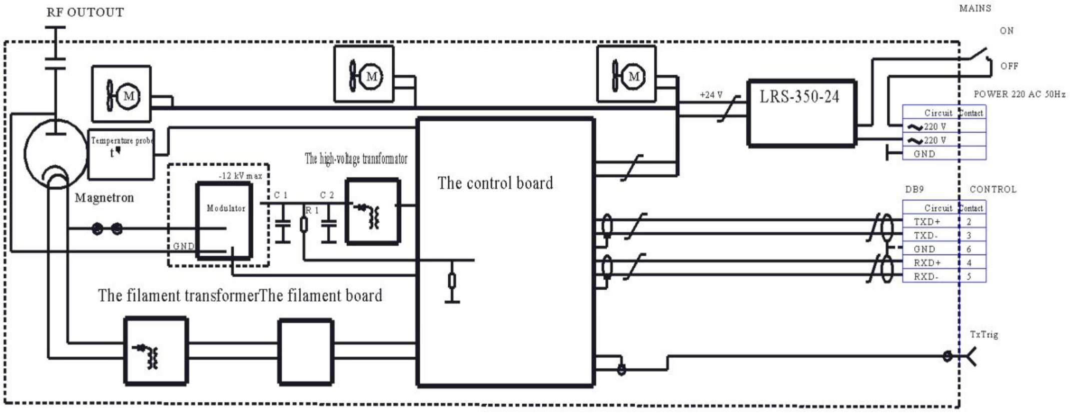

Figure 4.10 Simplified block diagram of a 95GHz magnetron transmitter.

The stability of the cathode temperature is an important issue to prolong the magnetron lifetime. The cathode temperature depends on both of the applied filament power and cathode power dissipation due to electron back bombardment. The cathode temperature should be kept within a rather narrow interval of several tens degrees typically. In this magnetron, 2.2V DC filament voltage is used. This DC voltage can not only reduce the magnetron noise, but also enable a digital controller to measure both filament voltage and current and to transfer the corresponding data to external computer.

Electrical breakdowns may not only contaminate the vacuum condition inside the magnetron, but also may damage the magnetron if there is no current limitation provided by the modulator circuit. However, as MOSFETs are in series connection in the high voltage switch, the limit current value of the modulator is defined by the maximal rated current of the transistors used. So, there is a contradiction between the necessity both to limit the output current and to ensure a minimal settling time of the output voltage of the modulator. Moreover, MOSFET are characterized by a rather low rated dU/dt capability. The transient intense voltage fluctuation due to the electric breakdowns may damage the transistors.

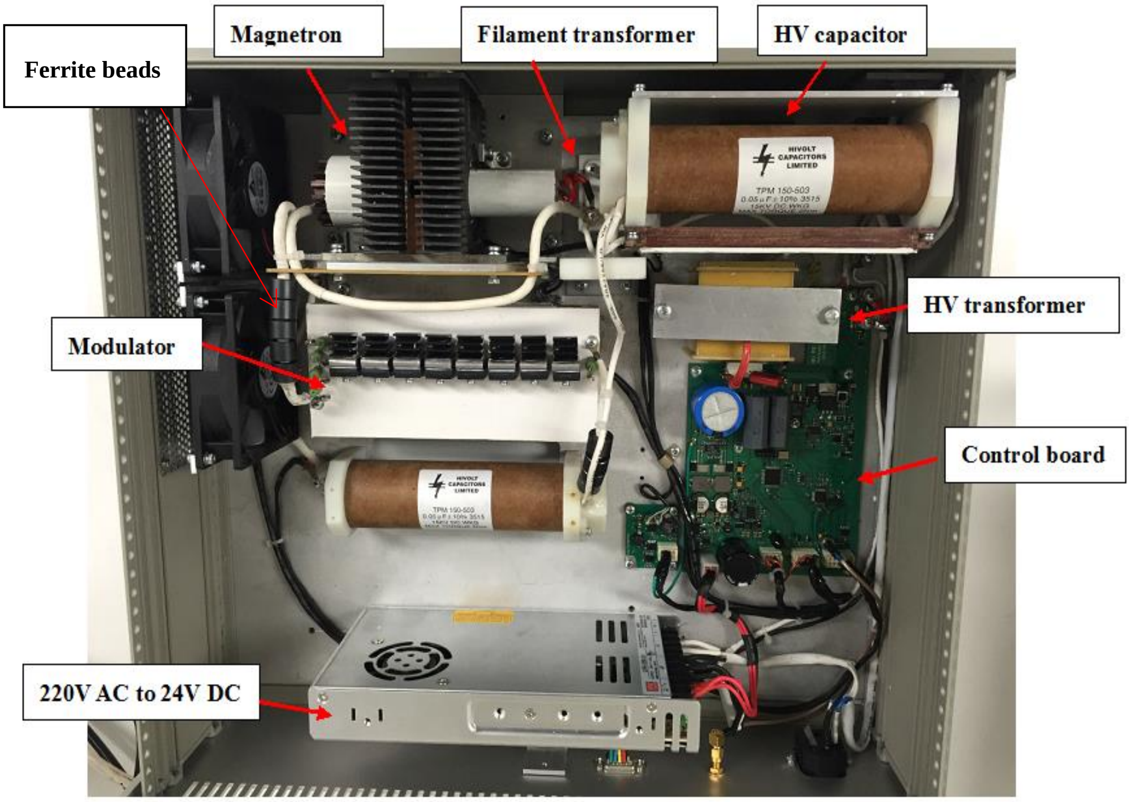

Figure 4.11 Photograph of a W-band magnetron transmitter.

In this transmitter, there is a simple way that uses some ferrite beads connected in series with the magnetron to improve the magnetron voltage stability as shown in Figure 4.11. This effect may be explained as follows. Breakdown in the magnetron appears usually in two stages. The first stage caused by field emission from a tip located somewhere inside magnetron. This stage runs very fast, typically during several nanoseconds. It cause negligible damages of the magnetron internal parts, but initiates developing the next stage which are overheating, cooper sputtering, and further arcing. This stage requires much longer time to run but can cause significant degradation of the magnetron performance. The ferrite beads have rather high impedance under transient conditions. Thus, it leads to fast decrease in the voltage across magnetron during the first stage of the breakdown and prevents developing of the second stage. The ferrite beads also prevent electromagnetic interferences due to the magnetron current fluctuation and increase the overall stability of the transmitter operation [70-72].

The magnetron temperature is measured by a sensor connected to a dedicated connector placed on the modulator PCB. The anode voltage and current are measured at a number of key test points and exported to external PC via a standard interface RS-422. The main window of the transmitter remote control program is shown in Figure 4.12.

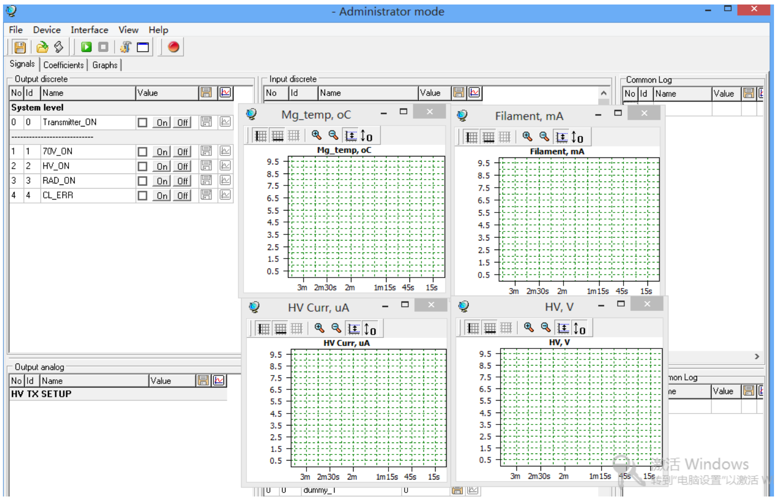

No	Id	Name	Value
System level			
0	0	Transmitter_ON	☐ On Off
1	1	70V_ON	☐ On Off
2	2	HV_ON	☐ On Off
3	3	RAD_ON	☐ On Off
4	4	CL_ERR	☐ On Off

HV TX SETUP

Figure 4.12 The main window of transmitter control program.

4.4.2 Frequency of output signal

The output signal frequency of the magnetron transmitter is measured by R&S FSP spectrum analyser. However, the frequency range of the spectrum analyser is below 40GHz. In this measurement, the frequency range of the spectrum analyser is extended to 75GHz - 110GHz by the use of an 8th harmonic mixer R&S FS-Z110. Figure 4.13 shows the schematic of the frequency measurement. A large amount of the output power of the magnetron transmitter is absorbed by a load with capacity of 10 kW peak power and 10 W average power. A small amount of the power is extracted by a directional coupler.

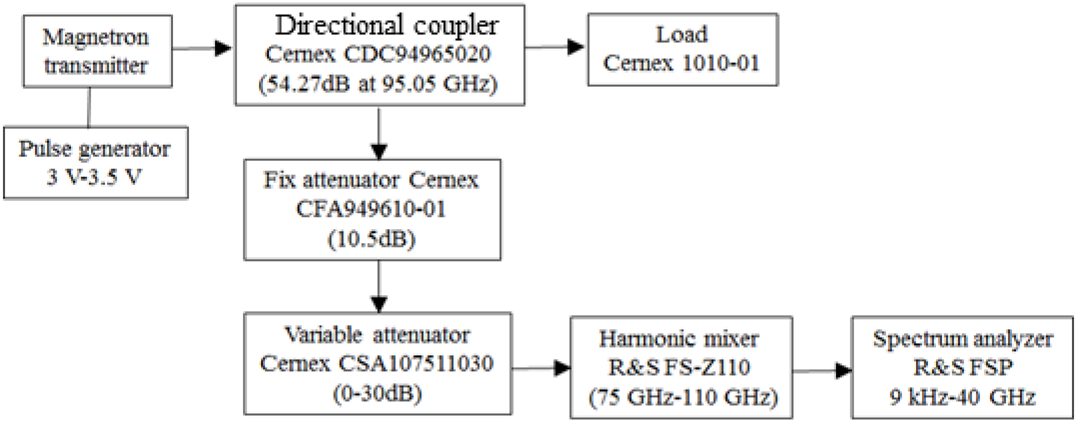

Figure 4.13 The schematic of frequency measurement.

Figure 4.14 The setup of the frequency measurement.

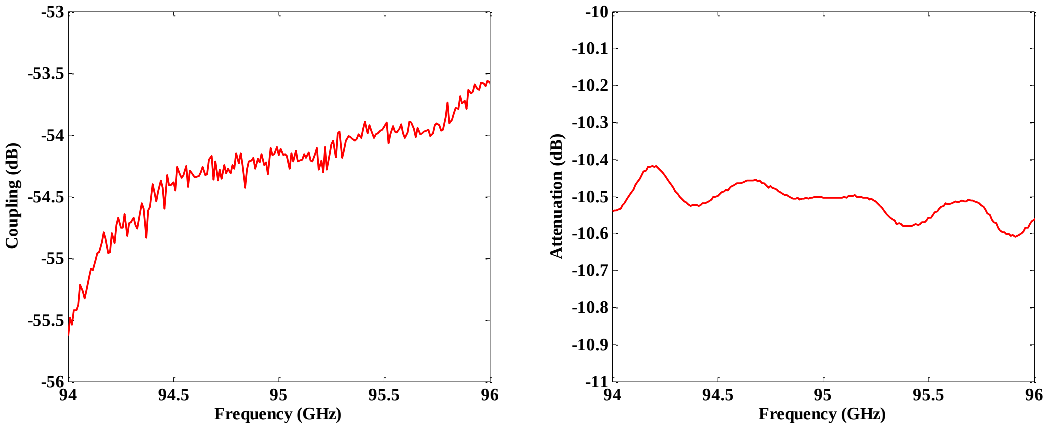

(a) (b)

Figure 4.15 Calibration of the devices. (a) Directional coupler which has 54.27 dB coupling at 95.05 GHz; (b) fix attenuator which has 10.5dB attenuation at 95.05 GHz.

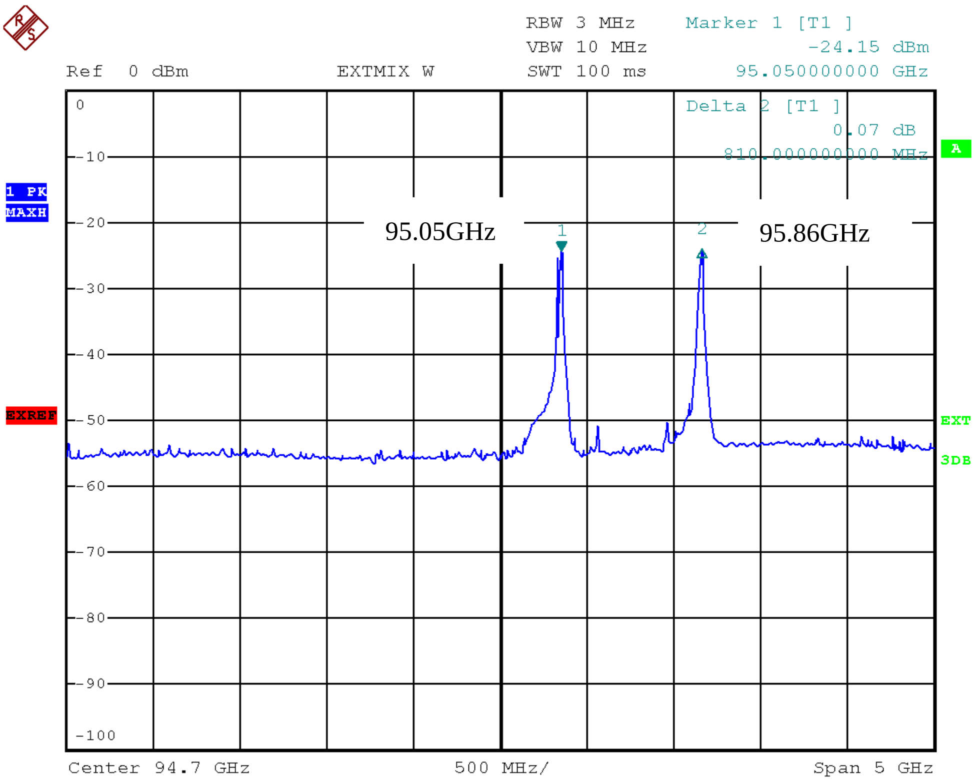

Figure 4.16 Frequency spectrum measured by R&S FSP spectrum analyser associated with R&S FS-Z110 8th harmonic mixer. There are two frequencies: 95.05 GHz and 95.86 GHz.

As the calibration results in Figure 4.15, the coupling is 54-54.5 dB in the frequency range of 94.5-95.5GHz. A 10.5dB fix attenuator and a 0-30dB variable attenuator are placed in the signal path between the directional coupler and the mixer to attenuate the input power of the mixer below 0dBm. The measured results of the directional coupler and fix attenuator are presented in Figure 4.15.

As we know, the RF signal applied to the input of the external mixer together with its harmonics is mixed with all harmonics of the LO signal. Thus, the mixer products that fall within the IF of the spectrum analyser with two frequencies 95.05GHz and 95.86GHz are displayed as shown in Figure 4.16. To distinguish the true frequency from the distortion frequency, modern spectrum analysers provide software algorithms (so called software pre-selectors), which can detect and eliminate the imaginary frequencies before drawing the measured curve on the screen.

For the purpose, we use another straight forward way to distinguish the true signal. As shown in Figure 4.17, a Vector Network Analyser (VNA) is used as a standard frequency source providing 95.05GHz input signal to the mixer. The output frequency of the mixer is measured by the spectrum analyser. As shown in Figure 4.18, 95.86 GHz distortion frequency is displayed. Comparing with Figure 4.16, it could confirm that the magnetron oscillation frequency is 95.05GHz. It is close to the particle simulation result of 95.21GHz frequency.

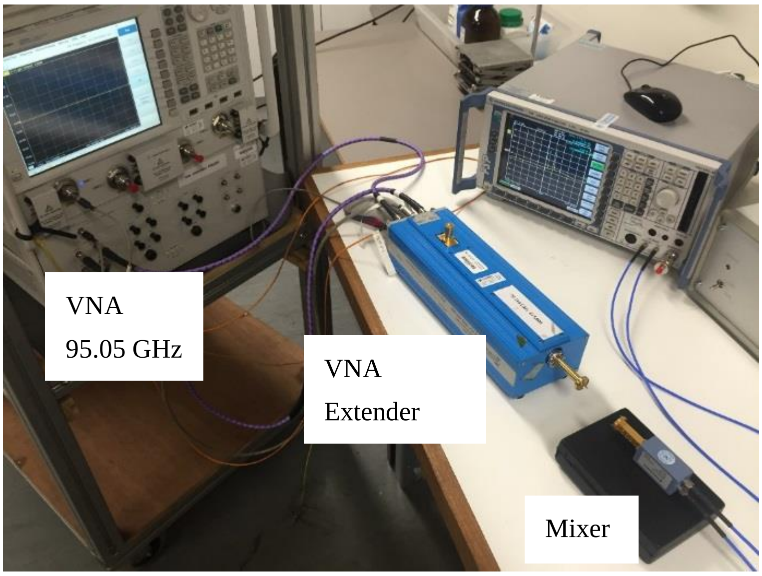

Figure 4.17 Distinguish the image frequency of the mixer by the use of VNA as a 95.05 GHz frequency source.

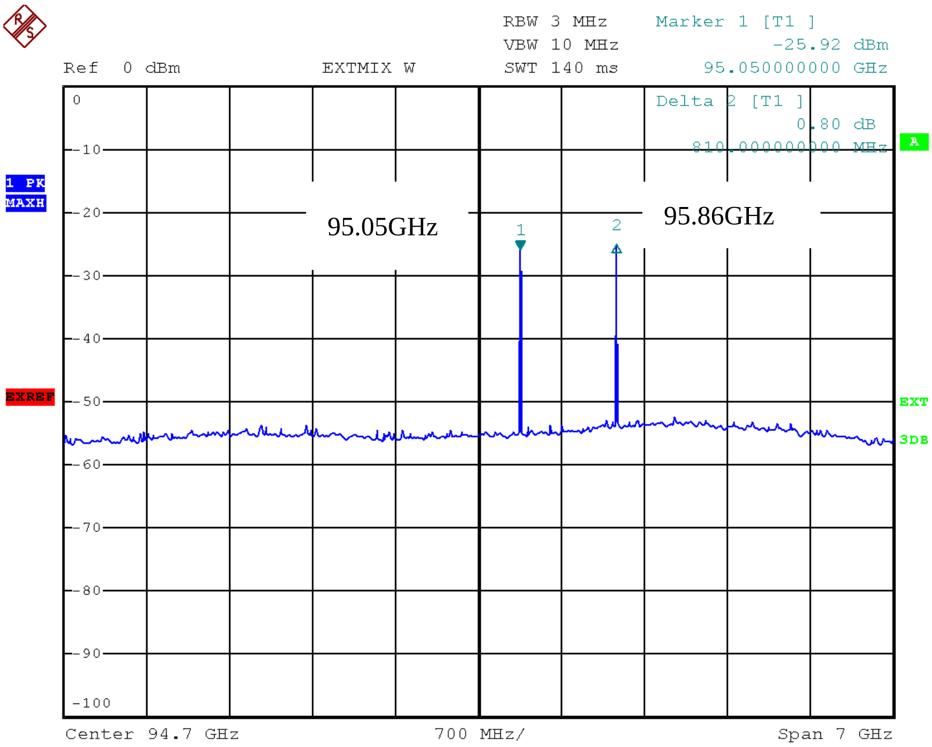

Figure 4.18 Frequency spectrum when 95.05 GHz signal is inputted into the mixer. The image frequency of 95.86 GHz is detected.

4.4.3 Power of output signal

The magnetron output power is measured by Agilent 436A power meter associated with W8486A power sensor. The measurement schematic is shown in Figure 4.19. The W8486A is a diode average power sensor which converts the ac voltage from the microwave source to dc voltage. It measures power levels in a range from -30dBm to +20dBm at frequencies from 75 GHz to 110 GHz. The maximum average power and maximum peak power are 23dBm and 46dBm respectively. As the simulated result of the magnetron peak power is about 6 kW (68dBm), the coupled peak power inputted into the power sensor is about 14dBm which falls in the measurement range of the power sensor.

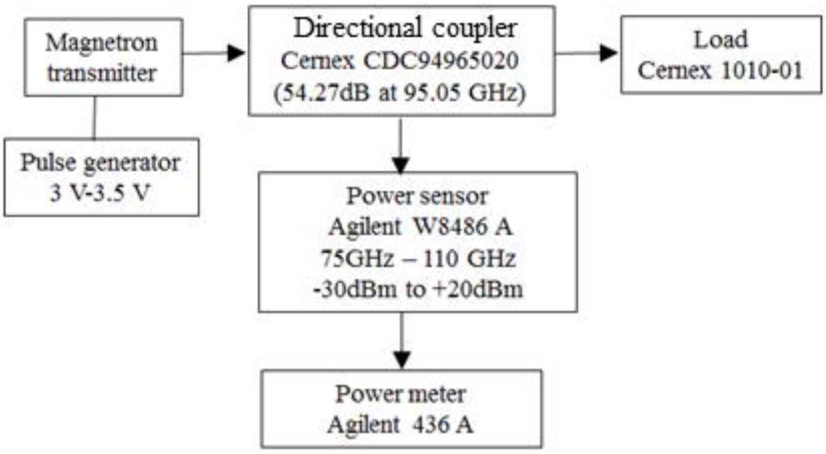

Figure 4.19 Schematic of the power measurement.

The peak power can be calculated by

$$Peak\ power = \frac{Average\ power}{Duty\ cycle} \quad 4.9$$

The average power is measured by the power meter and the duty cycle is measured by the oscilloscope. The measured results when the pulse widths are 50 ns, 100ns, 150ns, and 200 ns when the duty cycle is 0.05% are presented in Table 4-4. The measured peak power is about 5.7 kW which is close to the simulated power of 5.82kW.

Table 4-4 Measured results of the magnetron output power.

Duty cycle, %	Pulse width ns	Pulse Period, us	PRF kHz	Average power dBm/mw	Peak power kW
0.05	50	100	10	34.6/2884	5.76
0.05	100	200	5	34.58/2870	5.74
0.05	150	300	3.33	34.6/2884	5.76
0.05	200	400	2.5	34.55/2851	5.7

4.4.4 Pulse shape

The schematic of the pulse shape measurement is presented in Figure 4.20. The pulse shape is measured by Cernex CFD7511010045 detector which has 15dBm maximum input power, -45dBm tangential signal sensitivity (TSS), and 100mV/mW video sensitivity when it is operated from 75 GHz to 110 GHz. Figure 4.22 shows the measured pulse shapes of the transmitter when the pulse widths are 100ns, 150 ns and 200ns respectively with a duty cycle of 0.05%. The maximum rise time of the pulse is 11ns. The pulse jitter is 5.2 ns when the pulse width is 200ns as shown in Figure 4.23

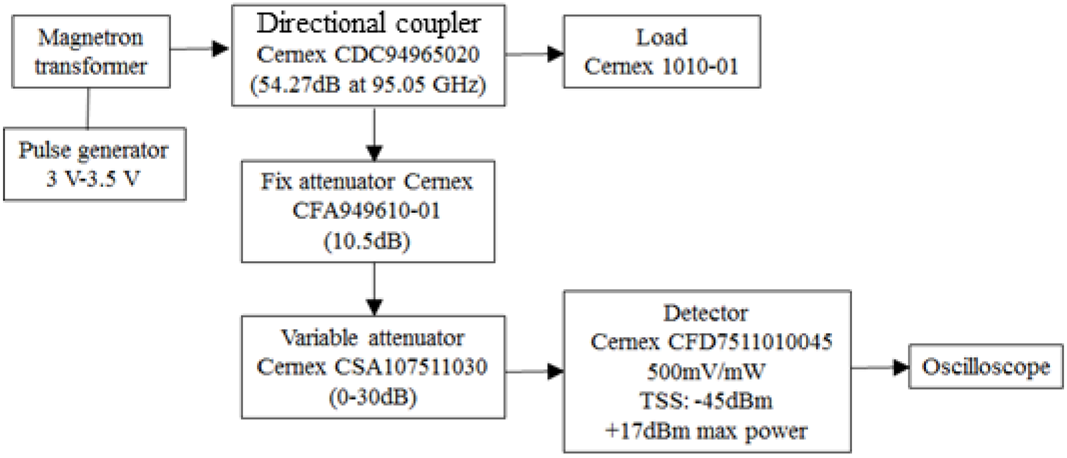

Figure 4.20 Schematic of the pulse shape measurement.

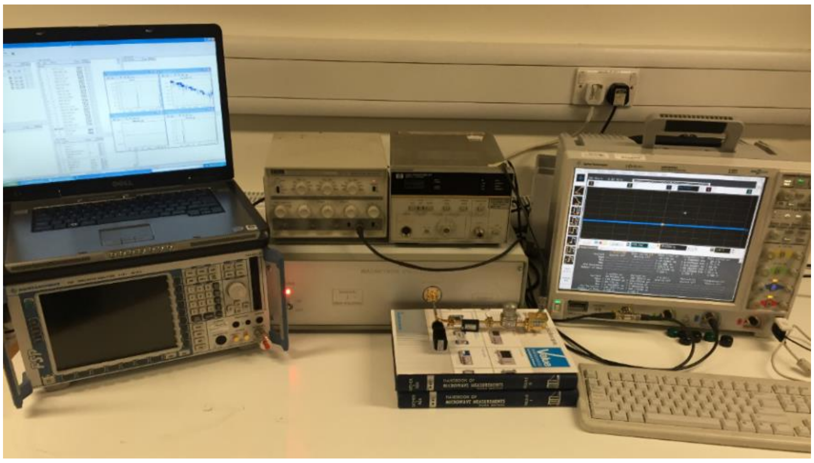

Figure 4.21 Setup of pulse shape measurement.

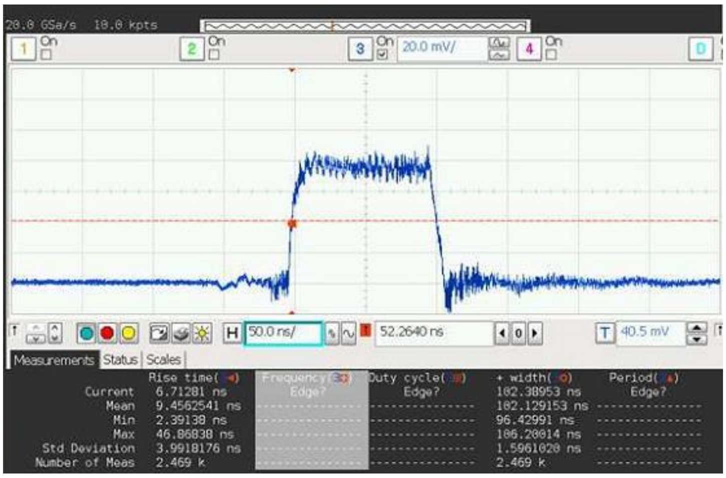

```
                 Rise time(  )   Frequency(  )  Duty cycle(  )   + width(  )      Period(  )
                                     Edge?          Edge?                           Edge?
      Current    6.71281 ns                                      102.38953 ns
         Mean    9.4562541 ns   -------------- --------------   102.129153 ns  --------------
          Min    2.39138 ns     -------------- --------------   96.42991 ns    --------------
          Max    46.86838 ns    -------------- --------------   106.20014 ns   --------------
Std Deviation    3.9918176 ns   -------------- --------------   1.5961020 ns   --------------
Number of Meas   2.469 k        -------------- --------------   2.469 k        --------------
```

(a) Pulse width 100ns; duty cycle 0.05%; rise time 6.7ns; PRF 5 kHz.

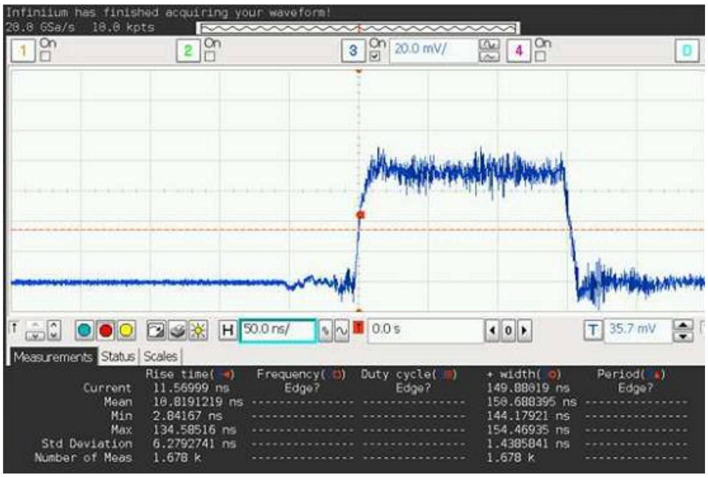

```
                 Rise time(  )   Frequency(  )  Duty cycle(  )   + width(  )      Period(  )
                                     Edge?          Edge?                           Edge?
      Current    11.56999 ns                                     149.88019 ns
         Mean    10.8191219 ns  -------------- --------------   150.688395 ns  --------------
          Min    2.84167 ns     -------------- --------------   144.17921 ns   --------------
          Max    134.58516 ns   -------------- --------------   154.46935 ns   --------------
Std Deviation    6.2792741 ns   -------------- --------------   1.4385841 ns   --------------
Number of Meas   1.678 k        -------------- --------------   1.678 k        --------------
```

(b) Pulse width 150 ns; duty cycle 0.05%; rise time 11ns; PRF 3.3 kHz.

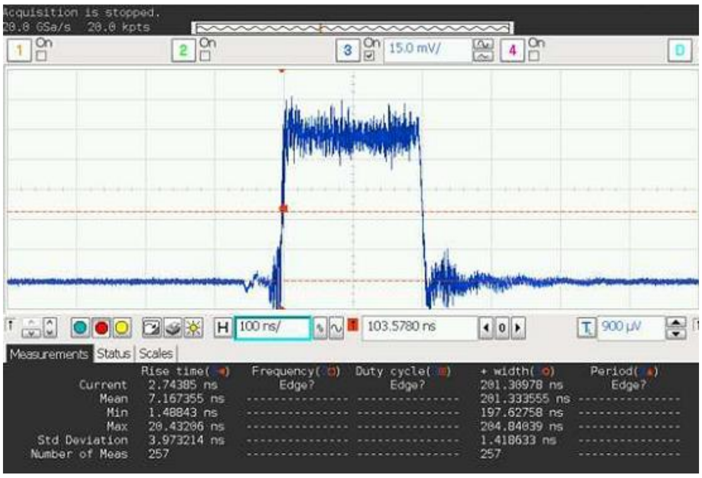

```
                 Rise time(  )  Frequency(  )  Duty cycle(  )  + width(  )     Period(  )
      Current    2.74385 ns         Edge?          Edge?       201.30978 ns       Edge?
         Mean    7.167355 ns   -------------- --------------   201.333555 ns  --------------
          Min    1.48843 ns    -------------- --------------   197.62758 ns   --------------
          Max    20.43206 ns   -------------- --------------   204.84039 ns   --------------
Std Deviation    3.973214 ns   -------------- --------------   1.418633 ns    --------------
Number of Meas   257           -------------- --------------   257            --------------
```

(c) Pulse width 200 ns; duty cycle 0.05%; rise time 2.7 ns; PRF 2.5 kHz.

Figure 4.22 Measurement results of the pulse shapes when pulse widths are (a) 100 ns, (b) 150 ns and (c) 200 ns respectively.

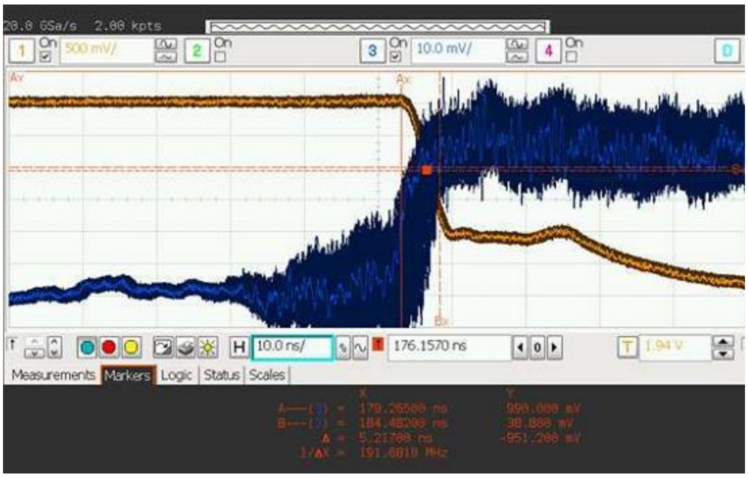

```
                  X                  Y
A----( ) =   179.26500 ns       990.000 mV
B----( ) =   184.48200 ns       38.800 mV
       Δ =   5.21700 ns         -951.200 mV
     1/ΔX =  191.6810 MHz
```

Figure 4.23 5.2 ns pulse jitter with 200ns pulse width and 0.05% duty cycle.

4.5 Summary

A W-band SHM has been investigated by 3-D particle simulation and experimental measurement. As shown in Table 4-5, the simulated results agree very well with the experimental results which confirm the accuracy of the modelling. Based on the considerations of anode temperature and threshold value of the electric field corresponding to vacuum break down, appropriate value for the pulse duration has been estimated. The measurement of the magnetron transmitter demonstrates that this magnetron has lifetime over 5000 hours with more than 5kW output power and high quality transmitting pulses operated at 95.05GHz frequency. It is a promising oscillator for the application of millimetre-wave cloud radar.

Table 4-5 Comparison between the simulation results and measurement results

Parameters	Simulation	Measurement
Anode voltage (kV)	10.5	10.5
Magnetic field (T)	0.83	0.83
Frequency (GHz)	95.21	95.05
Output power (kW)	5.82	5.7
Anode current (A)	10.4	10
Efficiency (%)	5.3	4.9

Chapter 5 THz-band Spatial Harmonic Magnetrons

5.1 Introduction

Most of the THz applications call for compact high-power radiation sources. So far, many kinds of vacuum tubes such as TWTs, Klystrons, Gyrotrons, and Clinotrons have been developed in the low region of THz band up to about 1 THz. However, THz-band magnetrons are rarely reported. Spatial harmonic magnetron with cold secondary emission cathode is an attractive candidate for the development of high-power and low-cost THz oscillators. In this chapter, the properties of the SHMs operating in the low region of THz band are investigated based on numerical simulations and cavity measurement. A SHM operating above 300 GHz is proposed and simulated.

5.2 209 GHz $\pi/2-1$ Mode SHM

5.2.1 Simulation model and cold simulation results

The simulation model of the 209GHz SHM has the same anode diameter (2.6 mm) as the 95GHz SHM as studied in Chapter 4, but to achieve high frequencies, the number of the vanes is increased from 24 to 40. Figure 5.1 shows the simplified simulation model without side cathode, in the x-y, x-z planes. It consists of the following parts: 1) a 40-vane anode block; 2) WR-5 output waveguide; 3) a quarter wavelength slot with 0.1 mm width; 4) platinum cold secondary emission cathode; The material of the anode cavity is copper with 5.8e7 S/m conductivity. The main geometrical parameters are presented in Table 5-4.

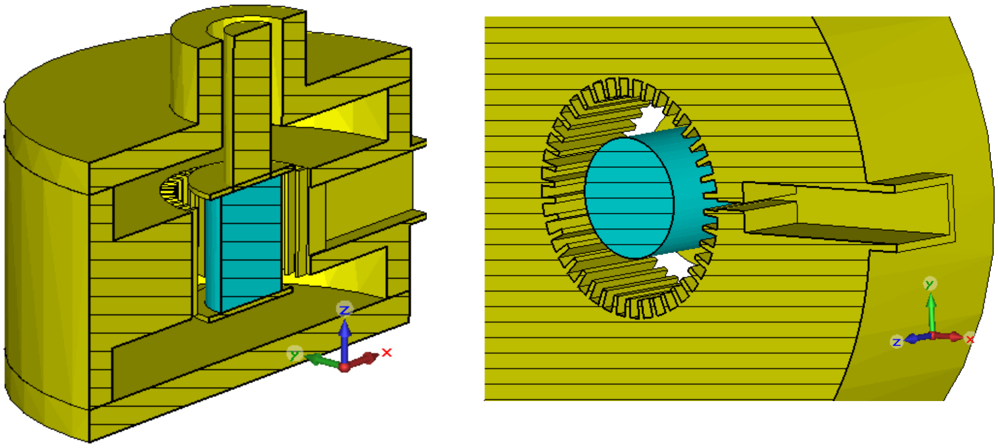

Figure 5.1 Simulation model of a 209 GHz SHM.

Table 5-4 Geometrical parameters of a 209 GHz SHM

Parameter	Value
Number of vanes	40
Anode diameter, mm	2.6
Cathode diameter, mm	1.55
Anode height, mm	2
Side resonator opening	6^{o}
Vane depth, mm	0.242
End space height, mm	0.5
Transformer width, mm	0.1
Transformer length, mm	0.4
Cathode hat radius, mm	1
Output Waveguide	WR5

According to the cold simulation in eigen mode solver, resonant modes and frequencies can be identified from the profiles of the vector electric field. For the $\pi/2-1$ (n=31) mode, the phase difference between the adjacent side resonators is 81^{o}

and the resonant frequency is 210.5 GHz. The neighbouring π/2 mode (n = 30) with 90^o phase shift between the adjacent side resonators is resonant at 217.5 GHz. Their cold cavity vector electric field patterns are presented in Figure 5.2.

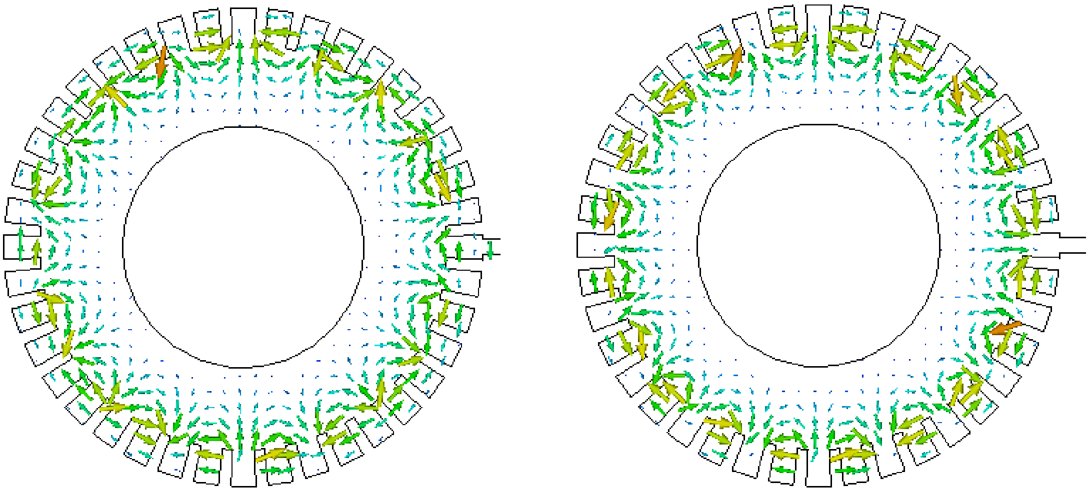

(a) **(b)**

Figure 5.2 Cold simulation results of vector electric field distribution (a) π/2-1 mode (210.5GHz), (b) π/2 mode (217.5GHz).

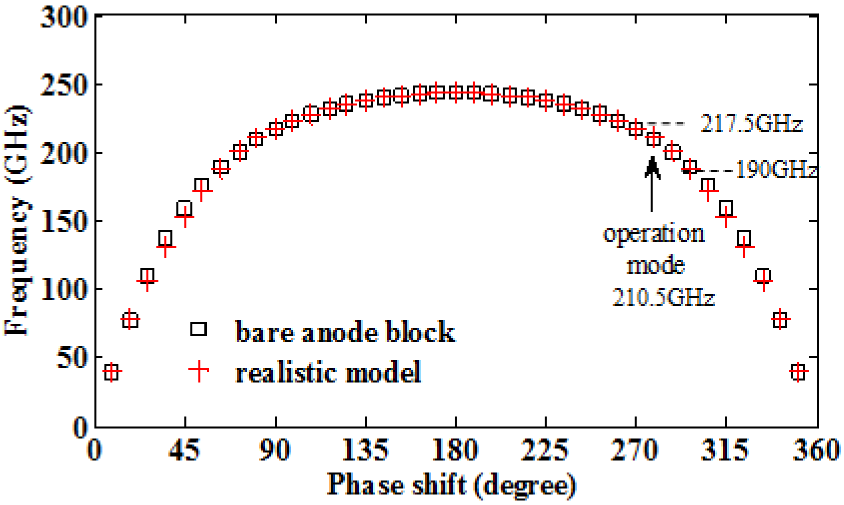

Figure 5.3 Resonant frequencies as a function of phase shift between adjacent vanes for two models: (1) bare anode block (without end space, end caps and output structure) with PMC boundary; (2) anode cavity with output structure as shown in Figure 5.1.

Figure 5.3 shows the dispersion diagram of the bare anode block with PMC boundaries and the anode cavity with output structure. These two dispersion diagrams are close to each other. The slight discrepency is due to the end space and output structure. Comparing with the dispersion diagram of the 35 GHz 16-vane SHM in Figure 3.9, the anode cavity with 40 vanes has a large number of the modes. The mode sperations of the π-mode and π/2-1 mode are 0.08% and 3.3% respectively.

5.2.2 Particle simulation

Figure 5.4 plots the Hull cutoff parabola, Hartree resonant line of the π/2−1-mode and one of the examined operating points (13.6 kV, 0.948 T). The operating point is selected in the region where the Hartree resonant line and the Hull cut-off parabola are close to each other. To trigger the secondary emission, 2A DC seed current is specified on the cold cathode surface. When 13.6kV anode voltage and 0.948T magnetic field are applied, the electron cloud initially forms in the area near the emission points assumed on the cathode (see Figure 5.5) and then expands until it fills the whole interaction space. Figure 5.6 depicts the time evolution of the space charge. In the beginning, before 2ns, the secondary emission current is very low (see Figure 5.6 (a) and Figure 5.7) and most of the space charges come from the primary electrons. During this stage the space charge is uniformly distributed as shown in Figure 5.6 (b).

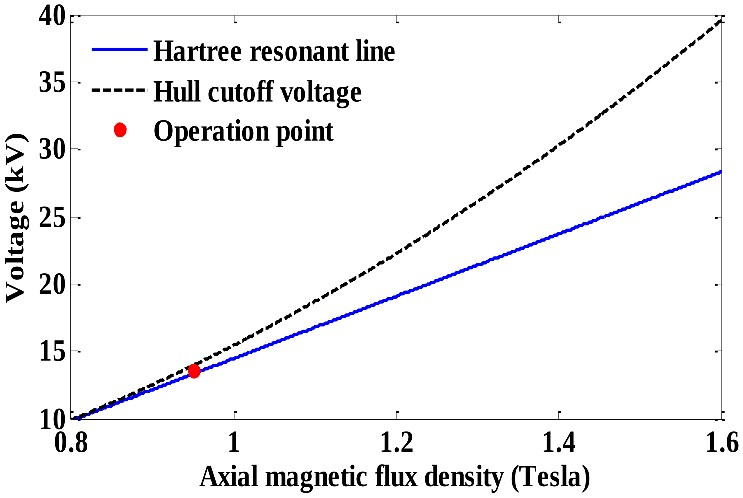

Figure 5.4 Hull cut-off parabola, Hartree resonant line and operation point (13.6kV, 0.948 T).

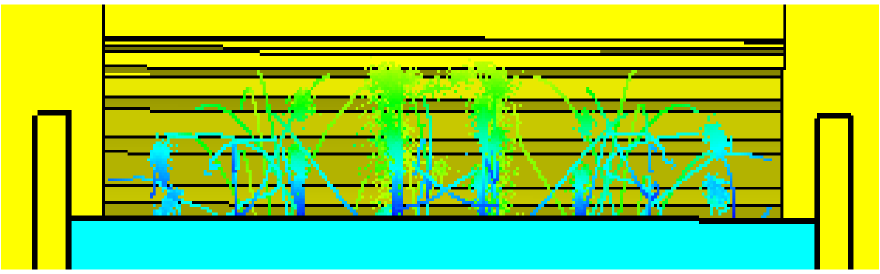

Figure 5.5 2 A seed current emitted from the emission points specified on the surface of the cold cathode.

After 3ns, there is an avalanche increase of the secondary emission current, which results in the destruction of the uniform space charge pre-exsited. As shown in Figure 5.6(d), When the oscillation is stable after 5 ns, 31 electron bunches appare near the anode surface. As it is known, the number of spokes is equal to the number of complete periods (k=m+nN) of the synchronous harmonic along the anode circumference. Thus, for this 40-vane SHM (N=40), the formation of 31 electron spokes confirms the synchronism between the first backward harmonic (m= −1) of the π/2 – 1 mode (n=9) and the space charge.

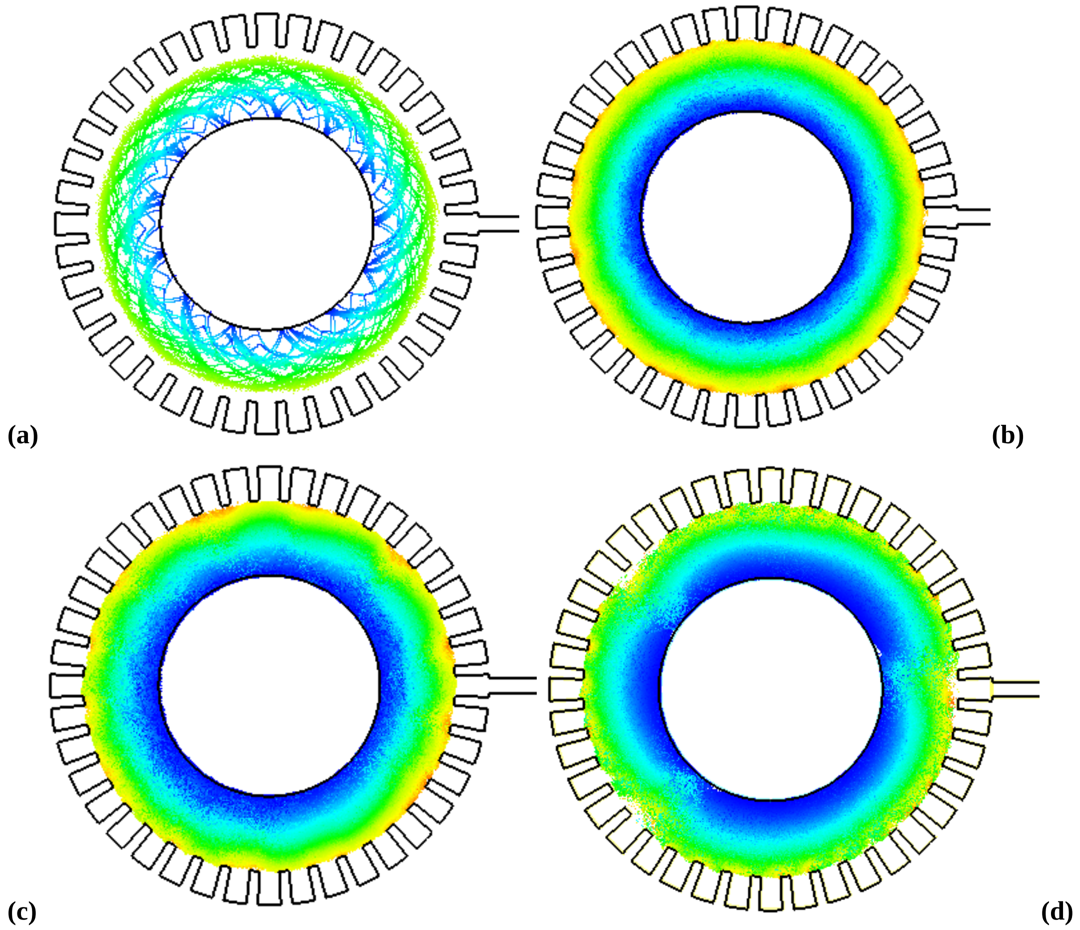

Figure 5.6 Time-evolved spoke formation plotted in the x-y plane at (a) 0.2 ns, (b) 2 ns, (c) 3 ns, and (d) 5 ns. The charge profiles are plotted for 13.6 kV, 0.948 T, when 2 A DC current is specified on the cathode surface.

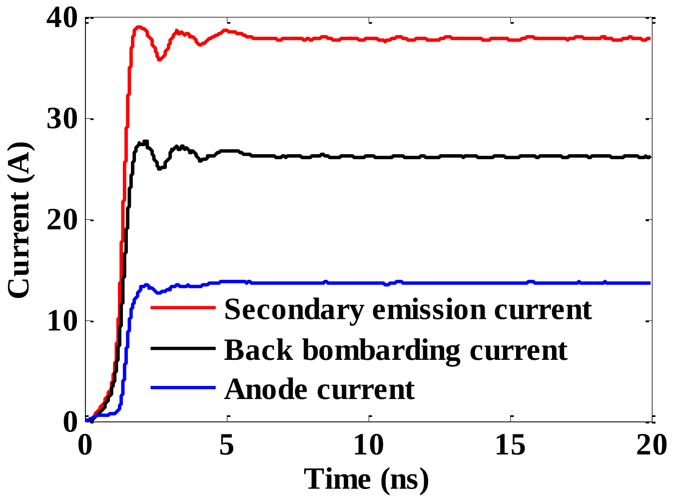

Figure 5.7 Secondary emission current, back bombarding current, and anode current for 13.6 kV, 0.948 T.

Figure 5.7 presents the time evolution of the secondary emission current, back bombarding current, and anode current. At the steady state, there is 37.73A secondary emission current gerated by 26.1A back bombarding current. The corresponding secondary coefficient is 1.45. The secondary emission current is around 19 times of the primary seed current. Thus, the main cathode emission current comes from the secondary emission.

This state is referred to as secondary-emission-dominated state [73]. As shown in Figure 5.6(d), in this state, a more turbulent space charge results in more energy exchange between the particles [61]. There are three regions with low charge density ("voids") propagating through the bottom of the space charge, which modulates the electron density entering the electron bunches and a part of electrons are not synchronous with the operating mode.

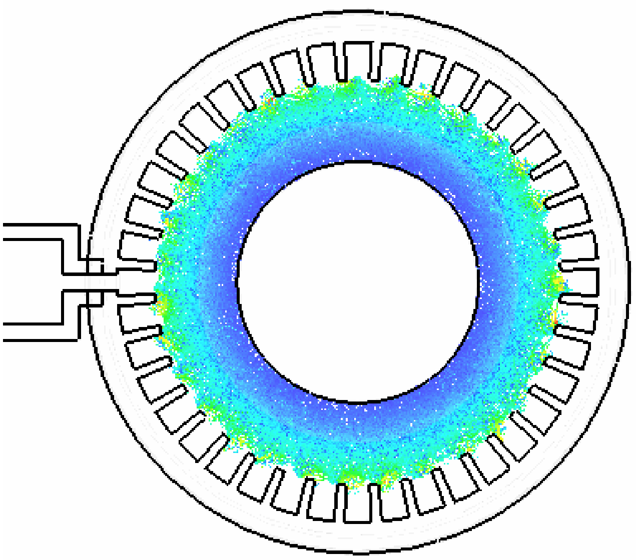

Figure 5.8 Space charge distribution at the steady state of the oscillation of a DC emission model with 40A cathode current.

For the comparison purpose, the magnetron is investigated with DC emission cathode instead of secondary emission cathode. A constant 40A current, which is close to the total cathode current in the secondary emission model, is specified in the DC emission model. Figure 5.8 shows that the space charge distribution is quite regularly. There are many layers in the electron sheath and the electrons distribute uniformly in each layer with low fluctuation. This state is referred to as primary-emission-dominated state. Therefore, it is deduced that the electron secondary emission is the main reason of the irregular space charge distribution and strong fluctuation.

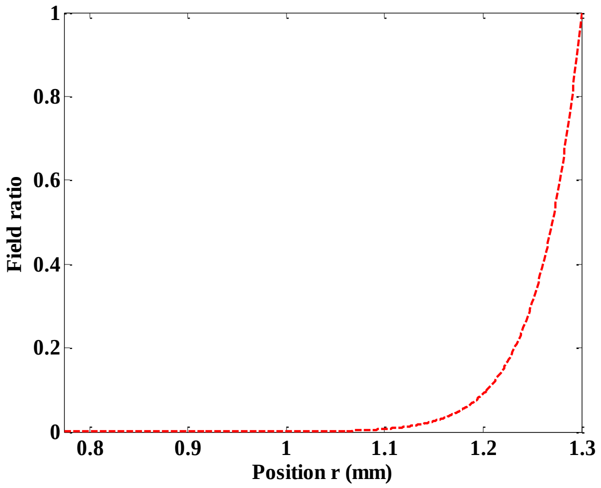

Figure 5.9 The normalized amplitude of π/2 – 1 mode of -1th spatial harmonic in the inter action space (anode surface r=1.3; cathode surface r=0.7).

Figure 5.9 shows the e-field amplitude of the π/2 –1 mode of -1th spatial harmonic in the interaction space normalized by the field at the anode surface, according to the following distribution law [74]

$$U_r = U_a(\frac{r}{r_a})^k \qquad 5.1$$

where U_r is the e-field amplitude at the position r; U_a is the e-field amplitude near the anode surface; $k = |n + mN|$.

Cathode surface is at *r*=0.7 mm and anode surface is at *r*=1.3 mm. One can see that the amplitude of the electric field decreases exponentially at the locations far away from the anode surface. An increase of the number of resonators N results in a concentration of the electric field in a thin layer near the anode surface. The amplitude of electric field reduces to about 90% at the position r=1.2 which is 0.1 mm away from the anode surface. Therefore, in order to realize an efficient electron-wave interaction, the electrons have to move closer to the anode surface. This is the reason why the operation points should be selected close to its critical value determined by the Hull cut off parabola. This is also the main reason why the electron bunches are in a thin layer near the anode surface as shown in Figure 5.6 (d) and Figure 5.8. The surface wave operation leads to an increase of the leakage current and a decrease of the efficiency.

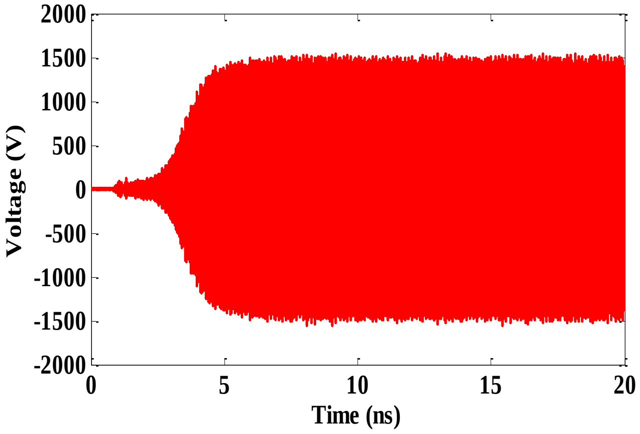

Figure 5.10 Output voltage amplitude measured at the centre line of the output waveguide broad walls for V_{dc}= 13.6 kV and B = 0.948 T.

Figure 5.10 shows the time evolution of the output voltage of the secondary emission model. The output voltage grows rapidly at about 3ns and reaches its saturation value $V_{out} = 1500\,V$ after 5ns. Considering the dimensions of the WR-5 waveguide (a=1.295 mm,b=0.648mm) and 115.7 GHz cutoff frequency, the calculated output power of this model is 2.48kW. The oscillation frequency is 209 GHz as shown in Figure 5.11, which is around 1.5 GHz lower than π/2-1 mode cold cavity frequency due to the effect of the space charge. At the steady state of the oscillation, around 13.5 A current is collected on the anode surface.

The magnetron is investigated with various values of anode voltage and magnetic field. Figure 5.12 presents the the output voltage profiles when the anode voltages are 13.5 kV, 13.6 kV, and 13.7 kV and magnetic field keeps constant at 0.948 T. Figure 5.13 shows the output voltage profiles when the magnetic field is varied from 0.944T to 0.956T with 13.6kV anode voltage. The simulation results are summarized in Table 5-1.

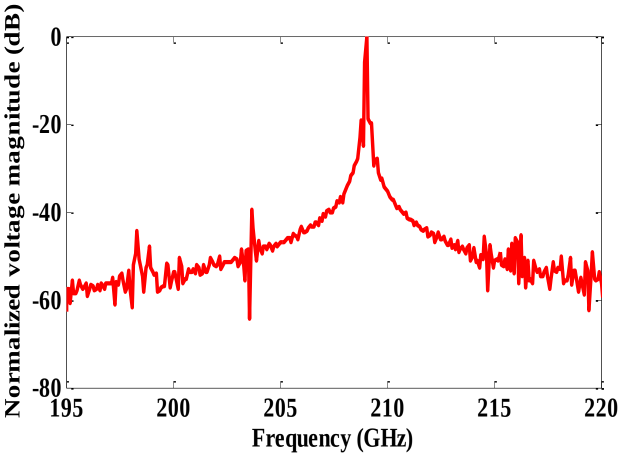

Figure 5.11 Normalized amplitude of the output frequency in dB.

Table 5-1 Simulation results performed with various operation points

B, T	V_{dc}, kV	I_a, A	P_{out}, kW	η	f, GHz
0.948	13.5	10	1.39	1.02%	209
0.948	13.6	13.6	2.48	1.34%	209
0.948	13.7	14.7	3.19	1.58%	209
0.944	13.6	15	2.8	1.37%	209
0.952	13.6	8.8	1.26	1.05%	209
0.956	13.6	7.8	1.1	1.03%	209

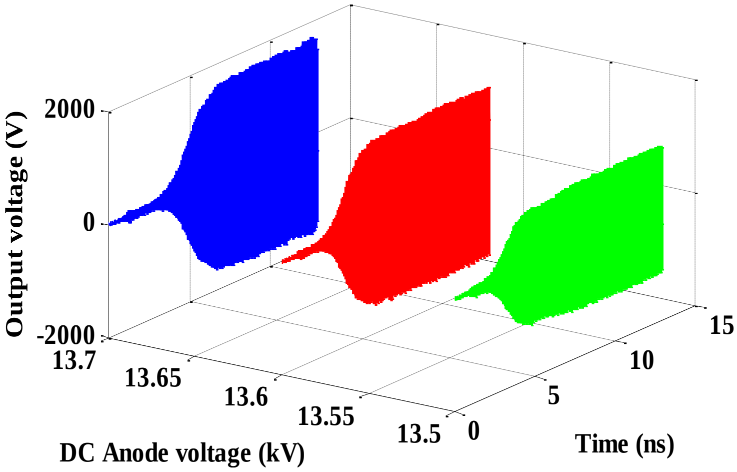

Figure 5.12 The output voltages when anode voltages are 13.5kV, 13.6kV, and 13.7 kV with 0.948T magnetic field.

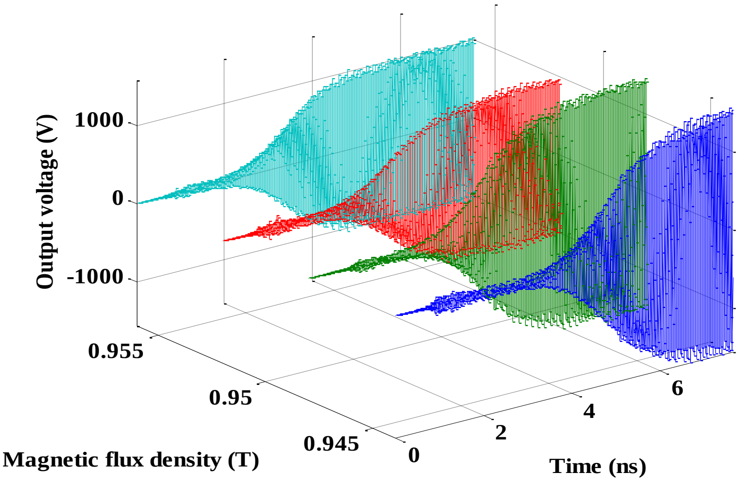

Figure 5.13 The output voltages for B = 0.944T, 0.948T, 0.952T, 0.956T and V_{dc}=13.6kV anode voltage.

5.2.3 Anode cavity fabrication and measurement

5.2.3.1 Anode cavity fabrication

The anode cavity is fabricated by the use of 0.05mm diameter Wire Electric Discharge Machining (WEDM, also named wire cutting). The photograph of the fabricated anode cavity is shown in Figure 5.14.

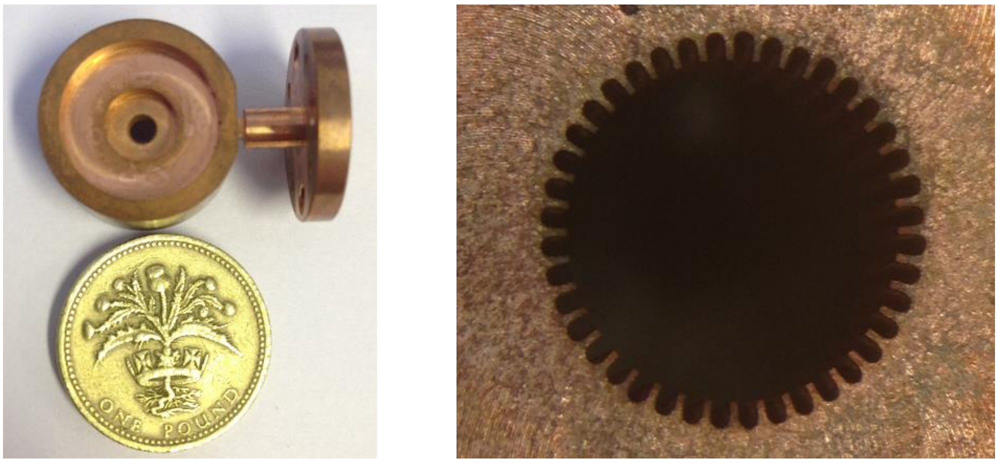

(a) **(b)**

Figure 5.14 (a) The photograph of a 40-vane anode cavity; (b) the zoomed view of anode block.

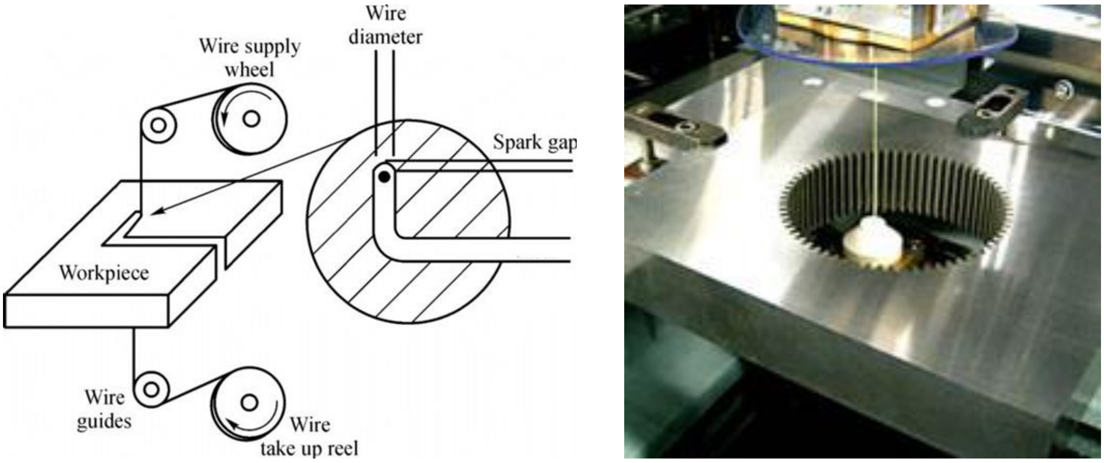

Figure 5.15 Schematic of the wire cutting.

Wire cutting is a type of micro EDM which is quite affordable for the magnetron cavity fabrication. As sketched in Figure 5.15, in the wire cutting process, the wire and the work piece are two electrodes with high voltage. Here, the work piece is oxygen-free copper. The large electric field arcs across the gap between the wire and the workpiece raises the local surface temperature to between 8000°C and 12,000°C and melts a roughly hemispherical volume on the workpiece. Therefore, as shown in Figure 5.14 (b), the bottoms of side resonators are rounded rather than being sharply cornered in the simulation model in Figure 5.1.

The wire is held in tension between a feed spool and a take-up spool and is continually fed through the cutting area. In this way, the cutting surface is continually replenished eliminating the need to regularly replace the wire. The wire is usually supported in a fixed position in the machine, but the workpiece can be translated and rotated in three dimensions around the wire enabling some fairly complicated shapes to be cut with a single straight edge. Both the wire and the workpiece are immersed in a dielectric fluid (usually deionized water). The arc vaporizes the dielectric locally, and the implosion of the vapor bubble helps to pull material from the molten crater on the metal surface. The flow of dielectric fluid then cools and flushes the removed material from the area. Normal range of the EDM wire diameter is from 0.3mm to 0.03mm.

5.2.3.2 Anode cavity measurement

The anode cavity is measured by R&S Vector Network Analyser (VNA) associated with ZVA-Z220 millimetre-wave converter in the frequency range of 140GHz-220GHz. There are two curves in Figure 5.16. One is the simulated S11 of the simulation model in Figure 5.1 without considering fabrication tolerance; the other is the measured S11 of the fabricated anode cavity. The simulated resonance frequency of S11 is 210.1 GHz which is very close to the $\pi/2-1$ mode frequency in the cold cavity simulation. However, there are two resonant frequencies of the measured S11: 208.1 GHz and 216.7 GHz.

To investigate the influence of the fabrication tolerance, the simulation model is modified by side resonators with rounded bottoms as shown in Figure 5.17, where r is the radius of the corner. The simulations indicate that the rounded bottoms of the side resonators result in the resonant frequencies increased. Therefore, it could confirm that the π/2−1 mode frequency of the fabricated anode cavity is 216.7GHz which has 6GHz frequency shift due to the fabrication tolerance. Simulation results shows that the radius of the rounded corner *r* is around 0.06mm. On the other hand, the vane of side resonator is 0.068mm width which is too thin to be fabricated. The vanes can be bended or cracked during the fabrication process. Therefore, it is needed to optimize the anode cavity with the consideration of the practical fabrication.

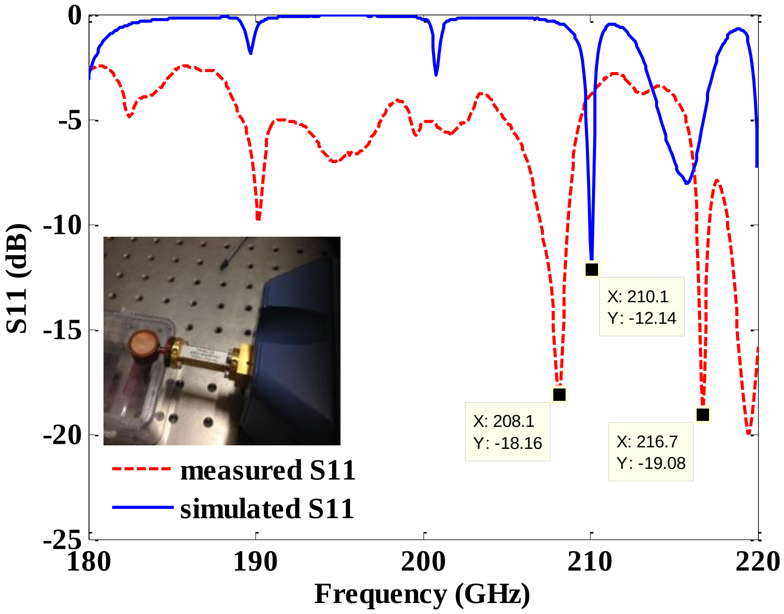

Figure 5.16 Simulated S11 of the model with sharply cornered side resonators and the measured S11 of the fabricated anode cavity with rounded corner side resonators.

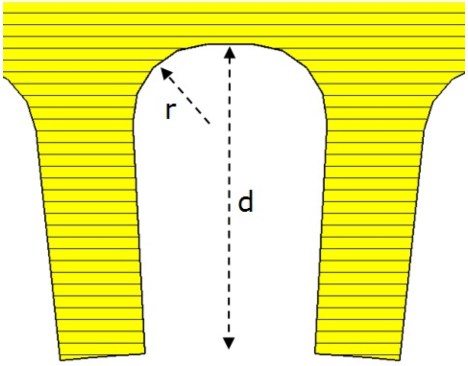

Figure 5.17 The side resonator with rounded bottoms. r: bottom radius; d: vane depth.

5.2.4 Anode cavity optimization

To keep the resonant frequency at around 209 GHz, the anode cavity is optimized by increasing the vane depth d from 0.234mm to 0.248mm. The radius of the bottom corner r is 0.06mm. To make the vanes thicker, the resonator opening reduces from 6^o to 5.9^o. The geometry dimensions are presented in Table 5-2. Other geometrical parameters are the same as the model in Figure 5.1. This optimized model requires much more mesh cells due to the tiny rounded corner, which results in the requirement of relatively large computer source and long simulation time. It takes around 105 hours for 5 ns simulation time for the particle simulation by the use of a quad-core Intel 3.2-GHz processor.

Table 5-2 Optimized geometries of the anode side resonators

Side resonator	Before optimization	After optimization
	Sharped	Rounded (r=0.06mm)
opening angle	6^o	5.9^o
Vane depth, mm	0.234	0.248

Figure 5.18 shows the profile of the time-varying output voltage monitored at the centre line of the output waveguide broad walls, when the operating point is 13.6 kV, 0.948 T. The oscillation is stable after 3 ns with 1100V output voltage. The calculated output power is 1.3 kW which is 1.18kW lower than the model without the consideration of the fabrication tolerance. The corresponding oscillation frequency is 208.7GHz as shown in Figure 5.19. The space charge distribution at the steady state is presented in Figure 5.20.

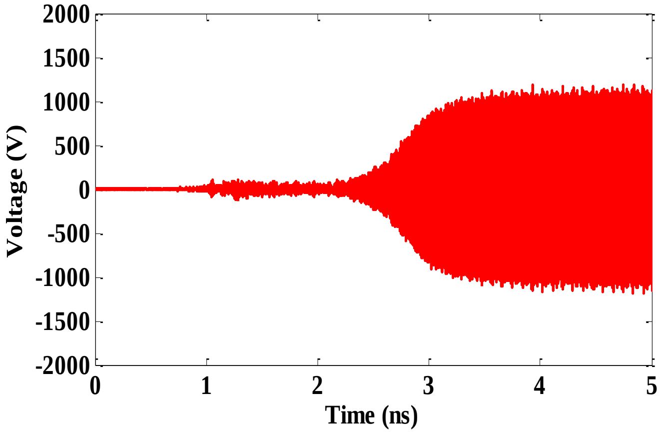

Figure 5.18 Output voltage amplitude measured at the centre line of the output waveguide broad walls for V_{dc}= 13.6 kV and B = 0.948 T.

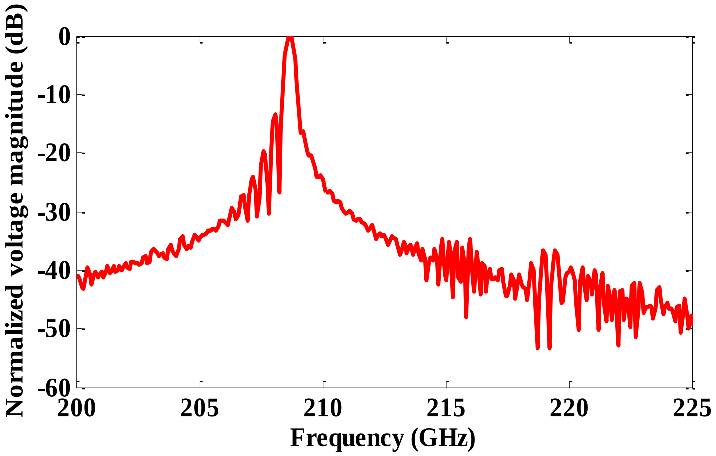

Figure 5.19 Normalized amplitude of the output frequency in dB.

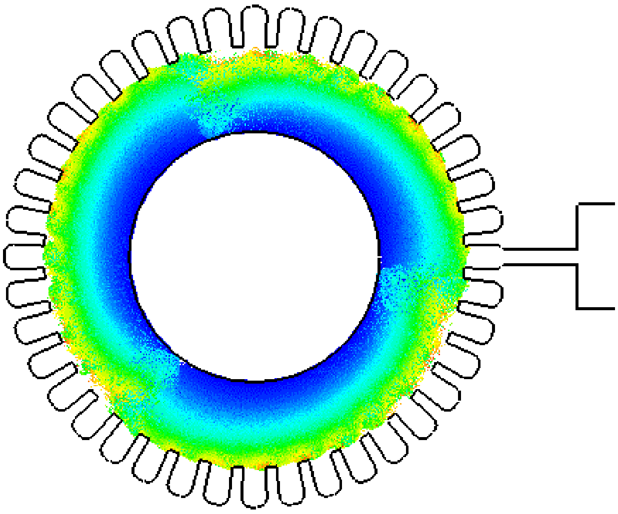

Figure 5.20 Space charge distribution at the steady state of 5 ns.

Figure 5.21 The photograph of the 210GHz magnetron (150mm*75mm*75mm, 1.3kg) [75].

The magnetron is developed in IRA NASU, Ukraine, as shown in Figure 5.21 [75]. The magnetron is operated with pulse duration of 50ns and duty factor of 0.01%. A low-power thermionic cathode producing a current of about 100 mA was used as the auxiliary cathode to initiate the secondary emission from the cold cathode. The magnetron is operated at a frequency of 208.8 GHz with an output peak power of about 1.1 kW and an average power of about 0.11 W. Its weight is 1.3 kg with dimensions of 150 mm × 75 mm × 75 mm. The measurement results are presented in Table 5-3. Comparing the simulation and experimental results, there is a good agreement between them.

Table 5-3 Simulation results and experimental results

	Simulation results	Experiment results [75]
Anode voltage V_{dc}, kV	13.6	14.6
Magnetic field B, T	0.948	0.94
Frequency f, GHz	208.7	208.8
Output power P_{out}, W	1336	1099
Anode curent I_a, A	10.2	20
Secondary emission current I_s, A	31	--
Efficienty η, %	0.96	0.4

Thus, according to particle simulation and experimental experiment, one could conclude that the fabrication tolerance should not be neglected during the design of the THz SHM, since there is a significant influence on the magnetron performance.

5.3 300 GHz π/2−3 Mode SHM

Following the study on the 209 GHz SHM in the previous section, this section presents a spatial harmonic magnetron model above 300GHz. The geometrical parameters are shown in Table 5-4. The magnetron is operated on the π/2−3 mode of -1th spatial harmonic. These parameters have been selected to be close to those of a 318 GHz π/2-2 mode simulation model previously reported in [76] which was proposed by using of an in-house developed 2D PIC code. These parameters are selected in a way that they can provide maximum output power for the π/2-3 mode with a resonant frequency about 300 GHz.

Table 5-4 Geometrical parameters of a 300GHz magnetron simulation model

Number of vanes, N	44
Cathode diameter, mm	1.2
Anode diameter, mm	2
Side resonator depth, mm	0.135
Side resonator opening angle	5.7^o
Vane thickness	0.043
Vane gap, mm	0.1
Anode height, mm	2
Output waveguide	WR 3
Copper conductivity, S/m	5.8e7 S/m
The height of the end space, mm	0.25
Transformer length, mm	0.2
Transformer width, mm	0.05

When the number of the side resonators is increased to 44, the RF field moves much closer to the anode surface. As shown in Figure 5.22, the amplitude of the electric field reduces 50% when 0.02 mm away from the anode surface and almost vanishes at the position 0.1 mm away (r=0.9) from the anode surface.

The approximate analysis of the beam-wave interaction in the SHM reveals that among the RF components, the electron trajectories and power generation in the SHM with large number of resonators depend on the synchronous harmonic of the angular electric field $E_{\emptyset}$ near the anode surface [77].

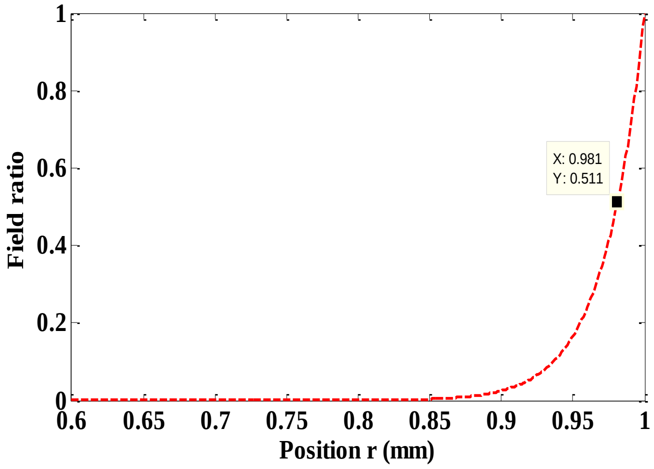

Figure 5.22 The normalized amplitude of the -1th spatial harmonic of π/2 – 3 mode in the interaction space (anode surface r=1; cathode surface r=0.6)

E_{φ} near the anode surface is written as [77]

$$E_{\varphi}(\varphi)=\sum_{m=-\infty}^{\infty}a_m e^{jk_m\varphi} \quad 5.2$$

$$a_m=\frac{N}{\pi}\frac{sin(k_m\theta)}{k_m} \quad 5.3$$

$k_m=mN+n$, m= …, -1, 0, 1, ...; $n=1,2,\dots,\ N/2$

where N and 2θ are the number of side resonators and resonator's opening angle, respectively, m is the order of spatial harmonic and n is the mode number. a_{-1} is referred to as the amplitude of the -1th spatial harmonic, respectively.

In this model, N=44, m=-1, n= 8, thus k_{-1}=36. To get the maximum amplitude of the –1th spatial harmonic, the resonator opening 2θ is close to 5^{o}. According to the cold cavity simulation, to increase the frequency of the π/2-3 mode to 300 GHz, the vane depth is about 0.137 mm.

As the RF field is in a thin layer near the anode surface, the electron cyclotron radius is comparable with the dimension of the interaction space and on one or two turns the electron is exposed to the region of RF-field. With the electron drift-like motion and the orbital-like motion taken into account, the electron-wave synchronization is determined by drift-orbital resonance condition expressed as follows [78]

$$U_a = U_0\left[\left(\frac{B}{B_0}\right)^2 - \left(\frac{1-\frac{B}{B_0}}{1+2m/k}\right)^2\right] \tag{5.4}$$

$$U_0 = (1-\sigma^2)\left(\frac{m_e}{e}\right)\left(\frac{r_a^2\omega^2}{2k^2}\right) \tag{5.5}$$

$$B_0 = \frac{2\omega m_e}{ek} \tag{5.6}$$

$$\sigma = \frac{r_c}{r_a} \tag{5.7}$$

Where B is the external magnetic field, ω is the angular oscillation frequency, k is the number of RF field variations along the anode perimeter, and m is the number of spatial harmonic. The drift-orbital resonance condition, Hull cut off condition and Hartree resonance voltage are plotted in Figure 5.23.

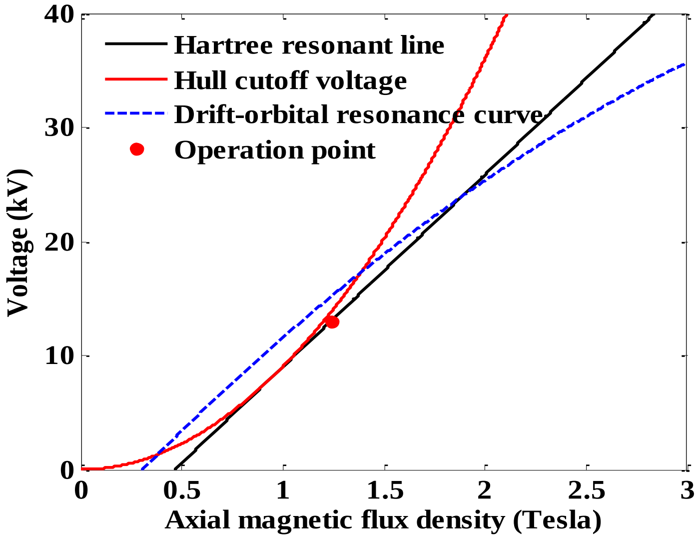

Figure 5.23 Hull cut off parabola, Hartree resonant voltage, drift orbital resonance curve and operation point of the 300 GHz π/2-3 mode SHM.

As the magnetic field of the π/2-2 mode SHM is around 1.25T [76], the magnetic field of the π/2-3 mode should be smaller than 1.25 T. Therefore, the operation points are in the region 1.1T-1.25T, and the anode voltage is in the range of 12kV-14kV. Comprehensive simulations have been carried out to find an optimal combination of the magnetron dimensions and the values of the anode voltage and the dc magnetic field. The obtained vane depth and resonator opening are 0.135 mm and 5.7^{o} respectively. Figure 5.24 shows the cold simulation results of the E-field patterns of π/2 mode (351.1 GHz), π/2-1 mode (337.8 GHz), π/2-2 mode (321.5 GHz) and π/2-3 mode (303.3 GHz). The mode separation of π/2-3 mode is 6%, while that of the π/2-2 mode is 5%.

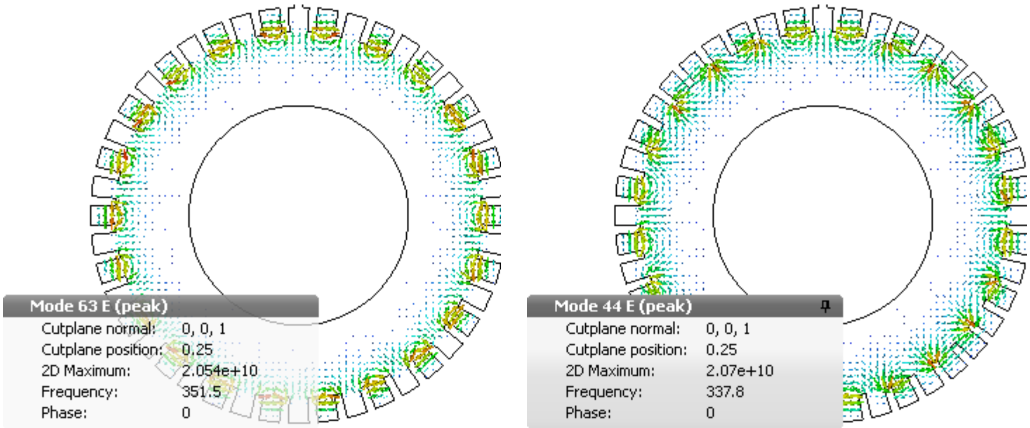

Mode 63 E (peak)
Cutplane normal: 0, 0, 1
Cutplane position: 0.25
2D Maximum: 2.054e+10
Frequency: 351.5
Phase: 0

Mode 44 E (peak)
Cutplane normal: 0, 0, 1
Cutplane position: 0.25
2D Maximum: 2.07e+10
Frequency: 337.8
Phase: 0

(a) π/2 mode 351.1 GHz **(b) π/2-1 mode 337.8 GHz**

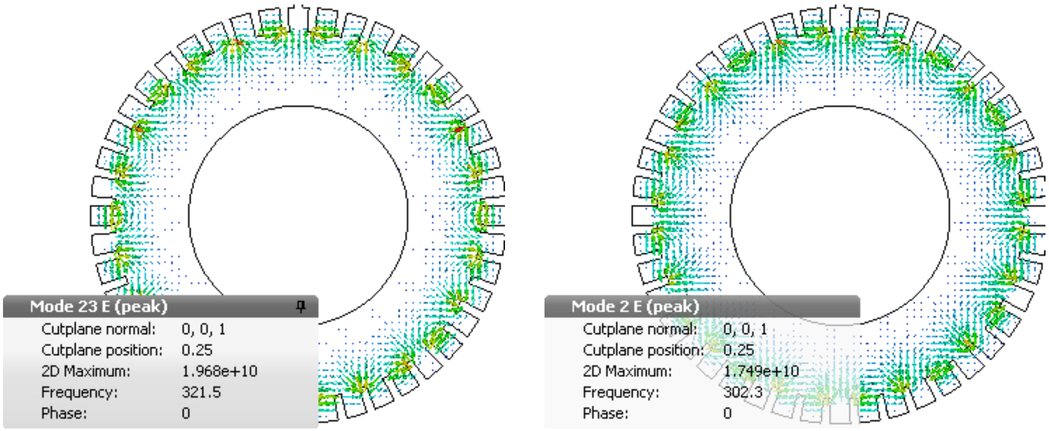

Mode 23 E (peak)
Cutplane normal: 0, 0, 1
Cutplane position: 0.25
2D Maximum: 1.968e+10
Frequency: 321.5
Phase: 0

Mode 2 E (peak)
Cutplane normal: 0, 0, 1
Cutplane position: 0.25
2D Maximum: 1.749e+10
Frequency: 302.3
Phase: 0

(c) π/2-2 mode 321.5 GHz **(d) π/2-3 mode 302.3 GHz**

Figure 5.24 Cold simulation results of electric field patterns of different modes.

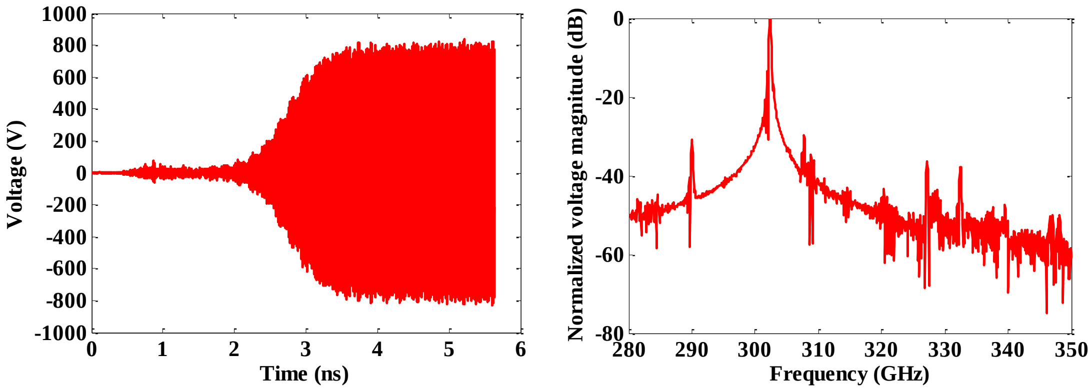

(a) **(b)**

Figure 5.25 (a) Output voltage amplitude measured at the centre line of the output port across the output waveguide broad walls; (b) normalized amplitude of the frequency spectrum obtained from a Fourier transform of the time-varying output voltage. The results are for V_{dc}= 12.9 kV, B = 1.24 T.

There is 2A DC seed current specified on the cathode surface. When 13 kV anode voltage and 1.24 T magnetic field are applied, there are around 36 A secondary emission current generated by 600 eV back bombarding energy at the steady state, Figure 5.25 (a) shows the output voltage amplitude measured at the centre line of the output port across the output waveguide broad walls. The output voltage reaches its saturation value of 800 V after 4 ns. Considering the WR 3 waveguide a = 0.864 mm, b = 0.432 mm, and the cut off frequency of 173.57 GHz, the calculated output power is 695 W. The anode current is 8A with calculated efficiency of 0.67%. As shown in Figure 5.25 (b), the oscillation frequency is 301.4 GHz which is close to the cold cavity frequency of the π/2-3 mode (302.3 GHz). The simulation results are summarized in Table 5-5.

The electron cloud initially forms in the area near the emission points and electron bunches appear after 4 ns. There should be 36 electron spokes when electrons interact with π/2-3 mode of -1th spatial harmonic. However, the number of the electron bunches cannot be distinguished due to the non-periodical distribution in a thin layer near the anode as shown in Figure 5.27 and Figure 5.27.

Table 5-5 Simulation results of a 44-vane π/2-3 mode SHM

Anode voltage, kV	12.9
Magnetic field, T	1.24
Anode current, A	8
Trigger current, A	2
Secondary emission current, A	36
Back bombarding current, A	27
Output power, W	695
Efficiency, %	0.67
Cold cavity frequency, GHz	303.3
External quality factor Q_{ext}	674
Unloaded quality factor Q_o	847
Loaded quality factor Q_L	375.3

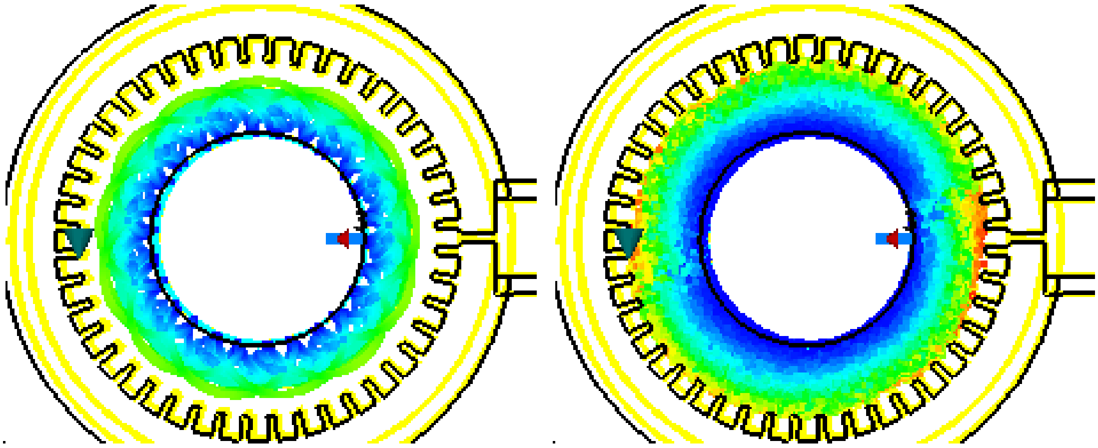

(a) (b)

Figure 5.26 Time-evolved spoke formation plotted in the x-y plane at (a) 1ns and (b) 5ns.

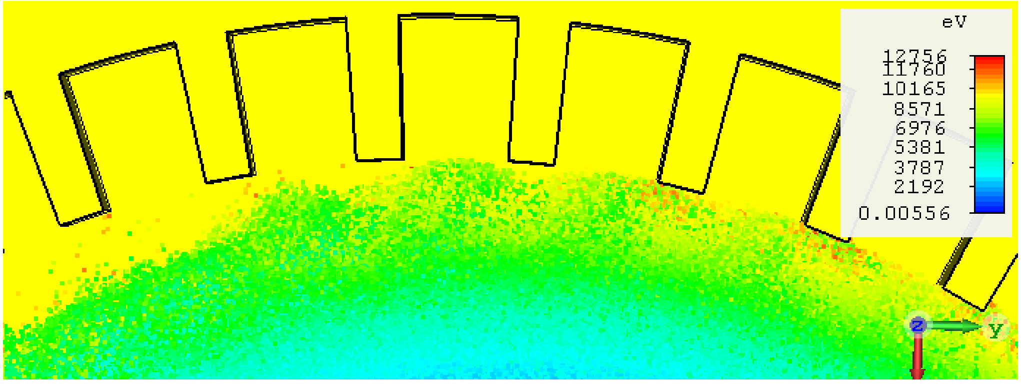

Figure 5.27 Zoomed view of Figure 5.26 (b).

5.4 Summary

In this chapter, the PIC simulations of a 209 GHz SHM shows that when magnetron depends on the primary emission dominated state, the space charge has low internal fluctuation and distributes regularly. When the magnetron depends on the secondary emission dominated state, there is a disturbance in the form of voids traveling through the space charge which causes the space charge irregular.

According to the fabrication and measurement of the anode cavity and the optimization of the simulation model of a 209GHz SHM, it indicates that the fabrication tolerance should be taken into account in the design of the high frequency SHM. Compared with millimetre-wave band SHM, the efficiency of the THz-band SHMs with a large number of vanes is much lower due to the surface wave in the anode slow wave structure.

The simulation model of a SHM above 300 GHz is proposed. The simulation results show that such magnetrons can produce at least 0.6 kW output power.

Chapter 6 Conclusions and Future Work

6.1 Conclusions

In this thesis, considerable insights into the characteristics of the spatial harmonic magnetron have been gained through 3D particle simulation and experimental measurement. The following are the obtained knowledge and key contributions in this work.

1. The effect of the injection current from the side cathode and a fast spatial harmonic magnetron model.

It is found that the cathode current depends on the secondary emission electrons. The injection current from the side cathode is just to provide accumulating electrons near the cathode to initiate the electron secondary emission on the cold cathode and does not affect the spatial harmonic magnetron performance. Thus, a fast SHM model without side cathode has been developed.

2. The dominate roles of the electron back bombardment and secondary emission in SHMs.

The particle simulations on several SHMs have shown that the electron back bombarding energy is substantial, in the range of 300eV-500eV. The electron secondary emission coefficient is dependent on the back bombarding energy. This energy in turn triggers electron secondary emission, which plays an important role in the SHM operation. The threshold value of the secondary emission coefficient for the stable operation of SHM is around 80% of platinum (1.44). Below this value, the oscillation cannot start properly. This may open a way for using of pure cheaper metal with relatively lower secondary emission coefficient than that of platinum to simplify the magnetron construction and reduce the cost.

3. The mode stability in SHMs.

It is found that the neighbouring modes are the main competitors of the operating mode in SHMs. The oscillation may jump from one mode to the neighbouring ones when the anode voltage is tuned. Though the operation in the $\pi/2$ mode is capable of a higher output power, it is less stable than the $\pi/2 - 1$ mode operation due to a narrower mode separation.

4. Development of a 95GHz SHM for cloud radar application.

The simulated performance on a compact 95 GHz SHM is in a good agreement with the measured one. A number of engineering issues, such as the pulse duration, the anode temperature and vacuum break down have been considered for the SHM to deliver more than 5kW peak power with 200ns pulse in 0.05% duty cycle. The quality of output signal pulses assessed in experiment indicates that this SHM can be effectively used for the development of a low cost W-band cloud radar.

5. The non-periodical space charge distribution in SHMs.

The particle simulations reveal that contrary to a conventional magnetron in which there are periodical and well defined electron spokes, the space charge in the SHM is non-periodical due to the secondary emission cathode and the non-π mode operation. The turbulent space charge results in low output efficiency in SHMs.

6. Investigation of a 209 GHz SHM.

When the SHM operating frequency is further increased to THz band, the RF field is found to be closer to the anode surface. Thus, the electron bunches have to be near the anode surface for the synchronised energy exchange, which further lowers the magnetron efficiency. The measurement on the fabricated anode cavity shows that the fabrication tolerance should be taken into account during the design of the THz-band magnetron.

7. Simulation of a 300 GHz SHM.

The research work on the 35GHz, 95GHz, and 209GHz SHMs has stimulated me to study a magnetron above 300GHz. Based on the analysis on a 44-cavity anode, the $\pi/2$-3 mode is chosen to improve the mode stability. The particle simulation indicates that such magnetrons can deliver at least 0.6 kW peak power at a frequency above 300GHz.

6.2 Future work

Although a number of the millimetre-wave and THz band SHMs have been investigated in this thesis, there are still many issues to be addressed further. The areas deserve further study may include the following.

- As is known, the rate of rise up of anode voltage, which is determined by the modulator, plays an important role in the magnetron performance. Therefore, the influence of the rate of rise up of anode voltage needs to be investigated in the future.

- The amplitude of the backward harmonic is always smaller than the amplitude of the fundamental one, i.e. π mode. This results in a weak interaction of electrons with the RF field, leading to a low efficiency in the SHMs. On the other hand, since there is no mode separation straps on the anode, the THz magnetron with a large number of side resonators has very small mode separation even in the spatial harmonics. Therefore, a rising sun type of the anode with a good separation between the π mode and the neighbouring modes is a promising candidate to be explored for the development of THz magnetrons.

- The current approach to develop a magnetron beyond 300GHz is to increase the side cavity numbers on the azimuthal plane of the anode. We have already seen the limitation of this approach since the mode separation is getting worse with a poor oscillation stability and a low efficiency, apart from the engineering challenges. One possible approach to be explored is to employ a high order harmonic on the axial plane of the anode, i.e. so-called dash modes in the conventional magnetrons. The preliminary study has shown that the anode frequency is beyond 300GHz when operating in the first axial harmonic with the same 209GHz magnetron anode cavity as studied in Chapter 5.

References

[1] W. Willshaw, L. Rushforth, A. Stainsby, R. Latham, A. Balls, and A. King, "The high-power pulsed magnetron: development and design for radar applications," *Electrical Engineers-Part IIIA: Radiolocation, Journal of the Institution of,* vol. 93, p. 985, 1946.

[2] H. A. Boot and J. T. Randall, "Historical notes on the cavity magnetron," *IEEE Transactions on Electron Devices,* vol. 23, pp. 724-729, 1976.

[3] G. R. Kilgore, "Recollections of pre-world war II magnetrons and their applications," *IEEE Transactions on Electron Devices,* vol. 31, pp. 1593-1595, 1984.

[4] R. W. Grow and D. Watkins, "Backward-wave oscillator efficiency," *Proceedings of the IRE,* vol. 43, pp. 848-856, 1955.

[5] C. Paoloni, M. Mineo, M. Henry, and P. G. Huggard, "Double Corrugated Waveguide for Ka-Band Traveling Wave Tube," *Electron Devices, IEEE Transactions on,* vol. 62, pp. 3851-3856, 2015.

[6] J. R. Pierce, "Traveling ‐ wave tubes," *Bell System Technical Journal,* vol. 29, pp. 390-460, 1950.

[7] H. T. Tran, G. Lankford, M. E. Read, R. L. Ives, K. Reppert, K. Cline, and J. Guzman, "Optimization of klystron designs using deterministic sampling methods," *IEEE Transactions on Electron Devices,* vol. 62, pp. 1032-1036, 2015.

[8] A. Staprans, E. McCune, and J. A. Ruetz, "High-power linear-beam tubes," *Proceedings of the IEEE,* vol. 61, pp. 299-330, 1973.

[9] A. Marinelli, D. Ratner, A. Lutman, J. Turner, J. Welch, F.-J. Decker, H. Loos, C. Behrens, S. Gilevich, and A. Miahnahri, "High-intensity double-pulse X-ray free-electron laser," *Nature communications,* vol. 6, 2015.

[10] J. M. Madey and D. A. Deacon, "Free electron lasers," in *Cooperative effects in matter and radiation*, ed: Springer, 1977, pp. 313-334.

[11] V. Flyagin, A. Gaponov, I. Petelin, and V. Yulpatov, "The gyrotron," *IEEE transactions on microwave theory and techniques,* vol. 25, pp. 514-521, 1977.

[12] A. Cross, W. He, A. Phelps, K. Ronald, C. Whyte, A. Young, C. Robertson, E. Rafferty, and J. Thomson, "Helically corrugated waveguide gyrotron traveling wave amplifier using a thermionic cathode electron gun," *Applied physics letters,* vol. 90, p. 253501, 2007.

[13] J. H. Booske, R. J. Dobbs, C. D. Joye, C. L. Kory, G. R. Neil, G.-S. Park, J. Park, and R. J. Temkin, "Vacuum electronic high power terahertz sources," *IEEE Transactions on Terahertz Science and Technology,* vol. 1, pp. 54-75, 2011.

[14] P. H. Siegel, "Terahertz technology," *IEEE transactions on microwave theory and techniques,* vol. 50, pp. 910-928, 2002.

[15] R. K. Parker, R. H. Abrams, B. G. Danly, and B. Levush, "Vacuum electronics," *IEEE transactions on microwave theory and techniques,* vol. 50, pp. 835-845, 2002.

[16] D. M. Pozar, *Microwave engineering*: John Wiley & Sons, 2009.

[17] "Electron tube," *https://www.britannica.com/.*

[18] H. Li, A. J. Illingworth, and J. Eastment, "A simple method of Dopplerizing a pulsed magnetron radar," *Microwave Journal,* vol. 37, pp. 226-232, 1994.

[19] M. Brady and M. Edwards, "Developments in marine radar magnetrons," in *Origins and Evolution of the Cavity Magnetron (CAVMAG), 2010 International Conference on the*, 2010, pp. 58-63.

[20] D. I. Thwaites and J. B. Tuohy, "Back to the future: the history and development of the clinical linear accelerator," *Physics in medicine and biology*, vol. 51, p. R343, 2006.

[21] J. E. Gerling, "Microwave oven power: a technical review," *Journal of Microwave Power and Electromagnetic Energy*, vol. 22, pp. 199-207, 1987.

[22] J. O. McSpadden and J. C. Mankins, "Space solar power programs and microwave wireless power transmission technology," *IEEE microwave magazine*, vol. 3, pp. 46-57, 2002.

[23] R. T. Austin, A. J. Heymsfield, and G. L. Stephens, "Retrieval of ice cloud microphysical parameters using the CloudSat millimeter‐wave radar and temperature," *Journal of Geophysical Research: Atmospheres (1984–2012)*, vol. 114, 2009.

[24] K. P. Moran, B. E. Martner, M. Post, and R. A. Kropfli, "An unattended cloud-profiling radar for use in climate research," *Bulletin of the American Meteorological Society*, vol. 79, p. 443, 1998.

[25] "Radar Basics," *www.radartutorial.eu*.

[26] L. Liao and K. Sassen, "Investigation of relationships between Ka-band radar reflectivity and ice and liquid water contents," *Atmospheric research*, vol. 34, pp. 231-248, 1994.

[27] K. Sassen and L. Liao, "Estimation of cloud content by W-band radar," *Journal of Applied Meteorology*, vol. 35, pp. 932-938, 1996.

[28] J. Richards, "Microwave Radar and Radiometric Remote Sensing [Book Reviews]," *IEEE Geoscience and Remote Sensing Magazine,* vol. 3, pp. 51-52, 2015.

[29] E. Im, C. Wu, and S. L. Durden, "Cloud profiling radar for the CloudSat mission," in *IEEE International Radar Conference, 2005.*, 2005, pp. 483-486.

[30] A. Roitman, D. Berry, and B. Steer, "State-of-the-art W-band extended interaction klystron for the CloudSat program," *IEEE Transactions on Electron Devices,* vol. 52, pp. 895-898, 2005.

[31] U. Görsdorf, V. Lehmann, M. Bauer-Pfundstein, G. Peters, D. Vavriv, V. Vinogradov, and V. Volkov, "A 35-GHz polarimetric Doppler radar for long-term observations of cloud parameters—Description of system and data processing," *Journal of Atmospheric and Oceanic Technology,* vol. 32, pp. 675-690, 2015.

[32] G. P. Williams, "Filling the THz gap—high power sources and applications," *Reports on Progress in Physics,* vol. 69, p. 301, 2005.

[33] S. Koenig, D. Lopez-Diaz, J. Antes, F. Boes, R. Henneberger, A. Leuther, A. Tessmann, R. Schmogrow, D. Hillerkuss, and R. Palmer, "Wireless sub-THz communication system with high data rate," *Nature Photonics,* vol. 7, pp. 977-981, 2013.

[34] J. F. Federici, B. Schulkin, F. Huang, D. Gary, R. Barat, F. Oliveira, and D. Zimdars, "THz imaging and sensing for security applications—explosives, weapons and drugs," *Semiconductor Science and Technology,* vol. 20, p. S266, 2005.

[35] R. Appleby and H. B. Wallace, "Standoff detection of weapons and contraband in the 100 GHz to 1 THz region," *IEEE transactions on antennas and propagation,* vol. 55, pp. 2944-2956, 2007.

[36] A. Kellarev and D. Sheffer, "Terahertz remote sensing," in *SPIE Defense, Security, and Sensing*, 2011, pp. 80230N-80230N-9.

[37] M. Tonouchi, "Cutting-edge terahertz technology," *Nature Photonics,* vol. 1, pp. 97-105, 2007.

[38] T. G. Phillips and J. Keene, "Submillimeter astronomy [heterodyne spectroscopy]," *Proceedings of the IEEE,* vol. 80, pp. 1662-1678, 1992.

[39] B. Deng, C. Domier, A. Donné, K. Lee, N. Luhmann, E. Mazzucato, T. Munsat, H. Park, and M. Van De Pol, "THz techniques in plasma diagnostics," in *Microwave Symposium Digest, 2002 IEEE MTT-S International*, 2002, pp. 1587-1590.

[40] P. H. Siegel, "Terahertz technology in biology and medicine," in *Microwave Symposium Digest, 2004 IEEE MTT-S International*, 2004, pp. 1575-1578.

[41] R. Robertshaw and W. Willshaw, "Some properties of magnetrons using spatial-harmonic operation," *Proceedings of the IEE-Part C: Monographs,* vol. 103, pp. 297-306, 1956.

[42] L. Ma, "3D computer modeling of magnetrons," *Phd thesis, Queen Mary University of London.,* 2004.

[43] M. I. Avtomonov, S. V. Sosnytskiy, and D. M. Vavriv, "Investigation and Optimization of Auxiliary Cathode for the Secondary-Emission Cold-Cathode Magnetrons," in *Microwave Conference (GeMIC), 2008 German*, 2008, pp. 1-4.

[44] I. Krupatkin, O. Baranov, N. Galushko, and V. Y. Ignatov, "Pulsed magnetrons of millimeter wave range in the spatial harmonics mode," *Ukr. J. Phys,* vol. 20, pp. 1170-1176, 1975.

[45] A. W. Hull, "The Effect of A Uniform Magnetic Field on the Motion of Electrons Between Coaxial Cylinders," *Physical Review,* vol. 18, p. 31, 1921.

[46] K. Posthumus, "Oscillations in a split anode magnetron," *Wireless Engineer,* vol. 12, p. 126, 1935.

[47] A. Gilmour Jr, "Microwave tubes," *Dedham, MA, Artech House, 1986, 502 p.,* vol. 1, 1986.

[48] E. C. Megaw, "The high-power pulsed magnetron: a review of early developments," *Electrical Engineers-Part IIIA: Radiolocation, Journal of the Institution of,* vol. 93, pp. 977-984, 1946.

[49] H. Boot and J. Randall, "The cavity magnetron," *Electrical Engineers-Part IIIA: Radiolocation, Journal of the Institution of,* vol. 93, pp. 928-938, 1946.

[50] G. B. Collins, *Microwave magnetrons* vol. 6: McGraw-Hill Book Company, 1948.

[51] J. Benford, J. A. Swegle, and E. Schamiloglu, *High power microwaves*: CRC Press, 2015.

[52] K. Schuenemann, A. Serebryannikov, S. Sosnytskiy, and D. Vavriv, "Optimizing the spatial-harmonic millimeter-wave magnetron," *Physics of Plasmas (1994-present),* vol. 10, pp. 2559-2565, 2003.

[53] W. Kleen, *Electronics of microwave tubes*: Elsevier, 2012.

[54] I. Bronshtein and B. Fraiman, "Secondary electron emission," ed: Nauka, Moscow, 1969.

[55] K. Schunemann, S. V. Sosnytskiy, and D. M. Vavriv, "Self-consistent simulation of the spatial-harmonic magnetron with cold secondary-emission cathode," *IEEE Transactions on Electron Devices*, vol. 48, pp. 993-998, 2001.

[56] J. R. M. Vaughan, "A new formula for secondary emission yield," *IEEE Transactions on Electron Devices*, vol. 36, pp. 1963-1967, 1989.

[57] S. S. Viktorovich, "Magnetron theory on the spatial harmonic with cold secondary-emission cathode," *Phd thesis, Institute of Radio Astronomy of National Academic Science of Ukraine.*, 2004.

[58] A. D. Andreev and K. J. Hendricks, "Particle-in-cell (PIC) simulation of CW industrial heating magnetron," *Journal of Microwave Power and Electromagnetic Energy,* vol. 44, pp. 114-124, 2010.

[59] H. Kim and J. Choi, "Characterization of a 16-vane strapped magnetron oscillator by three-dimensional particle-in-cell code simulations," *Current Applied Physics,* vol. 6, pp. 66-70, 2006.

[60] V. B. Neculaes, M. C. Jones, R. M. Gilgenbach, Y. Lau, J. W. Luginsland, B. W. Hoff, W. M. White, N. Jordan, P. Pengvanich, and Y. Hidaka, "Magnetic priming effects on noise, startup, and mode competition in magnetrons," *IEEE transactions on plasma science,* vol. 33, pp. 94-102, 2005.

[61] H. L. McDowell, "Magnetron simulations using a moving wavelength computer code," *IEEE transactions on plasma science,* vol. 26, pp. 733-754, 1998.

[62] S. V. Sosnytskiy and D. M. Vavriv, "Theory of the spatial-harmonic magnetron: an equivalent network approach," *IEEE transactions on plasma science,* vol. 30, pp. 984-991, 2002.

[63] J.-I. Kim, S.-G. Jeon, G.-J. Kim, J. Kim, V. Yeryomka, A. Tishchenko, and V. Naumenko, "Numerical and experimental investigation of a 35 GHz 20-vane spatial-harmonic magnetron," in *35th International Conference on Infrared, Millimeter, and Terahertz Waves*, 2010.

[64] M. C. Balk, "3D Magnetron simulation with CST STUDIO SUITE™," in *Vacuum Electronics Conference (IVEC), 2011 IEEE International*, 2011, pp. 443-444.

[65] "CST user manual," 2016.

[66] A. Shih, J. Yater, C. Hor, and R. Abrams, "Secondary electron emission studies," *Applied surface science,* vol. 111, pp. 251-258, 1997.

[67] N. N. Esfahani, M. Tayarani, and K. Schünemann, "Design and simulation of a π/2-mode spatial-harmonic magnetron," *AEU-International Journal of Electronics and Communications,* vol. 67, pp. 426-432, 2013.

[68] V. Kovalenko, "Physics of Heat Transfer and Electrovacuum Devices," *Sovetskoe Radio, Moscow,* 1975.

[69] R. V. Latham, *High voltage vacuum insulation: Basic concepts and technological practice*: Elsevier, 1995.

[70] V. Volkov, *Magnetron based radar Systems for millimeter wavelength band-modern approaches and prospects*: INTECH Open Access Publisher, 2010.

[71] N. Maiti, K. Thakur, D. Patil, and A. Das, "High voltage breakdown studies in electron gun and its damage control," in *2014 International Symposium on Discharges and Electrical Insulation in Vacuum (ISDEIV)*, 2014, pp. 37-39.

[72] N. Maiti, U. Barve, S. K. Mishra, M. Bhatia, and A. Das, "Attenuation of electron gun generated surges in an electron beam evaporation system using ferrite beads," *Vacuum,* vol. 86, pp. 1810-1814, 2012.

[73] H. L. McDowell, "Magnetron simulations using a multiple wavelength computer code," *IEEE transactions on plasma science,* vol. 32, pp. 1160-1170, 2004.

[74] J. Fisk, H. Hagstrum, and P. Hartman, "The magnetron as a generator of centimeter waves," *The Bell System Technical Journal,* vol. 25, pp. 167-348, 1946.

[75] N. Avtomonov, V. Naumenko, D. M. Vavriv, K. Schünemann, A. Suvorov, and V. Markov, "Toward Terahertz Magnetrons: 210-GHz Spatial-Harmonic Magnetron With Cold Cathode," *IEEE Transactions on Electron Devices,* vol. 59, pp. 3608-3611, 2012.

[76] N. Avtomonov, V. Naumenko, and D. Vavriv, "Development of terahertz spatial-harmonic magnetrons," in *Microwave Conference (EuMC), 2013 European*, 2013, pp. 187-190.

[77] N. N. E. a. K. Schünemann, "Towards the application of MNG-loaded slow wave structures in spatial harmonic magnetrons," *6th International Congress on Advanced Electromagnetic Materials in Microwaves and Optics* pp. 487-489, 2012.

[78] O. P. Kulagin and V. D. Yeryomka, "Optimal conditions for drift-orbital resonance in M-type devices," *IEEE transactions on plasma science,* vol. 32, pp. 1181-1186, 2004.